2011

Development of the spectral difference method and application in the numerical investigation of the separated and transitional flows over a low-Reynolds number airfoil

Ying Zhou
Iowa State University

Development of the spectral difference method and application in the numerical investigation of the separated and transitional flows over a low-Reynolds number airfoil

by

Ying Zhou

A dissertation submitted to the graduate faculty
In partial fulfillment of the requirements for the degree of
DOCTOR OF PHILOSOPHY

Major: Aerospace Engineering

Program of Study Committee:
Z.J. Wang, Major Professor
Paul Durbin
Hui Hu
Alric Rothmayer
Jue Yan

Iowa State University
Ames, Iowa

2011

TABLE OF CONTENTS

LIST OF FIGURES

LIST OF TABLES

ABSTRACT

The development of the high-order accuracy spectral difference (SD) method on hexahedral mesh and its applications in aeroacoustic and aerodynamic problems are carried out in this work. Two absorbing boundary conditions, the absorbing sponge zone and the perfectly matched layer, are developed and implemented for the SD method discretizing the Euler and Navier-Stokes equations on unstructured grids. The performance of both boundary conditions is evaluated and compared with the characteristic boundary condition for a variety of benchmark problems including vortex and acoustic wave propagations. The applications of the perfectly matched layer technique in the numerical simulations of unsteady problems with complex geometries are also presented to demonstrate its capability.

Numerical simulations of the low-Reynolds number ($\mathrm{Re} = 10^4 \sim 10^5$) flows over a SD7003 airfoil at moderate incidences ($< 10°$) are performed. A low-frequency convective instability is observed to dominate the spectrum near the leading edge and be responsible for the growth of the disturbance in the attached boundary layer. The characteristic frequency, the growth rate and the wave shape are investigated based on the numerical results. The growth of the low-frequency instability is not in agreement with parallel flow stability theory, nor with leading edge receptivity theory. And it has a higher growth rate than the Tollmien-Schlichting (T-S) wave. The effects of the angle-of-attack (AoA), the Reynolds number and the airfoil geometry on the low-frequency instability are investigated and discussed.

The mechanisms in the breakdown process are investigated and discussed. it is observed that the breakdown of the shedding vortices starts at approximately the location with the maximum negative streamwise flow velocity. And the reverse flow in the separation region directly triggers the generation of three dimensional disturbances and the streamwise vorticities. In addition, the secondary instability which initiates the breakdown process differs in cases at different AOAs. The elliptic and hyperbolic instabilities observed in bluff-body wakes are found to occur in the breakdown process of current cases. Furthermore, the sequence of breakdown states at various incidences is found to be similar to that of the bluff-body wakes at various Reynolds numbers.

A numerical investigation of passive LSB control techniques using roughness bumps on a low-Reynolds number wing is conducted as a further study. The previous case at $Re = 6 \times 10^4$ and $AoA = 4°$ is used as the baseline (uncontrolled) case. In the controlled cases, roughness bumps are strategically placed near the leading edge of the wing for the purpose of improving aerodynamic performance in terms of the lift to drag ratio. The location, bump size, the number of bumps and the AoA are varied to study the effects. The pressure drag forces in the controlled cases are found to be reduced significantly when the LSB are reduced or avoided, resulting in much improved lift over drag ratio.

CHAPTER 1. General Introduction

Introduction

In the last two decades, there have been intensive research efforts on high-order methods for unstructured grids. Such methods provide unprecedented geometric flexibility and accuracy for real world applications. An incomplete list of notable examples includes the spectral element method [1], multi-domain spectral method [2,3], k-exact finite volume method [4], WENO methods [5], discontinuous Galerkin (DG) method [6,7,8], high-order residual distribution methods [9], spectral volume (SV) [10-14] and spectral difference (SD) methods [15-21]. Spectral difference method originated in the staggered grid multi-domain spectral method [2,3]. Thereafter it was generalized to simplex elements by Liu et al [16,22]. More recently, a weak instability was discovered by van Den Abeele et al. [23] and Huynh [24]. The use of Gauss quadrature points and the two ending points as the flux points fixes the problem, and it was proved to be stable by Jameson [25]. A high-order SD method for three dimensional Navier-Stokes equations on unstructured hexahedral grids developed by Sun et al. [18,19] is used in this paper.

For the numerical simulations of fluid dynamic and aeroacoustic problems, a proper artificial computational boundary condition is needed to minimize the reflection of out-going waves, which can contaminate the physical flow field. This boundary condition is usually called the non-reflecting boundary condition or absorbing boundary condition. It remains a critical component and a difficult challenge in the development of computational fluid dynamics (CFD) and computational aeroacoustics (CAA) algorithms. Significant progresses have been made in this research as reviewed extensively by Colonius et al. [26] and Hu [27].

The non-reflecting boundary condition based on the characteristics of the Euler equations was developed as one of the first attempts to minimize the reflection of out-going waves, e.g., in [28-30]. The absorbing boundary condition (ABC) also receives much attention from the electromagnetic and acoustic communities. An innovative class of approaches of non-reflecting/absorbing boundary conditions uses extra artificial zones to reduce wave reflections. They are the loosely termed “zonal techniques” [27]. In this type of technique, additional zones surrounding the physical domain are introduced so that in the added zones either the outgoing disturbances/waves are attenuated and thus the reflections are minimized, or the mean flow is altered gradually to be supersonic and thus all disturbances/waves are out-going. Two popular zonal techniques are the absorbing sponge zone (ASZ) technique [31] and perfectly matched layer (PML) technique [32]. In this work, both the ASZ and the PML techniques are extended and implemented for the SD method on hexahedral meshes. The performance and effectiveness are compared with the CBC based on one-dimensional Euler equations. Then a two cylinder case is employed to test the performance of three boundary conditions with complex geometries and vortex dominant flow.

In the past decade, low-Reynolds-number flows and the associated laminar separation bubbles (LSBs) have been of great interest in the development of micro air vehicles (MAV), small scale wind turbines and low-pressure turbine/cascade. Since laminar boundary layers are less resistible to the significant adverse pressure gradient, LSBs are widely found over the suction side of low-Reynolds number airfoils/turbines at incidences. LSBs on an airfoil are classified into two types: a short bubble and a long bubble [33]. A short bubble is formed when the airfoil AoA is relatively small. The flow quickly transitions into a turbulent one and reattaches downstream after the breakdown of LSBs. A long bubble is formed at higher AoAs near the stall condition. For airfoils, the behavior of the LSB affects the aerodynamic performance and typically causes the increase of the pressure drag. Meanwhile, the existence of a turbulent boundary layer induces higher friction force on the airfoil than a laminar flow, and therefore can cause the degradation of the lift-to-drag ratio. Early works on LSB and associated hydrodynamic instability mechanisms can be traced back to the 1950s [33] and 1960s [34-37]. With the rapid development of numerical methods, numerical simulations of laminar-separated flows have been used to investigate the LSB and the associated turbulent transition. The two-dimensional simulations of separation bubbles were first carried out and investigated by Pauley et al [38]. Pauley [39] and Rist [40] carried out three-dimensional studies of the primary instability later, but the transition was still not resolved due to the limitation of the computational resource and computer technology. More recently, direct numerical simulations (DNS) to fully resolve the transition of LSBs to turbulence were conducted by Alam & Sandham [41] and also

Spalart & Strelets [42]. With the development of experimental techniques, Laser-Doppler-Anemometry (LDA) and Particle-Image-Velocity (PIV) technologies can provide the flow field measurements to quantify the evolution of the unsteady flow structure and investigate the dynamics of LSBs (see Marxen et al. [43]; Lang et al. [44]; Hu & Yang [45]; Yarusevych et al. [46]; Hain et al.[47]). In spite of considerable progresses in recent years, both the LSB and the transition mechanism still need further investigation. Distinct from the convective types of transition, the simultaneous presence of and the interaction between separation and transition make the problem highly complicated.

In the present study, the numerical simulations of the low-Reynolds number flows over a SD7003 airfoil at incidences are carried out by using the high-order SD method for the three-dimensional Navier-Stokes equations on hexahedral grids. The simulations started with a uniform freestream initial condition and no incoming disturbances are added explicitly. The 'short' bubbles and transitional flows are observed on the suctions side of the airfoil under the present conditions. We study the primary growth of disturbances on a low-Reynolds number airfoil at moderate incidences when 'short' bubbles occur, and a low-frequency instability is found to be dominant near the leading edge and responsible for the growth of disturbances. The growth of the low-frequency instability is not in agreement with the parallel flow stability theory, nor with the leading edge receptivity theory. The AoA, Reynolds number and the geometry of the airfoil are varied to investigate their effects on the frequency and the growth rate of the low-frequency instability.

The breakdown processes of the current 'short' LSBs at different incidences are investigated and discussed in this work. The breakdown to turbulent flow occurs more abruptly than the receptivity and disturbance-growth stages. In different flows, there are different possible scenarios for the breakdown process but it is generally accepted the breakdown is caused by the uncontrolled growth of unstable three dimensional waves. The so-called secondary instability in compare with the primary instability is responsible for the growth of the three dimensional disturbances. In the present cases, the secondary instability which initiates the breakdown process differs in cases at different AOAs. The elliptic and hyperbolic instabilities observed in bluff-body wakes are found to occur in the breakdown process of current cases. Furthermore, the sequence of breakdown states at various incidences is found to be similar to that of the bluff-body wakes at various Reynolds numbers.

Flow control, the technique to manipulate a flow field to achieve a desired change, is of immense technological importance, and thus is pursued by many scientists and engineers in various areas of fluid mechanics field for many years. The configuration lift, drag and $\mathrm{L/D}$ ratio are the principal considerations in the design and construction of air vehicles. The decrease in drag and increase in $\mathrm{L/D}$ ratio can increase the range and reduce the required thrust, which result in improved fuel economy. Low-Reynolds number ($\mathrm{Re_c} = 10^4 \sim 10^5$) flow has been of interest for many decades with the development of Micro Air Vehicles (MAV). In the low-Reynolds number flows over airfoils, the formation of a LSB has a dominant effect on the flow field and usually causes high pressure drag force on the airfoil. Reducing or avoiding the LSB on the surfaces of the airfoils is one way of achieving reduced drag. Because of this, aerodynamicists and aircraft designers have pursued the objective of separation control for many decades.

A passive flow control technique using surface roughness (bumps) near the leading-edge of the wing is numerically studied as a further study. High-order methods on unstructured grids are known for their advantages of accuracy and flexibility in the numerical simulation of multi-scale flow with complex geometries. The approach of SD method is capable of capturing the laminar separation and the vortex breakdown, and has been previously shown in the numerical simulation of the attached/detached laminar flow and the reattached turbulent flow. The roughness bumps can affect the formation of the LSBs and be used for the purpose of aerodynamic performance improvement. The flow over a SD7003 wing at $\mathrm{AoA} = 4$ deg, $\mathrm{Re_c} = 6 \times 10^4$ and $\mathrm{M} = 0.2$ is used as the baseline model and the starting point for the controlled models. In the controlled cases, roughness bumps are strategically placed near the leading edge of the wing for the purpose of improving aerodynamic performance in terms of the lift to drag ratio. The location, bump size, the number of bumps and the angle-of-attack are varied to study the effects. The pressure drag forces in the controlled cases are found to be reduced significantly when the LSB are reduced or avoided, resulting in much improved lift over drag ratio.

Dissertation Organization

The rest of this dissertation is organized as follows.

Chapter 2, “Absorbing Boundary Conditions for the Euler and Navier-Stokes Equations with the Spectral Difference Method” is a paper published in Journal of Computational Physics. I am the primary author of the paper, responsible for most of the work and writing.

Chapter 3, “A Low-Frequency Instability/Oscillation near the Airfoil Leading-Edge at Low Reynolds Numbers and Moderate Incidences” is a paper planned to submit to AIAA Journal. I am the primary author of the paper, responsible for most of the work and writing.

Chapter 4, “The breakdown of laminar separation bubbles on a low-Reynolds number airfoil at incidences” is a paper planned to submit to AIAA Journal. I am the primary author of the paper, responsible for most of the work and writing.

Chapter 5, “Effects of Surface Roughness on Laminar Separation Bubble over a Wing at a Low-Reynolds Number” is a paper submitted to AIAA Journal and in revision process. I am the primary author of the paper, responsible for most of the work and writing.

Chapter 6 is devoted to general conclusions.

References

[1] T. Poinsot, and S.K. Lele, Boundary conditions for direct simulation of compressible viscous flows, J. Comput. Phys., 101, 104-129(1992)

[2] Y. Liu, M. Vinokur and Z.J. Wang, discontinuous spectral difference method for conservation laws on unstructured grids, in: C. Groth, D.W. Zingg (Eds.), Proceeding of the 3rd international Conference in CFD, Toronto, Springer, 2004, pp. 449-454.

[3] Y. Liu, M. Vinokur and Z.J. Wang, Spectral (finite) difference method for conservation laws on unstructured grids I: Basic formulation, J. Compute. Phys.. 216 (2006), 780-801.

[4] T.J. Barth and P.O. Fredericks o, High-order solution of the Euler equations on unstructured grids using quadratic reconstruction, AIAA Paper 96-0027, 1996.

[5] C. Hu and C.W. Shu, Weighted essentially non-oscillatory schemes on triangular meshes, J. Comput. Phys., 150 (1999), 97-127.

[6] F. Bassi and S. Rebay, High-order accurate discontinuous finite element solution of the 2D euler equations, J. Comput. Phys., 138 (1997), 251-285.

[7] Cockburn and C.W. Shu, TVB Runge-Kutta local projection discontinuous Galerkin finite element method for conservation laws II: General framework, Math. Comput., 52 (1989), 411-435.

[8] Cockburn and C.W. Shu, The Runge-Kutta discontinuous Galerkin method for conservation laws V: multidimentional systems, J. Comput. Phys., 141 (1998), 199-224.

[9] R. Abgrall and P.L. Roe, High order fluctuation schemes on triangular meshes, J. Sci. Compute., 19 (2003), 3-36.

[10] Y, Liu, M. Vinokur and Z.J. Wang, Spectral (finite) volume method for conservation laws on unstructured grids V: Extension to three-dimensional systems, J. Comput. Phys., 212 (2006), 454-472.

[11] Y. Sun, Z.J. Wang and Y. Liu, Spectral (finite) volume method for conservation laws on unstructured grids VI: Extension to viscous flow, J. Comput. Phys., 215 (2006), 41-58.

[12] Z.J. Wang, Spectral (finite) volume method for conservation laws on unstructured grids: Basic formulation, J. Comput. Phys., 178 (2002), 210-251.

[13] Z.J. Wang and Y. Liu, Spectral (finite) volume method for conservation laws on unstructured grids III: Extension to one-dimentional systems, J. Sci. Comput. 20 (2004), 137-157.

[14] Z.J. Wang, L. Zhang and Y. Liu, Spectral (finite) volume method for conservation laws on unstructured grids III: Extension to two-dimentional systems, J. Sci. Comput. 194 (2004), 716-741.

[15] P.G. Huang, Z.J. Wang and Y. Liu, An implicit space-time spectral difference method for discontinuity capturing using adaptive polynomials, AIAA Paper 2005-5255, 2005.

[16] Y. Liu, M. Vinokur and Z.J. Wang, discontinuous spectral difference method for conservation laws on unstructured grids, in: C. Groth, D.W. Zingg (Eds.), Proceeding of the 3rd international Conference in CFD, Toronto, Springer, 2004, pp. 449-454.

[17] G. May and A. Jameson, A spectral difference method for the Euler and Navier-Stokes equations on unstructured grids, AIAA Paper 2006-304, 2006.

[18] Y. Sun, Z.J. Wang, Y. Liu, High-Order Multidomain Spectral Difference Method for the Navier-Stokes Equations on Unstructured Hexahedral Grids, Communications in Computational Physics, Vol. 2, No. 2(2007) 310-333.

[19] Y. Sun, Z.J. Wang, Y. Liu and C.L. Chen, Efficient implicit LU-SGS algorithm for high-order spectral difference method on unstructured hexahedral grids, AIAA paper, (2007), 2007-0313

[20] Z.J. Wang and Y. Liu, The spectral difference method for the 2D Euler equations on unstructured grids, AIAA Paper 2005-5112, 2005.

[21] Z.J. Wang, Y. Liu, G. May and A. Jameson, Spectral difference method for unstructured grids II: Extension to the Euler equations, J. Sci. Comput., 32(1) (2007), 45-71.

[22] Y. Liu, M. Vinokur and Z.J. Wang, Spectral (finite) difference method for conservation laws on unstructured grids I: Basic formulation, J. Compute. Phys.. 216 (2006), 780-801.

[23] K. Van den Abeele, C. Lacor and Z.J. Wang, "On the stability and accuracy of the spectral difference method," Journal of Scientific Computing, Journal of Scientific Computing 37, (2008) 162–188.

[24] H.T. Huynh, A flux reconstruction approach to high-order schemes including discontinuous Galerkin methods, AIAA Paper 2007-4079.

[25] Jameson, A Proof of the stability of the spectral difference method for all orders of accuracy, ACL Report no. 2009-1, Stanford University, March, 2009.

[26] T. Colonius, Modelling Artificial Boundary Conditions for Compressible Flow, Annual Review of Fluid Mechanics, Vol. 36, 2004,pp. 315-345.

[27] F.Q. Hu, Absorbing boundary conditions (a review), International Journal of Computational Fluid Dynamics, Vol. 18, No. 6, 513-522, 2004

[28] M. B. Giles, Non-reflecting boundary conditions for Euler equation calculations, AIAA J., 28, 2050-2058(1990).

[29] T. Poinsot, and S.K. Lele, Boundary conditions for direct simulation of compressible viscous flows, J. Comput. Phys., 101, 104-129(1992)

[30] K.W. Thompson, Time-dependent boundary conditions for hyperbolic systems, J. Comput. Phys., 68, 1-24(1987).

[31] J. B. Freund, Proposed inflow/outflow boundary condition for direct computation of aerodynamic sound, AIAA J., 35(4), 740-742(1997).

[32] F.Q. Hu, X.D. Li and D.K. Lin, Absorbing boundary conditions for nonlinear Euler and Navier-Stokes equations based on the Perfectly Matched Layer technique, Journal of Computational Physics,227-9(2008), 4398-4424.

[33] Owen, P. R. and Klanfer, L. On the laminar boundary layer separation from the leading edge of a thin aerofoil. 1953 ARC Conf. Proc. 220.

[34] Gaster, M. 1963 On stability of parallel flows and the behaviour of separation bubbles. PhD Dissertation, University of London.

[35] GASTER, M. 1967 The structure and behaviour of separation bubbles. Aero. Res. Counc. R&M 3595. Aerodynamics Division NPL.

[36] HORTON, H. P. 1967 A semi-empirical theory for the growth and bursting of laminar separation bubbles. Aero. Res. Counc. Current Paper 1073.

[37] HORTON, H. P. 1968 Laminar separation in two and three-dimensional incompressible flow. PhD Dissertation, University of London.

[38] PAULEY, L. L., MOIN, P. & REYNOLDS, W. C. 1990 The structure of two-dimensional separation. J. Fluid Mech. 220, 397-411.

[39] PAULEY, L. L. 1994 Response of two-dimensional separation to three-dimensional disturbances. Trans. ASME: J. Fluids Engng 116, 433–438.

[40] RIST, U. 1994 Nonlinear effects of 2D and 3D disturbances on laminar separation bubbles. Proc. IUTAM Symp. on Nonlinear Instability of Nonparallel Flows, pp. 324–333. Springer.

[41] ALAM, M. & SANDHAM, N. D. 2000 Direct numerical simulation of ‘short’ laminar separation bubbles with turbulent reattachment. J. Fluid Mech. 410, 1–28.

[42] SPALART, P. R. & STRELETS, M. K. H. 2000 Mechanisms of transition and heat transfer in a separation bubble. J. Fluid Mech. 403, 329–349.

[43] MARXEN, O., LANG, M., RIST, U. & WAGNER, S. 2003 A combined experimental/numerical study of unsteady phenomena in a laminar separation bubble. Flow, Turbulence Combust. 71, 133–146.

[44] LANG, M., RIST, U. & WAGNER, S. 2004 Investigations on controlled transition development in a laminar separation bubble by means of LDA and PIV. Exp. Fluids 36, 43–52.

[45] H. HU AND Z. YANG, "An Experimental Study of the Laminar Flow Separation on a Low Reynolds Number Airfoil", ASME Journal of Fluid Engineering, Vol.130, No.5, 051101, 2008.

[46] YARUSEVYCH, S., SULLIVAN, P.E. & KAWALL, J.G. 2009 On vortex shedding from an airfoil in low-Reynolds-number flows. J. Fluid. Mech. 632, 245-271

[47] HAIN, R., KAHLER, C. J. & RADESPIEL, R. 2009 Dynamics of laminar separation bubbles at low-Reynolds-number aerofoils. J. Fluid Mech. 630, 129–153.

CHAPTER 2. Absorbing Boundary Conditions for the Euler and Navier-Stokes Equations with the Spectral Difference Method

A paper published in Journal of Computational Physics

Ying Zhou and Z.J. Wang

Abstract

Two absorbing boundary conditions, the absorbing sponge zone and the perfectly matched layer, are developed and implemented for the spectral difference method discretizing the Euler and Navier-Stokes equations on unstructured grids. The performance of both boundary conditions is evaluated and compared with the characteristic boundary condition for a variety of benchmark problems including vortex and acoustic wave propagations. The applications of the perfectly matched layer technique in the numerical simulations of unsteady problems with complex geometries are also presented to demonstrate its capability.

1. Introduction

In the last two decades, there have been intensive research efforts on high-order methods for unstructured grids. Such methods provide unprecedented geometric flexibility and accuracy for real world applications. An incomplete list of notable examples includes the spectral element method [51], multi-domain spectral method [44,45], k-exact finite volume method [6], WENO methods [27], discontinuous Galerkin (DG) method [7,12,13], high-order residual distribution methods [1], spectral volume (SV) [49,56,64,65,66] and spectral difference (SD) methods [40,47,50,57,58,67,68]. Spectral difference method originated in the staggered grid multi-domain spectral method [43,44]. Thereafter it was generalized to simplex elements by Liu et al [47,48]. More recently, a weak instability was discovered by van Den Abeele et al. [63] and Huynh [41]. The use of Gauss quadrature points and the two ending points as the flux points fixes the problem, and it was proved to be stable by Jameson [42]. A high-order SD method for three dimensional Navier-Stokes equations on unstructured hexahedral grids developed by Sun et al. [57,58] is used in this paper.

For the numerical simulations of fluid dynamic and aeroacoustic problems, a proper artificial computational boundary condition is needed to minimize the reflection of out-going waves, which can contaminate the physical flow field. This boundary condition is usually called the non-reflecting boundary condition or absorbing boundary condition. It remains a critical component and a difficult challenge in the development of computational fluid dynamics (CFD) and computational aeroacoustics (CAA) algorithms. Significant progresses have been made in this research as reviewed extensively by Colonius et al. [16] and Hu [34].

The non-reflecting boundary condition based on the characteristics of the Euler equations was developed as one of the first attempts to minimize the reflection of out-going waves, e.g., in [21,54,61]. In the Godunov-type finite volume methods, the characteristic boundary condition (CBC) based on the linearized one-dimensional Euler equations [45,69,26] is widespread and works well in the numerical simulations of steady problems. For multi-dimensional problems, the performance of the CBC degrades if the wave propagation direction is not aligned with the boundary face normal direction. More efficient and accurate non-reflecting boundary conditions are needed to handle problems like vortex dominated flows and wave propagation problems.

The absorbing boundary condition (ABC) also receives much attention from the electromagnetic and acoustic communities. Engquist and Majda [18] made a pioneering contribution to in this area. Their boundary conditions were constructed to minimize reflections of waves traveling in directions close to perpendicular to the boundary. Higdon [25] further developed the boundary conditions in a simpler and more general form. Another well-known ABC firstly proposed by Bayliss and Turkel [8,9] was developed in an asymptotic expansion of the solution in the far field and annihilate of the leading terms. This type of ABC is widely used in scattering problems to absorb the outgoing disturbances. In the present study, we consider flow problems with strong nonlinear viscous wakes. As a result, we did not pursue the above boundary conditions.

An innovative class of approaches of non-reflecting/absorbing boundary conditions uses extra artificial zones to reduce wave reflections. They are the loosely termed “zonal techniques” [34]. In this type of technique, additional zones surrounding the physical domain are introduced so that in the added zones either the outgoing disturbances/waves are attenuated and thus the reflections are minimized, or the mean flow is altered gradually to be supersonic and thus all disturbances/waves are out-going. Two popular zonal techniques are the absorbing sponge zone (ASZ) technique [19] and perfectly matched layer (PML) technique [39].

The ASZ technique used in this paper was first proposed for the direct acoustic simulation by Colonius et al. [15]. It was further developed and theoretically analyzed by Freund [19] and Bodony [11]. Inside the ASZ domain, one source term $-\sigma(\mathrm{Q}-\overline{\mathrm{Q}})$ is added to the right-hand-side of the governing equations such that the solution Q is gradually tuned to the proposed solution $\overline{\mathrm{Q}}$. In order to diminish the reflected error generated at the physical/ASZ interface, the absorbing coefficient σ increases smoothly from zero at the interface to a positive value at the end of the ASZ domain. This technique is widely used in the CAA community for its simplicity and effective performance.

The PML technique was originally developed as an absorbing boundary condition for computational electromagnetic [10] in which the Maxwell equations are numerically solved, and quickly became the method of choice in the computational electromagnetic community [20,53]. The PML equations are formulated such that the amplitude of the out-going waves entering the PML domain can be exponentially reduced while causing as little numerical reflection as possible. It was also found to be a good choice for computational aeroacoustics and computational fluid dynamics [14,22,23,24,62]. The PML technique was firstly extended to the linearized Euler equations in [28]. However the direct adaption of the split formulation to the Euler equations was found to be unstable in the PML domain [28,29,2,3,4,5,60,70]. Hu [30,31,33,35,52] found that for the PML technique to yield stable absorbing boundary condition, the phase and group velocities of the physical wave supported by the governing equations must be consistent and in the same direction, and a stable formulation of a PML for the linearized Euler equations was proposed. It was proved in [36] that theoretically no reflection will be generated in the PML domain for linearized Euler equations. Further extension of the PML technique to nonlinear Euler and Navier-Stokes equations was given in [37,39]. For nonlinear equations, though the conversion of the equations is not perfectly matched to the original equations due to the nonlinearity of flux vectors, the results of the numerical examples show that the proposed absorbing equations are still effective [37,38,39].

In this paper, both the ASZ and the PML techniques are extended and implemented for the SD method on hexahedral meshes. The performance and effectiveness are compared with the CBC based on one-dimensional Euler equations. Then a two cylinder case is employed to test the performance of three boundary conditions with complex geometries and vortex dominant flow.

The rest of the paper is organized as follows. In the next section, the formulation of the spectral difference method is briefly reviewed. In sections 3 and 4, the ASZ and PML approaches used in the spectral difference method are presented with the unstructured hexahedral mesh. In section 5, numerical tests are presented and discussed. Concluding remarks are given in section 6.

2. Review of the Multi-domain Spectral Difference Method

2.1 Governing equations

Consider the three-dimensional compressible non-linear Navier-Stokes equations written in the conservation form as

$$\frac{\partial Q}{\partial t}+\frac{\partial F}{\partial x}+\frac{\partial G}{\partial y}+\frac{\partial H}{\partial z}=0 \tag{2.1a}$$

on domain $\Omega \times [0,T]$ and $\Omega \subset R^3$ with the initial condition

$$Q(x,y,z,0)=Q_0(x,y,z) \tag{2.1b}$$

and appropriate boundary conditions on $\partial\Omega$. In (2.1), x, y, and z are the Cartesian coordinates and $(x,y,z)\in\Omega$, $t\in[0,T]$ denotes time. Q is the vector of conserved variables, and F, G and H are the fluxes in the x, y and z directions, respectively, which take the following form

$$Q=\begin{Bmatrix}\rho\\ \rho u\\ \rho v\\ \rho w\\ E\end{Bmatrix} \tag{2.1c}$$

$$F=F^i-F^v=\begin{Bmatrix}\rho u\\ \rho u^2+p\\ \rho uv\\ \rho uw\\ (E+p)u\end{Bmatrix}-\begin{Bmatrix}0\\ \tau_{xx}\\ \tau_{xy}\\ \tau_{xz}\\ u\tau_{xx}+v\tau_{xy}+w\tau_{xz}-q_x\end{Bmatrix} \tag{2.1d}$$

$$G = G^i - G^v = \begin{Bmatrix} \rho v \\ \rho uv \\ \rho v^2 + p \\ \rho vw \\ (E+p)v \end{Bmatrix} - \begin{Bmatrix} 0 \\ \tau_{xy} \\ \tau_{yy} \\ \tau_{yz} \\ u\tau_{xy} + v\tau_{yy} + w\tau_{yz} - q_y \end{Bmatrix} \tag{2.1e}$$

$$H = H^i - H^v = \begin{Bmatrix} \rho w \\ \rho uw \\ \rho vw \\ \rho w^2 + p \\ (E+p)w \end{Bmatrix} - \begin{Bmatrix} 0 \\ \tau_{xz} \\ \tau_{yz} \\ \tau_{zz} \\ u\tau_{xz} + v\tau_{yz} + w\tau_{zz} - q_z \end{Bmatrix} \tag{2.1f}$$

with the total energy written as

$$E = \frac{p}{\gamma - 1} + \frac{1}{2}\rho(u^2 + v^2 + w^2)$$

viscous stress terms written as

$$\tau_{xx} = 2\mu\frac{\partial u}{\partial x} - \frac{2}{3}\mu\left(\frac{\partial u}{\partial x} + \frac{\partial v}{\partial y} + \frac{\partial w}{\partial z}\right)$$

$$\tau_{yy} = 2\mu\frac{\partial v}{\partial y} - \frac{2}{3}\mu\left(\frac{\partial u}{\partial x} + \frac{\partial v}{\partial y} + \frac{\partial w}{\partial z}\right)$$

$$\tau_{zz} = 2\mu\frac{\partial w}{\partial z} - \frac{2}{3}\mu\left(\frac{\partial u}{\partial x} + \frac{\partial v}{\partial y} + \frac{\partial w}{\partial z}\right)$$

$$\tau_{xy} = \mu\left(\frac{\partial u}{\partial y} + \frac{\partial v}{\partial x}\right), \tau_{xz} = \mu\left(\frac{\partial u}{\partial z} + \frac{\partial w}{\partial x}\right), \tau_{yz} = \mu\left(\frac{\partial w}{\partial y} + \frac{\partial v}{\partial z}\right)$$

and heat transfer terms

$$q_x = -k\frac{\partial T}{\partial x}, q_y = -k\frac{\partial T}{\partial y}, q_z = -k\frac{\partial T}{\partial z}$$

where $\{\rho, u, v, w, p\}$ are the primitive variables of density, velocities and pressure, μ is coefficient of viscosity and k is the coefficient of thermal.

2.2 Coordinate transformation

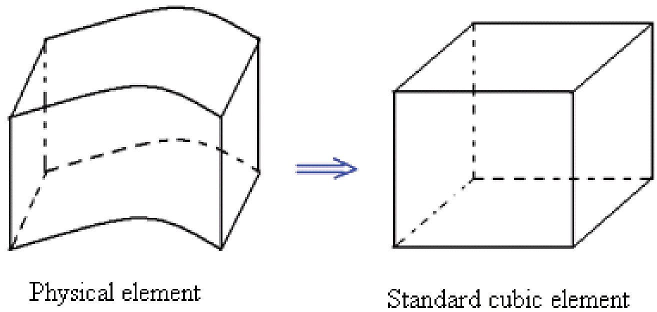

Fig. 1. Transformation from a physical element to a standard element

In the SD method, it is assumed that the computational domain is divided into non-overlapping unstructured hexahedral cells or elements. In order to handle curved boundaries, both linear and quadratic isoparametric elements are employed, with linear elements used in the interior domain and quadratic elements used near high-order curved boundaries. In order to achieve an efficient implementation, all physical elements (x, y, z) are transformed into standard cubic element $(\xi, \eta, \varsigma) \in [-1,1] \times [-1,1] \times [-1,1]$ as shown in Fig. 1.

The transformation can be written as

$$\begin{bmatrix} x \\ y \\ z \end{bmatrix} = \sum_{i=1}^{K} M_i(\xi, \eta, \varsigma) \begin{bmatrix} x_i \\ y_i \\ z_i \end{bmatrix} \tag{2.2}$$

where K is the number of points used to define the physical element, (x_i, y_i, z_i) are the Cartesian coordinates of these points, and $M_i(\xi, \eta, \varsigma)$ are the shape functions. For the transformation given in (2.2), the Jacobian matrix J takes the following form

$$J = \frac{\partial(x,y,z)}{\partial(\xi,\eta,\varsigma)} = \begin{bmatrix} x_\xi & x_\eta & x_\varsigma \\ y_\xi & y_\eta & y_\varsigma \\ z_\xi & z_\eta & z_\varsigma \end{bmatrix}.$$

The governing equations in the physical domain are then transformed into the standard element, and the transformed equations take the following form

$$\frac{\partial \tilde{Q}}{\partial t} + \frac{\partial \tilde{F}}{\partial \xi} + \frac{\partial \tilde{G}}{\partial \eta} + \frac{\partial \tilde{H}}{\partial \varsigma} = 0 \tag{2.3}$$

where

$$\tilde{Q} = |J| \cdot Q$$

$$\begin{bmatrix}\tilde{F}\\ \tilde{G}\\ \tilde{H}\end{bmatrix} = |J|\begin{bmatrix}\xi_x & \xi_y & \xi_z\\ \eta_x & \eta_y & \eta_z\\ \varsigma_x & \varsigma_y & \varsigma_z\end{bmatrix}\cdot\begin{bmatrix}F\\ G\\ H\end{bmatrix}$$

2.3 Spatial Discretization

In the standard element, two sets of points are defined, namely the solution points and the flux points, illustrated in Fig. 2 for a 2D element. The solution unknowns (conserved variables Q) or degrees-of-freedoms (DOFs) are stored at the solution points, while fluxes are computed at the flux points. The solution points in 1D are chosen to be the Chebyshev-Gauss points defined by

$$X_s = -cos\left(\frac{2s-1}{2N}\cdot\pi\right), s = 1,2,\cdots,N. \tag{2.4}$$

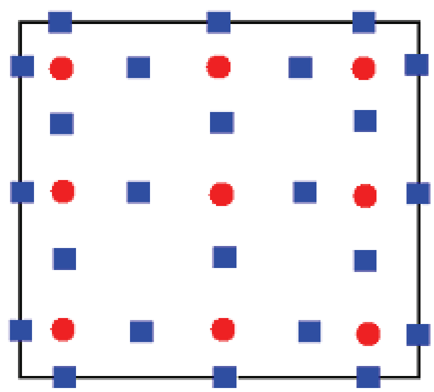

Fig. 2. Distribution of solution points (circles) and flux points (squares) in a standard element for a 3rd-order SD scheme.

With solutions at N points, we can construct a degree $(\mathrm{N}-1)$ polynomial in each coordinate direction using the following Lagrange basis defined as

$$h_i(X) = \prod_{s=1,s\neq i}^{N}\left(\frac{X-X_s}{X_i-X_s}\right) \tag{2.5}$$

The reconstructed solution for the conserved variables in the standard element is just the tensor products of the three one-dimensional polynomials, i.e.,

$$Q(\xi,\eta,\varsigma) = \sum_{k=1}^{N}\sum_{j=1}^{N}\sum_{i=1}^{N}\frac{\tilde{Q}_{i,j,k}}{|J_{i,j,k}|}h_i(\xi)\cdot h_j(\eta)\cdot h_k(\varsigma) \tag{2.6}$$

The flux points in 1D are chosen to be the $(\mathrm{N}-1)$ Legendre-Gauss quadrature points plus the two end points, -1 and 1. With fluxes at $(\mathrm{N}+1)$ points, a degree N polynomial can be constructed in each coordinate direction using the following Lagrange bases defined as

$$l_{i+1/2}(X)=\prod_{s=0,s\neq i}^{N}\left(\frac{X-X_{s+1/2}}{X_{i+1/2}-X_{s+1/2}}\right) \tag{2.7}$$

Similarly, the reconstructed flux polynomials take the following form:

$$\tilde{F}(\xi,\eta,\varsigma)=\sum_{k=1}^{N}\sum_{j=1}^{N}\sum_{i=0}^{N}\tilde{F}_{i+1/2,j,k}\,l_{i+1/2}(\xi)\cdot h_j(\eta)\cdot h_k(\varsigma) \tag{2.8a}$$

$$\tilde{G}(\xi,\eta,\varsigma)=\sum_{k=1}^{N}\sum_{j=0}^{N}\sum_{i=1}^{N}\tilde{G}_{i,j+1/2,k}\,h_i(\xi)\cdot l_{j+1/2}(\eta)\cdot h_k(\varsigma) \tag{2.8b}$$

$$\tilde{H}(\xi,\eta,\varsigma)=\sum_{k=0}^{N}\sum_{j=1}^{N}\sum_{i=1}^{N}\tilde{H}_{i,j,k+1/2}\,h_i(\xi)\cdot h_j(\eta)\cdot l_{k+1/2}(\varsigma) \tag{2.8c}$$

Because the SD method is based on the differential form of the governing equations, the implementation is straightforward even for high-order curved boundaries. All the operations are basically one-dimensional in each coordinate direction and each coordinate direction shares the collocated solution points with others, resulting in improved efficiency. In summary, the algorithm to compute the inviscid flux and viscous flux and update the unknowns (DOFs) consists the following steps:

1. Given the conserved variables $\{Q_{i,j,k}\}$ at the solution points, compute the conserved variables $\{Q_{i+1/2,j,k}\}$ at the flux points using polynomial (2.6).
2. Note that inviscid flux is a function of the conserved solution and the viscous flux is a function of both the conserved solution and its gradient, taking flux $\tilde{F}$ for example:

$$\begin{cases}\tilde{F}=\tilde{F}^i-\tilde{F}^v\\ \tilde{F}^i_{i+1/2,j,k}=\tilde{F}^i\left(Q_{i+1/2,j,k}\right)\\ \tilde{F}^v_{i+1/2,j,k}=\tilde{F}^v\left(Q_{i+1/2,j,k},\nabla Q_{i+1/2,j,k}\right)\end{cases} \tag{2.9}$$

Compute the inviscid fluxes $\{\tilde{F}^i_{i+1/2,j,k}\}$ at the interior flux points using the solution $\{Q_{i+1/2,j,k}\}$ computed at Step 1. Compute the viscous fluxes $\{\tilde{F}^v_{i+1/2,j,k}\}$ using the solution $\{Q_{i+1/2,j,k}\}$ computed at Step 1 and the gradient of the solutions $\{\nabla Q_{i+1/2,j,k}\}$ computed based on $\{Q_{i+1/2,j,k}\}$.

3. Compute the common inviscid flux at element interfaces using a Riemann solver (2.11), such as the Roe solver [55] and Russanov solver [57].

$$\tilde{F}^i = \tilde{F}^i(Q_L, Q_R) \tag{2.11}$$

where Q_L and Q_R represent the solutions from the two elements beside the interface. Compute the common viscous flux at element interfaces using a viscous approach (2.12), such as the averaged approach and DG-like approach [57].

$$\tilde{F}^v = \tilde{F}^v(Q_L, Q_R, \nabla Q_L, \nabla Q_R) \tag{2.12}$$

Then compute the derivatives of the fluxes at all the solution points by using (2.13).

$$\left(\frac{\partial \tilde{F}}{\partial \xi}\right)_{i,j,k} = \sum_{r=0}^{N} \tilde{F}_{r+1/2,j,k}\, l'_{r+1/2}(\xi_i) \tag{2.13a}$$

$$\left(\frac{\partial \tilde{G}}{\partial \eta}\right)_{i,j,k} = \sum_{r=0}^{N} \tilde{G}_{i,r+1/2,k}\, l'_{r+1/2}(\eta_j) \tag{2.13b}$$

$$\left(\frac{\partial \tilde{H}}{\partial \varsigma}\right)_{i,j,k} = \sum_{r=0}^{N} \tilde{H}_{i,j,r+1/2}\, l'_{r+1/2}(\varsigma_k) \tag{2.13c}$$

4. Update the DOFs using a multistage TVD scheme for time integration of (2.14).

$$\frac{\partial \tilde{Q}_{i,j,k}}{\partial t} = -\left(\frac{\partial \tilde{F}}{\partial \xi} + \frac{\partial \tilde{G}}{\partial \eta} + \frac{\partial \tilde{H}}{\partial \varsigma}\right)_{i,j,k} \tag{2.14}$$

For more details about SD method on hexahedral mesh, the readers can refer to [57].

3. Formulation of the absorbing sponge zone (ASZ)

The ASZ technique is a widely used absorbing boundary condition in the computational aeroacoustic community. In generalized coordinates, the conservative form of the Navier-Stokes equations with additional source terms in ASZ domain can be expressed as

$$\frac{\partial \tilde{Q}}{\partial t} + \frac{\partial \tilde{F}}{\partial \xi} + \frac{\partial \tilde{G}}{\partial \eta} + \frac{\partial \tilde{H}}{\partial \varsigma} = -\tilde{S} \tag{3.1}$$

where

$$\tilde{S} = |J| \cdot S$$

$$S = \sigma(Q - \bar{Q}) = \sigma \begin{Bmatrix} \rho - \bar{\rho} \\ \rho u - \overline{\rho u} \\ \rho v - \overline{\rho v} \\ \rho w - \overline{\rho w} \\ E - \bar{E} \end{Bmatrix}$$ and σ is the absorbing coefficient.

Basically, there are two choices for the proposed solution $\overline{\mathrm{Q}}$ in ASZ domain. One is to choose $\overline{\mathrm{Q}}$ to be the far field values, and the CBC is usually used at the boundary of the ASZ domain. In this paper, all the numerical cases with ASZ choose this one. The other one is to set $\overline{\mathrm{Q}}$ to be a supersonic uniform flow, and the boundary condition at the end of the ASZ domain can simply be the extrapolation boundary condition.

The effectiveness of the ASZ can be roughly shown as follows. Take the 1st-order Euler method for example. Let $\mathrm{Q}_{\mathrm{i,j,k}}^{\mathrm{n+1}}$ and $\mathrm{Q}_{\mathrm{i,j,k}}^{\mathrm{n+1}^*}$ be the numerical solutions of the Navier-Stokes equation with and without the source term respectively, then

$$Q_{i,j,k}^{n+1} = Q_{i,j,k}^{n} - \Delta t \left(S + \frac{\partial F}{\partial x} + \frac{\partial G}{\partial y} + \frac{\partial H}{\partial z} \right)_{i,j,k}^{n} \tag{3.2}$$

$$Q_{i,j,k}^{n+1^*} = Q_{i,j,k}^{n} - \Delta t \left(\frac{\partial F}{\partial x} + \frac{\partial G}{\partial y} + \frac{\partial H}{\partial z} \right)_{i,j,k}^{n}. \tag{3.3}$$

There are three possible cases:

1) If $Q_{i,j,k}^{n} > \bar{Q}_{i,j,k}^{n}$ then S= $\sigma\left(Q_{i,j,k}^{n} - \bar{Q}_{i,j,k}^{n}\right) > 0$ such that $Q_{i,j,k}^{n+1} < Q_{i,j,k}^{n+1^*}$.
2) If $Q_{i,j,k}^{n} < \bar{Q}_{i,j,k}^{n}$ then S= $\sigma\left(Q_{i,j,k}^{n} - \bar{Q}_{i,j,k}^{n}\right) < 0$ such that$Q_{i,j,k}^{n+1} > Q_{i,j,k}^{n+1^*}$.
3) If $Q_{i,j,k}^{n} = \bar{Q}_{i,j,k}^{n}$ then S= $\sigma\left(Q_{i,j,k}^{n} - \bar{Q}_{i,j,k}^{n}\right) = 0$ such that $Q_{i,j,k}^{n+1} = Q_{i,j,k}^{n+1^*}$.

The source term $\mathrm{S} = \sigma(\mathrm{Q} - \overline{\mathrm{Q}})$ adjusts the solution Q gradually approaching to $\overline{\mathrm{Q}}$ as in case 1) and 2) till the solution Q is tuned to the proposed solution $\overline{\mathrm{Q}}$ inside the ASZ domain as in case 3).

The coefficient σ is zero in the physical domain and grows smoothly in the ASZ domain to a specified value at the boundaries in order to minimize the reflection generated at the interfaces between the physical domain and the ASZ domain. Here, a basic sponge coefficient profile for a cuboid mesh with smooth blending over the corners can be given by

$$\sigma = \sigma(x, y, z) = \sigma_0 \{1 + cos[\pi A(x)B(y)C(z)]\}/2 \tag{3.4}$$

where

$$x \in [x_{min}, x_{max}] \;\&\; y \in [y_{min}, y_{max}] \;\&\; z \in [z_{min}, z_{max}]$$

$$\begin{cases} A(x) = 1 - max[1 - (x - x_{min})/L_x\,, 0] - max[1 - (x_{max} - x)/L_x\,, 0] \\ B(y) = 1 - max[1 - (y - y_{min})/L_y\,, 0] - max[1 - (y_{max} - y)/L_y\,, 0] \\ C(z) = 1 - max[1 - (z - z_{min})/L_z\,, 0] - max[1 - (z_{max} - z)/L_z\,, 0] \end{cases}$$

and L_x, L_y, L_z respresent the width of the ASZ domain in each coordinate direction

4. Formulation of perfectly matched layer (PML)

The PML technique is an effective absorbing boundary condition to truncate the physical domain [37,38,39]. The equations in the PML domain are formulated so that the amplitude of the out-going waves $\mathrm{Q}' = \mathrm{Q} - \overline{\mathrm{Q}}$ entering the PML domain can be exponentially reduced while causing as little numerical reflection as possible, thus the extrapolation boundary condition can be used at the end of PML domain. A mean state of flow $\overline{\mathrm{Q}}$ satisfies (4.1) is needed for the unsteady flow variables Q to reduce to. Equation (4.2) is obtained by subtracting the mean state equations (4.1) from the original Navier-Stokes Equations (2.1a).

$$\frac{\partial F(\bar{Q})}{\partial x} + \frac{\partial G(\bar{Q})}{\partial y} + \frac{\partial H(\bar{Q})}{\partial z} = 0 \tag{4.1}$$

$$\frac{\partial Q'}{\partial t} + \frac{\partial (F - F(\bar{Q}))}{\partial x} + \frac{\partial (G - G(\bar{Q}))}{\partial y} + \frac{\partial (H - H(\bar{Q}))}{\partial z} = 0 \tag{4.2}$$

A three-step transformation process to formulate the PML equations based on (4.2) is described in [39], assuming the mainstream is in x-direction:

a. A proper space-time transformation

$$\bar{t} = t + \beta x$$

$$\frac{\partial}{\partial t} \to \frac{\partial}{\partial \bar{t}}, \qquad \frac{\partial}{\partial x} \to \frac{\partial}{\partial x} + \beta \frac{\partial}{\partial \bar{t}}$$

b. A PML change of variables in the frequency domain

$$\frac{\partial}{\partial x} \to \frac{1}{1 + i\frac{\sigma_x}{\omega}} \frac{\partial}{\partial x}, \qquad \frac{\partial}{\partial y} \to \frac{1}{1 + i\frac{\sigma_y}{\omega}} \frac{\partial}{\partial y}, \qquad \frac{\partial}{\partial z} \to \frac{1}{1 + i\frac{\sigma_z}{\omega}} \frac{\partial}{\partial z}$$

c. A transformation from the frequency domain equation to the time domain equation

The PML equations (4.3) are obtained by following the above steps. The detailed derivation and description of PML equations can be found in [39].

$$\frac{\partial(Q-\bar{Q})}{\partial t}+\frac{\partial(F-\bar{F})}{\partial x}+\frac{\partial(G-\bar{G})}{\partial y}+\frac{\partial(H-\bar{H})}{\partial z}+\sigma_x q_1+\sigma_y q_2+\sigma_z q_3+\beta\sigma_x(F-\bar{F})=0 \quad (4.3a)$$

$$\frac{\partial q_1}{\partial t}+\frac{\partial(F-\bar{F})}{\partial x}+\sigma_x q_1+\beta\sigma_x(F-\bar{F})=0 \quad (4.3b)$$

$$\frac{\partial q_2}{\partial t}+\frac{\partial(G-\bar{G})}{\partial y}+\sigma_y q_2=0 \quad (4.3c)$$

$$\frac{\partial q_3}{\partial t}+\frac{\partial(H-\bar{H})}{\partial z}+\sigma_z q_3=0 \quad (4.3d)$$

$$\frac{\partial r_1}{\partial t}+\sigma_x r_1=\frac{\partial(U-\bar{U})}{\partial x}+\beta\sigma_x(U-\bar{U}) \quad (4.3e)$$

$$\frac{\partial r_2}{\partial t}+\sigma_y r_2=\frac{\partial(U-\bar{U})}{\partial y} \quad (4.3f)$$

$$\frac{\partial r_3}{\partial t}+\sigma_z r_3=\frac{\partial(U-\bar{U})}{\partial z} \quad (4.3g)$$

$$e_1=\frac{\partial U}{\partial x}-\sigma_x r_1+\beta\sigma_x(U-\bar{U}) \quad (4.3h)$$

$$e_2=\frac{\partial U}{\partial y}-\sigma_y r_2 \quad (4.3i)$$

$$e_3=\frac{\partial U}{\partial z}-\sigma_z r_3 \quad (4.3j)$$

where

$$\bar{F}=\ F(\bar{Q}), \bar{F}=\ G(\bar{Q}), \bar{H}=\ H(\bar{Q})$$

and $U=(u,v,w,T)$ are the variables whose spatial derivative are present in the viscous flux vectors.

The PML Equations (4.3) are valid only in the PML region as shown in Fig. 3. In [39], the PML absorption coefficient in x direction is taken to be

$$\sigma_x=\sigma_{max}\left|\frac{x-x_0}{D_x}\right|^\alpha$$

$$\sigma_y=\sigma_{max}\left|\frac{y-y_0}{D_y}\right|^\alpha$$

$$\sigma_z=\sigma_{max}\left|\frac{z-z_0}{D_z}\right|^\alpha$$

where σ_{max} and α are absorbing parameters, $\{x_0, y_0, z_0\}$ are the locations of interface between the PML and physical domains, and $\{D_{x,}, D_y, D_z\}$ are the width of the PML domain as shown in Fig. 3. The absorption coefficients in the other two directions are defined in a similar way. And β is given by a simple empirical formula [39],

$$\beta = \frac{u_0}{1 - u_0^2}$$

where

$$u_0 = \frac{1}{b-a}\int_a^b \bar{u}(y)\,dy$$

assuming the computational domain for y direction is $[a, b]$ and $\bar{u}(y)$ is the mean velocity in x direction.

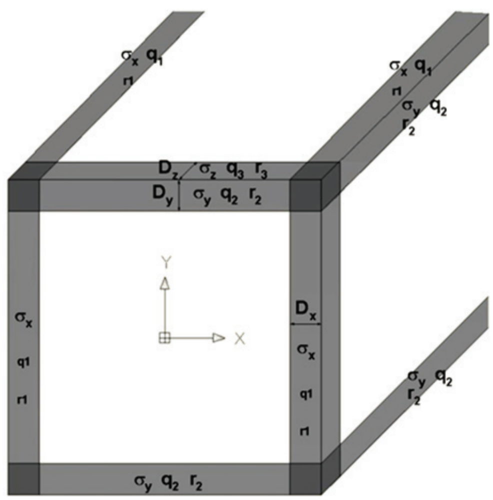

Fig. 3. The schematics of the physical and PML domains. The sub-domains where the absorption coefficients are non-zero are indicated by arrows.

As the PML equations (4.3) are derived and designed within Cartesian coordinates, the new unknowns $\{q_1, q_2, q_3\}$ and $\{r_1, r_2, r_3\}$ are actually split variables in $\{x, y, z\}$ directions respectively. To apply the PML technique in the SD method with hexahedral mesh, the hexahedral mesh inside the PML domain is designed to be orthogonal such that the PML equation (4.3) can be used directly under transformation (4.4).

$$J^{-1} = \frac{\partial(\xi, \eta, \varsigma)}{\partial(x, y, z)} = \begin{bmatrix} \xi_x & 0 & 0 \\ 0 & \eta_y & 0 \\ 0 & 0 & \varsigma_z \end{bmatrix} \tag{4.4}$$

In this way, the PML equation in the PML domain for SD method can be written as

$$\frac{\partial(\tilde{Q}-\tilde{\bar{Q}})}{\partial t}+\frac{\partial(\tilde{F}-\tilde{\bar{F}})}{\partial \xi}+\frac{\partial(\tilde{G}-\tilde{\bar{G}})}{\partial \eta}+\frac{\partial(\tilde{H}-\tilde{\bar{H}})}{\partial \varsigma}+\sigma_x\tilde{q}_1+\sigma_y\tilde{q}_2+\sigma_z\tilde{q}_3+\beta\sigma_x\tilde{S}_0 = 0 \qquad (4.5a)$$

$$\frac{\partial \tilde{q}_1}{\partial t}+\frac{\partial(\tilde{F}-\tilde{\bar{F}})}{\partial \xi}+\sigma_x\tilde{q}_1+\beta\sigma_x\tilde{S}_0=0 \qquad (4.5b)$$

$$\frac{\partial \tilde{q}_2}{\partial t}+\frac{\partial(\tilde{G}-\tilde{\bar{G}})}{\partial \eta}+\sigma_y\tilde{q}_2=0 \qquad (4.5c)$$

$$\frac{\partial \tilde{q}_3}{\partial t}+\frac{\partial(\tilde{H}-\tilde{\bar{H}})}{\partial \varsigma}+\sigma_z\tilde{q}_3=0 \qquad (4.5d)$$

$$\frac{\partial \tilde{r}_1}{\partial t}+\sigma_x\tilde{r}_1=\frac{\partial(\tilde{U}-\tilde{\bar{U}})}{\partial \xi}+\beta\sigma_x\tilde{S}_1 \qquad (4.5e)$$

$$\frac{\partial \tilde{r}_2}{\partial t}+\sigma_y\tilde{r}_2=\frac{\partial(\tilde{U}-\tilde{\bar{U}})}{\partial \eta} \qquad (4.5f)$$

$$\frac{\partial \tilde{r}_3}{\partial t}+\sigma_z\tilde{r}_3=\frac{\partial(\tilde{U}-\tilde{\bar{U}})}{\partial \varsigma} \qquad (4.5g)$$

$$\tilde{e}_1=\frac{\partial \tilde{U}}{\partial \xi}-\sigma_x\tilde{r}_1+\beta\sigma_x\tilde{S}_1 \qquad (4.5h)$$

$$\tilde{e}_2=\frac{\partial \tilde{U}}{\partial \eta}-\sigma_y\tilde{r}_2 \qquad (4.5i)$$

$$\tilde{e}_3=\frac{\partial \tilde{U}}{\partial \varsigma}-\sigma_z\tilde{r}_3 \qquad (4.5j)$$

where

$$\left(\tilde{Q}-\tilde{\bar{Q}}\right)=|J|\cdot(Q-\bar{Q})$$

$$\tilde{S}_0=|J|\cdot(F-\bar{F})$$

$$\begin{bmatrix}\tilde{F}-\tilde{\bar{F}}\\ \tilde{G}-\tilde{\bar{G}}\\ \tilde{H}-\tilde{\bar{H}}\end{bmatrix}=|J|\begin{bmatrix}\xi_x & 0 & 0\\ 0 & \eta_y & 0\\ 0 & 0 & \varsigma_z\end{bmatrix}\cdot\begin{bmatrix}F-\bar{F}\\ G-\bar{G}\\ H-\bar{H}\end{bmatrix}$$

$$[\tilde{q}_1 \quad \tilde{q}_2 \quad \tilde{q}_3]=|J|\cdot[q_1 \quad q_2 \quad q_3]$$

$$[\tilde{r}_1 \quad \tilde{r}_2 \quad \tilde{r}_3]=|J|\cdot[r_1 \quad r_2 \quad r_3]$$

$$\tilde{S}_1=|J|\cdot(U-\bar{U})$$

In equation (4.5), the unknowns and the fluxes are discretized in the same way as in the SD method. As in Equations (4.5) the inviscid and viscous fluxes keep in the same forms as in the Navier-Stokes equations (2.1), the common inviscid flux and viscous flux at the interfaces between each two element in PML domain are computed in the same manner as the common SD method described in Section 2.

5. Numerical test

5.1 Isentropic vortex propagation

A case of isentropic vortex propagation is employed here to verify the effectiveness of ASZ and PML techniques for nonlinear Euler equations. The two-dimensional nonlinear Euler equations support an advective solution of the form

$$\begin{pmatrix} \rho \\ u \\ v \\ p \end{pmatrix} = \begin{pmatrix} \rho' \\ U_0 + u' \\ V_0 + v' \\ p' \end{pmatrix} \tag{5.1}$$

where

$$\begin{cases} \rho' = \left(1 - \frac{1}{2}(\gamma - 1)U_{max}^2 e^{1-\frac{r^2}{r_0^2}}\right)^{1/(\gamma-1)} \\ u' = -u_r sin\theta \\ v' = -u_r cos\theta \\ p' = \frac{1}{\gamma}\left(1 - \frac{1}{2}(\gamma - 1)U_{max}^2 e^{1-\frac{r^2}{r_0^2}}\right)^{1/(\gamma-1)} \end{cases}$$

$$r = \sqrt{(x - U_0 t)^2 + (y - V_0 t)^2}$$

$$(U_0, V_0) = (0.5, 0.0)$$

$$U_{max} = 0.5U_0 = 0.25$$

$$r_0 = 0.2$$

The Euler equations are solved with the 4th-order SD method in space and an explicit 3rd-order Runge-Kutta method in time. The entire computational domain is $[-1.5,1.5] \times [-1.5,1.5]$, which includes the physical domain of $[-1.0,1.0] \times [-1.0,1.0]$ and the remaining absorbing domain. The number of elements in the physical domain is 160 (resulting in 2,560 degrees-of-freedom), and in the absorbing domain 5 stretched elements are added in each direction. In this case, the mean flow $\overline{\mathrm{Q}}$ is,

$$\begin{pmatrix} \bar{\rho} \\ \bar{u} \\ \bar{v} \\ \bar{p} \end{pmatrix} = \begin{pmatrix} 1.0 \\ 0.5 \\ 0.0 \\ 1/\gamma \end{pmatrix}. \tag{5.2}$$

The performance of both ASZ and PML depends on the size of the absorbing domain and the absorption coefficient. The reflection error can be reduced by extending the length of the absorbing domain [39,71]. Here, the length of the absorbing domain is fixed to be 0.5 for both cases, and the effectiveness of the absorbing coefficient is tested. For both techniques, the choices of the optimal absorbing coefficient are definitely problem dependent. Tuning the absorption coefficients for the same problem, a bigger $\sigma_{\max}$ usually generate more reflection at the interfaces for both ASZ and PML, while a smaller $\sigma_{\max}$ may cause an incomplete absorbing process and the unabsorbed reflecting disturbances would also contaminate the physical domain.

In this case, an optimal absorption coefficient is found to be $\sigma_{\max} = 0.5$ for ASZ. And for PML, the optimal parameters of absorption coefficient in (15) are found be $\sigma_{\max} = 10$ and $\alpha = 4$. The absorption of the vortex in the absorbing domain is clearly demonstrated for ASZ in Figs. 4a-4c and for PML in Figs. 5a-5c. In Figs. 4d-4f and 5d-5f, the v-velocity profiles along $y = 0$ at time $t = 2.0,\ 3.0$ and 4.0, respectively are compared with the exact solution. It is shown that in the physical domain, the numerical solutions agree with the exact solution well for both cases. To the naked eyes, the velocity profile with PML appears to match perfectly with the analytical solution in the physical domain, while the profile with the ASZ shows a slight discrepancy. The absorbing processes are different for ASZ and PML techniques. Note that in the domain of ASZ, the vortex is attenuated gradually, and the strength of the vortex becomes very small at the end of the ASZ domain, where a CBC is applied. Obviously, outgoing waves will reflect at this boundary if the disturbance is not zero and of course the reflected error will experience the absorbing process again inside of the ASZ domain while propagating upstream. It is obvious that PML is more efficient in absorbing the disturbances. In the PML domain, the solution decays exponentially and reduces to the mean state of flow near the end of PML domain. Thus essentially no reflection is generated at the end of the PML domain with a simple extrapolation boundary condition.

Fig. 6 compares the L_∞ error (maximum error) of pressure in the physical domain computed with ASZ, PML and CBC at different times of the simulations. It is shown that the error of the numerical results generated with PML is the smallest while the error with CBC is at least one order bigger than the error with PML. The error with ASZ is between those with PML and CBC.

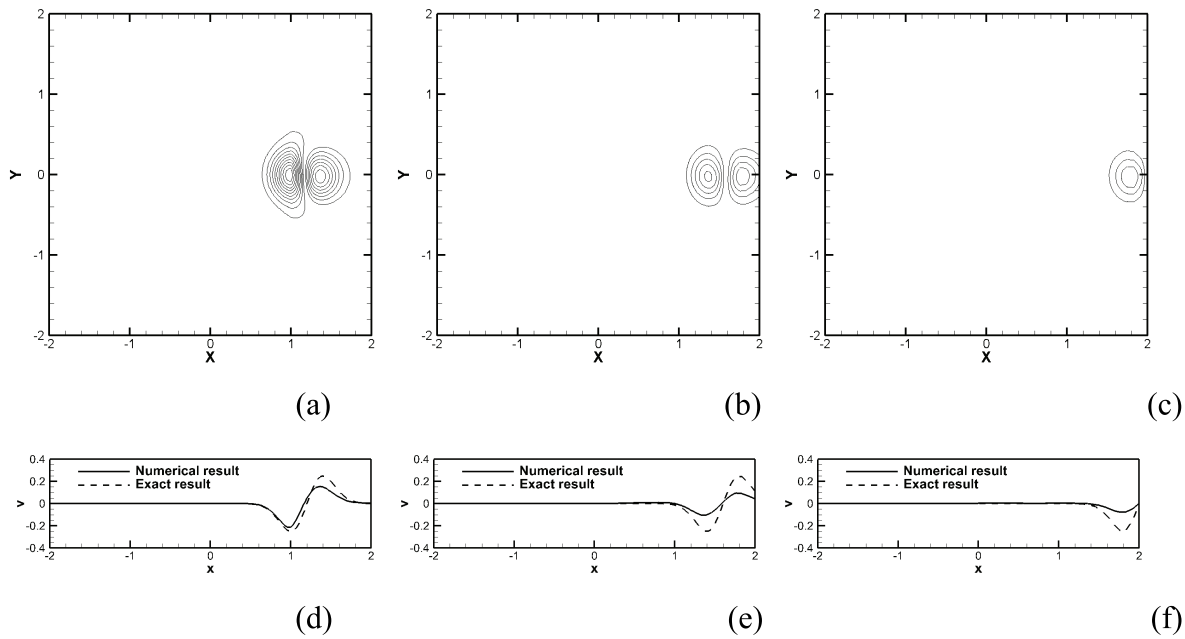

Fig. 4. The v-velocity contours (a, b c) and v-velocity profile along $y = 0$ (d, e, f) with ASZ at time $t = 2.0,\ 3.0$ and 4.0

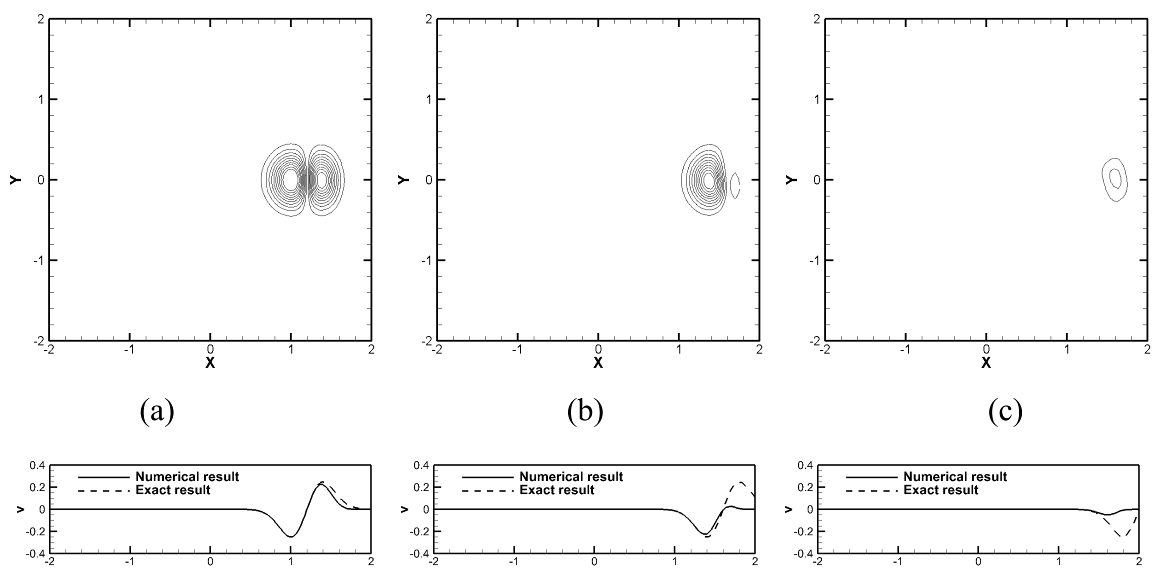

(d) (e) (f)

Fig. 5. The v-velocity contours (a, b, c) and v-velocity profile along $\mathrm{y} = 0$ (d, e, f) with PML at time $t = 2.0,\ 3.0$ and 4.0

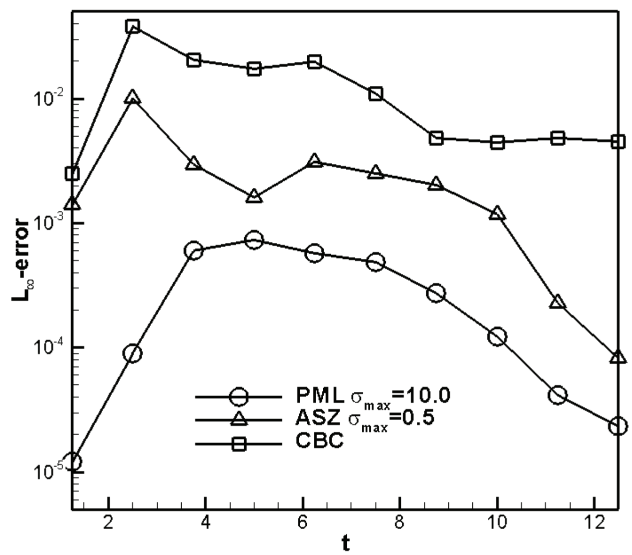

Fig. 6. Comparison of L_∞ error (maximum error) of pressure

5.2 3-D acoustic pulse

The propagation of a three dimensional nonlinear acoustic pulse in a uniform mean flow is employed to test the performance and effectiveness of absorbing boundary conditions with non-linear Navier-Stokes equations. The absorbing domains are applied in all boundaries of the cubic physical domain. The computational results with the CBC are also presented here for comparison. The initial condition is as follows:

$$\begin{cases} \rho = 1 + P'_{max} e^{-ln2\left(x^2+y^2+z^2\right)/r_0^2} \\ u = U_0 \\ v = 0 \\ w = 0 \\ \rho = 1/\gamma + P'_{max} e^{-ln2\left(x^2+y^2+z^2\right)/r_0^2} \end{cases} \tag{5.3}$$

where

$$\gamma = 1.4, r_0 = 1.0, U_0 = 0.5, P'_{max} = 0.5.$$

The Reynolds number in this case is 500. The proposed reference solution $\overline{\mathrm{Q}}$ in both the ASZ and PML is

$$\begin{pmatrix} \bar{\rho} \\ \bar{u} \\ \bar{v} \\ \bar{w} \\ \bar{p} \end{pmatrix} = \begin{pmatrix} 1.0 \\ 0.5 \\ 0.0 \\ 0.0 \\ 1/\gamma \end{pmatrix} \tag{5.4}$$

The physical domain is $[-10,10] \times [-10,10] \times [-10,10]$ with a uniform mesh of 20 elements in each coordinate direction. For the zonal techniques, a stretched grid with 3 elements is used in each coordinate direction. The 4th-order SD method and an explicit 3rd-order Runge-Kutta method are used for spatial discretization and time integration respectively. Different absorbing coefficients are tested for both the ASZ and PML.

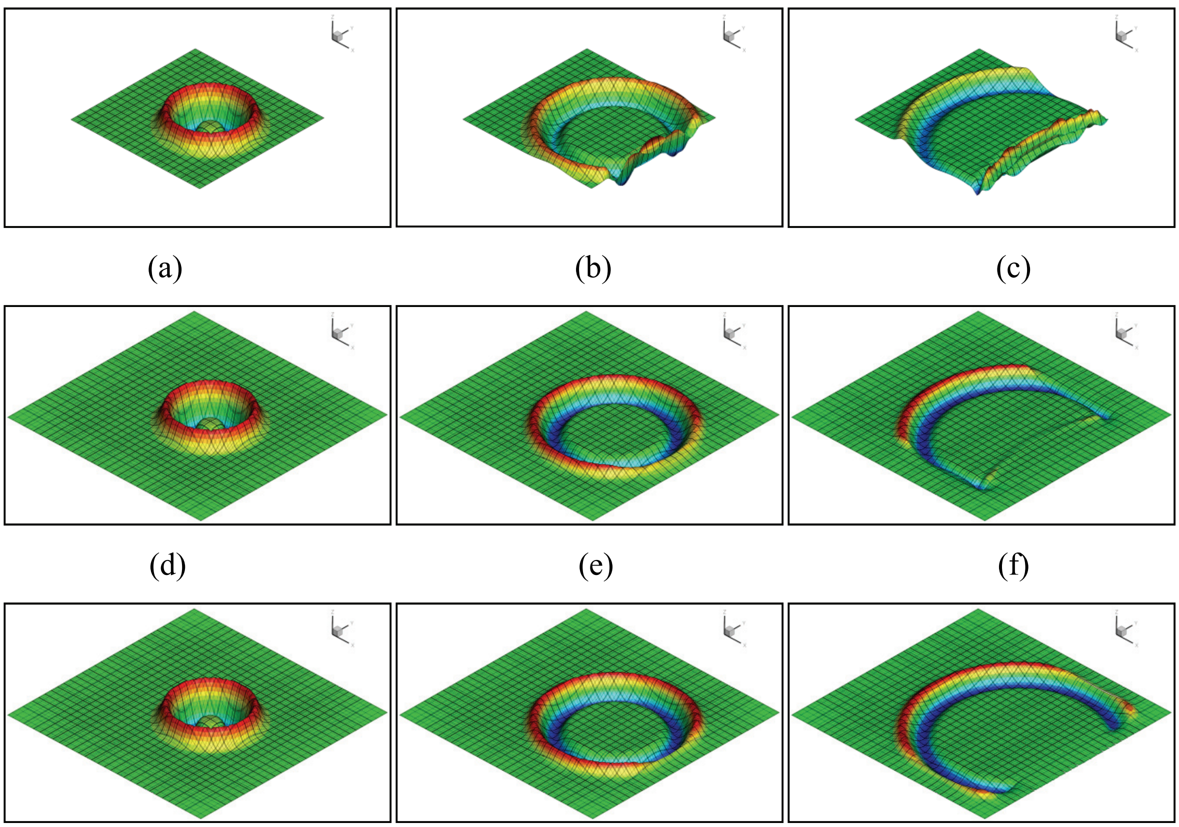

(a) (b) (c)

(d) (e) (f)

(g) (h) (i)

Fig. 7. Pressure contours with CBC (a-c), ASZ (d-f) and PML (g-i) at time $\mathrm{t} = 4.0,\ 8.0$ and 12.0

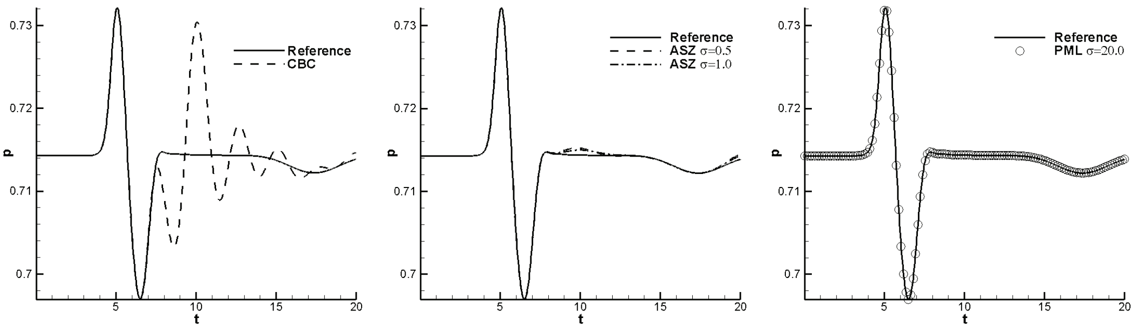

(a) (b) (c)

Fig. 8. Time history of pressure at point $(x, y, z) = (8.5,0.5,0.5)$ with CBC (a), ASZ (b) and PML (c)

Fig. 7 shows the pressure contours in the $\mathrm{X-Y}$ plane with CBC (a, b, c), ASZ (d, e, f) and PML (g, h, i) at time $\mathrm{t} = 4.0,\ 8.0$ and 12.0 respectively. The absorbing coefficients used here are $\sigma_{\max} = 0.5$ for ASZ and $\sigma_{\max} = 20.0$ for PML. In Fig. 7, the Z coordinate is the pressure, which gives a three dimensional illustration of the pressure distribution. With CBC, obvious reflections are generated at the outlet boundary and contaminate the numerical solution. In the results with ASZ technique, the pressure pulse is attenuated inside the ASZ domain but a small reflecting wave is generated at the interface. The PML technique gives the best performance among all the three presented boundary conditions. The pressure pulse is well absorbed after entering the absorbing domain and the reflecting disturbance is very small and invisible.

Fig. 8 compares the pressure history at point $(\mathrm{x}, \mathrm{y}, \mathrm{z}) = (8.5,0.5,0.5)$ with a reference solution. The reference solution is computed in a computational domain of $[-20,20] \times [-20,20] \times [-20,20]$ with the same grid size. The comparisons agree well with the observations in Fig. 7.

5.3 Viscous flow over two cylinders

In the previous two numerical tests, it has been shown that PML gives the best performance in absorbing acoustic and vertical disturbances. In this example, the case of nonlinear vortices shed by a viscous low-Mach laminar flow over two side-by-side cylinders is presented to test the performance of the three boundary conditions with complex geometry inside the physical domain. Fig. 9 shows the computational mesh. The physical domain is $[-10,20] \times [-10,10]$ with a total of 5,445 elements. The absorbing domain is added around the physical domain and a stretched grid with 5 elements is used in each coordinate direction. The numerical method for the spatial discretization and time integration is the same as in the previous two cases.

The Mach number of the uniform incoming flow is $\mathrm{Ma} = 0.2$ and the Reynolds number based on the diameter of the cylinder D is $\mathrm{Re} = 200$. The center-to-center spacing of the two cylinders is $\mathrm{s} = 3\mathrm{D}$. The inlet flow and the initial condition of the flow field is set to be

$$Q_0 = \begin{pmatrix} \rho \\ u \\ v \\ p \end{pmatrix} = \begin{pmatrix} 1.0 \\ 0.2 \\ 0.0 \\ 1/\gamma \end{pmatrix} \tag{5.5}$$

Thus the proposed mean solution $\overline{\mathrm{Q}}$ in (4.1) is the uniform flow $\overline{\mathrm{Q}} = \mathrm{Q}_0$ as the natural choice for this problem.

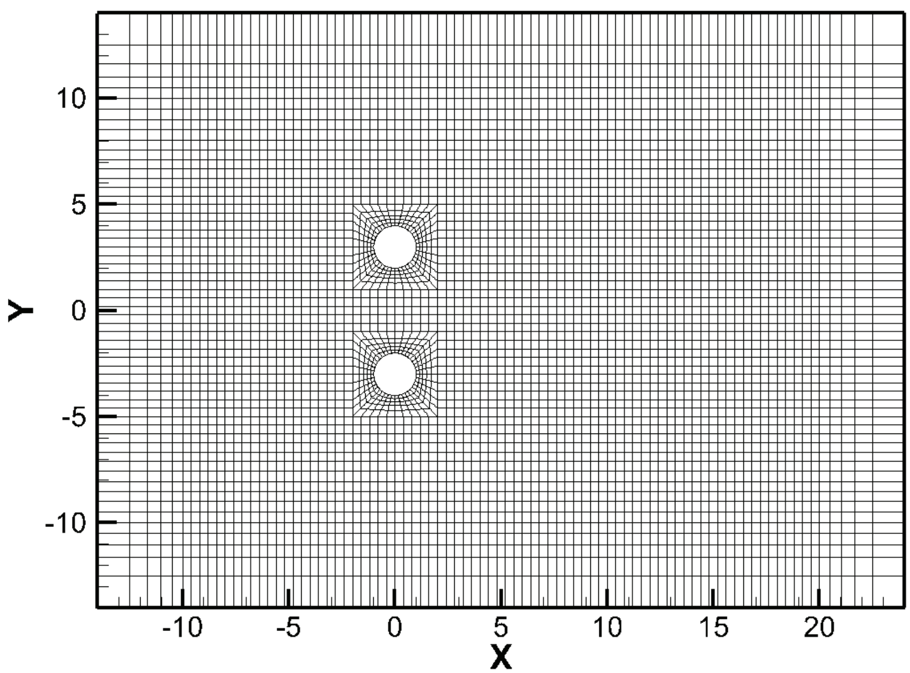

Fig. 9. Computational mesh of viscous flow over two cylinders

Optimal parameters of absorption coefficient in (15) are found be $\sigma_{\max} = 10$ and $\alpha = 4$ for PML in this case. Fig. 10 shows the vorticity contours at different times in the case with PML. The absorbing process of the shedding vortices can be observed in this Fig. from $\mathrm{t} = 280$ to $\mathrm{t} = 330$ over roughly a period. The shedding vortices are gradually absorbed as they convect out of the physical domain and enter the PML domain. Fig. 11 shows the history of v-velocity and pressure at point $(x, y) = (19.0, 3.0)$ from time $t = 300$ to $t = 600$ and compares with the reference result which is obtained in a reference physical domain $[-10, 40] \times [-20, 20]$ with PML. Excellent agreement is found, which indicates that the performance of the PML domain in absorbing the shedding vortices is very effective. Very good results have been achieved with the relatively small domain.

Fig. 12 shows the instantaneous vorticity contours in the cases with CBC and ASZ. It is noted that in current computational mesh with CBC, the boundary condition significantly affects the flow field of the physical domain and the shedding vortices lose the regular alignment as shown in Fig. 11. In the case with ASZ, the shedding vortices keep a similar pattern as the case with PML and are gradually absorbed after entering the absorbing domain. In this case, an optimal parameter of absorption coefficient is chosen to be $\sigma_{max} = 0.1$ for ASZ.

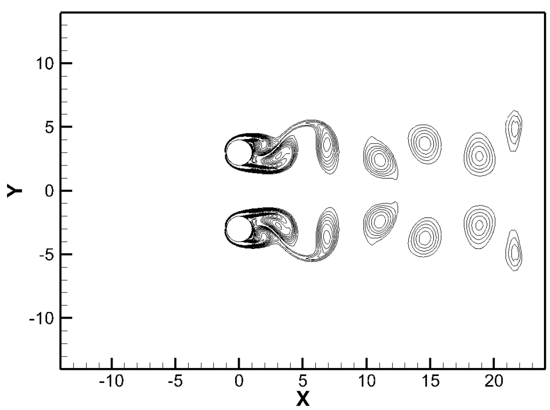

(a)

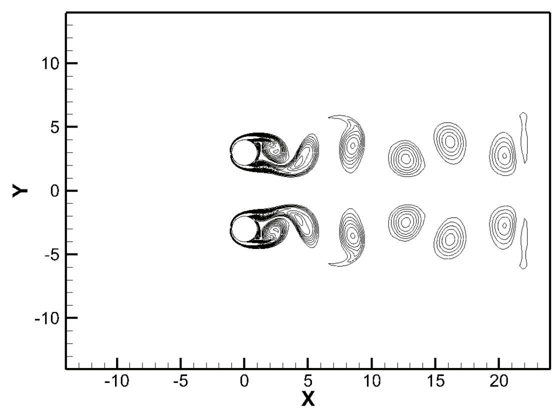

(b)

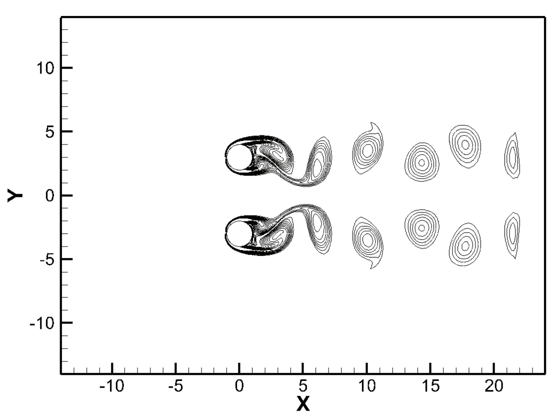

(d)

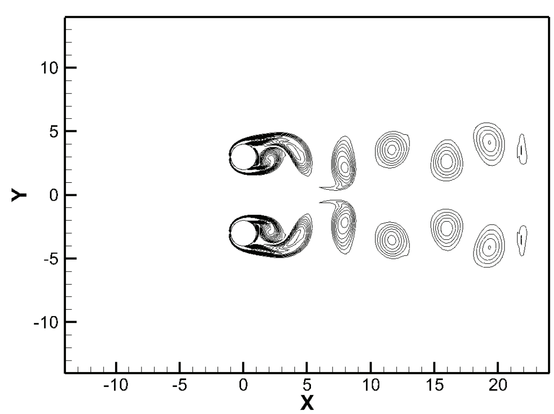

(e)

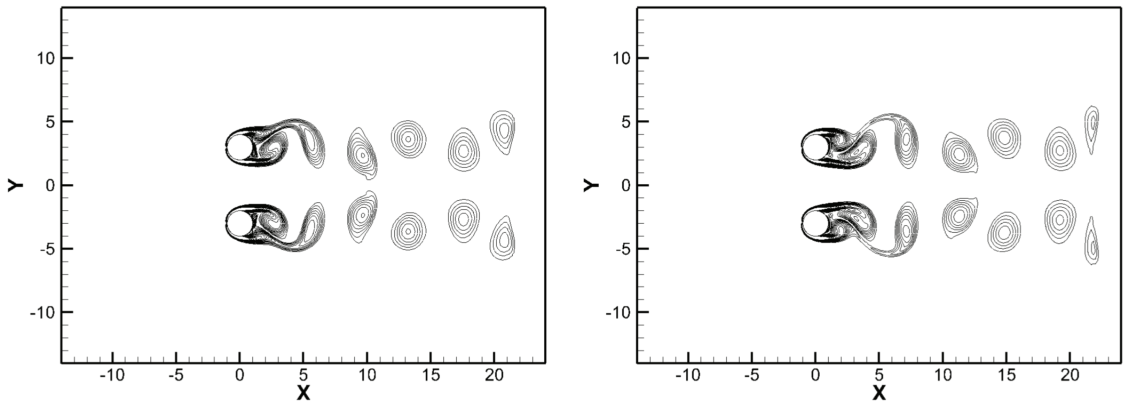

(f) (g)

Fig. 10. Vorticity contours at time $t = 280, 290, 300, 310, 320$ and 330 in the case with PML, from left to right, top to bottom

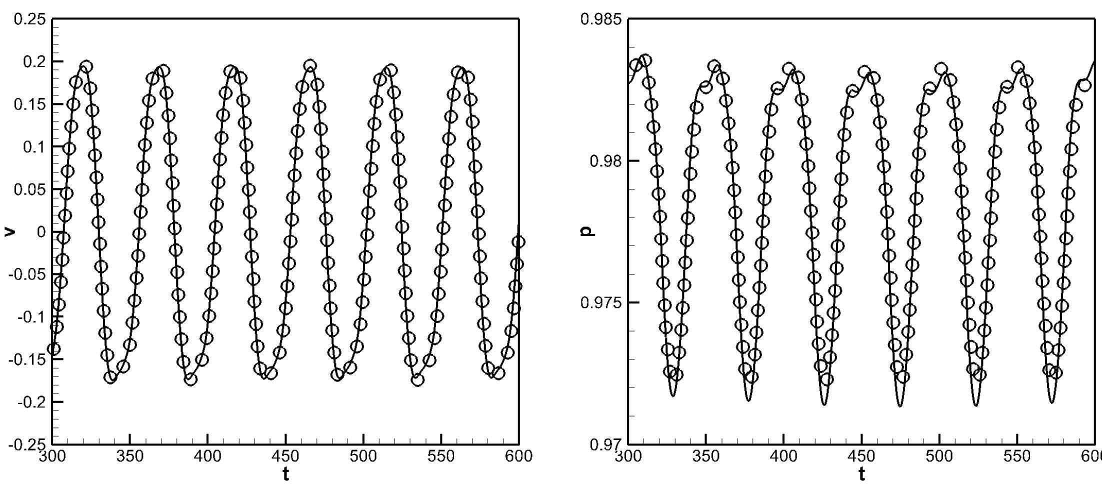

(a) (b)

Fig. 11. Time history of v-velocity (a) and pressure (b) at point $(x, y) = (19.0,3.0)$ from time $t = 300$ to $t = 600$ in the case with PML

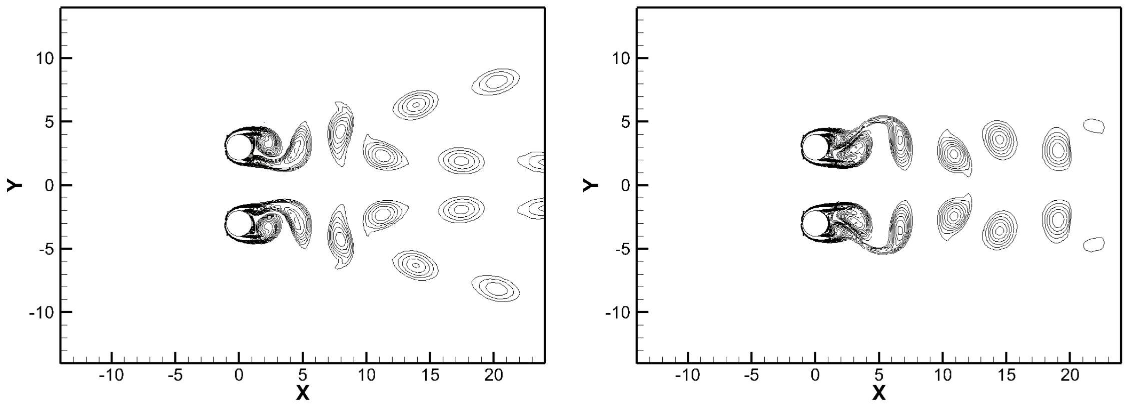

(a) (b)

Fig. 12. Instantaneous vorticity contours in the cases with CBC (a) and ASZ (b)

Here, the authors try to investigate the effect of boundary conditions on the drag and lift forces on the wall of the cylinders. Fig. 13 shows the time history of the drag coefficients for the cases with different boundary conditions. It is shown that the C_d in the case with PML agrees well with the reference results, as shown in Fig. 13(a). The current computational domain is much smaller than those used in previously published paper [17,46], and with the current mesh the boundary condition significantly affects the drag and lift forces in the cases with CBC and ASZ, as shown in Fig. 13(b). The C_d with CBC is highly oscillatory owing to the high frequency disturbances generated at the outflow boundary, while the C_d with ASZ is smooth but much higher than the results with PML. In [17], the outflow boundary is set to be far downstream of the cylinders with much larger spaced grid to dissipate the disturbances. Table 1 compares the averaged C_d of the current cases with the result in [17,46]. The current results with PML agree well with the result of Liang et al. [17] and the SD method is also used in their case.

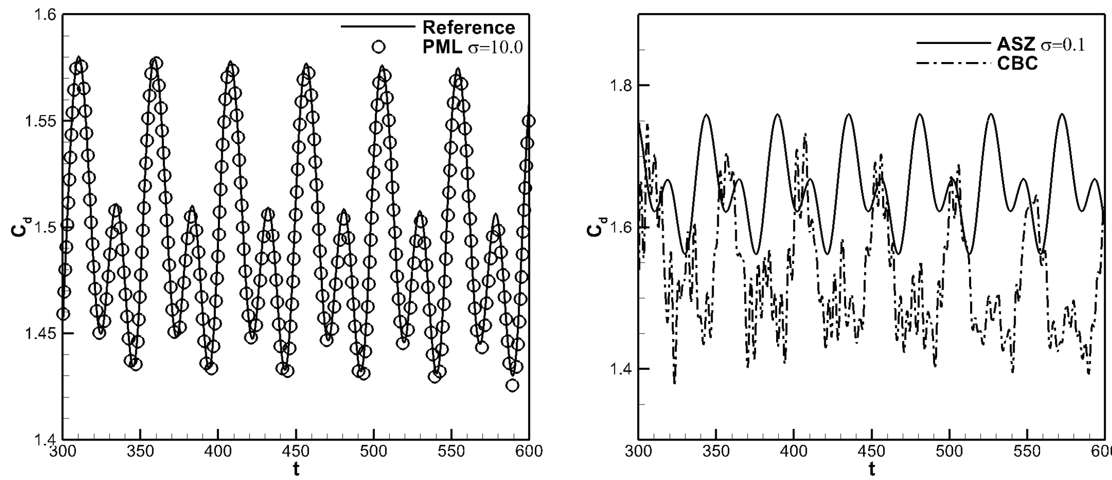

(a) (b)

Fig. 13. Time history of drag coefficients, (a) PML and the reference; (b) ASZ and CBC

Table 1. Comparison of mean drag coefficients for flow over two cylinders at $Re = 200$ and $s = 3D$

	CBC	ASZ	PML	Liang et al	Ding et al
$\boldsymbol{C_d}$	1.530	1.650	1.492	1.496	1.548

6. Conclusions

Two popular absorbing boundary conditions, the absorbing sponge zone and perfectly matched layer, are implemented with the spectral difference method on hexahedral meshes for non-linear Euler and Navier-Stokes equations in this paper. The disturbances are gradually attenuated thus the reflection at the end of the absorbing domain is minimized by using the spectral difference method with both zonal techniques. Both the ASZ and PML perform very effectively in the vortex and acoustic propagation problems. The reflected errors with the two zonal techniques are much smaller than those with the CBC based on linearized one-dimensional Euler equations. The absorbing processes with the two techniques are different owing to the different design concepts. The formula of the ASZ is much simpler than the PML technique and therefore easier to implement. However, it is still somewhat reflective and generates visible reflections at the interface with the ASZ between the physical domain and the absorbing domain. PML is more efficient in absorbing the disturbances. With the PML technique, the magnitude of the disturbances decreases exponentially in the absorbing domain and the solution finally reduces to the proposed mean solution at the end of the absorbing domain while the reflection generated at the interface between the physical domain and absorbing domain is almost invisible. In the case of low-Mach number laminar flow past two side-by-side cylinders, with complex geometries inside the physical domain the PML technique also performs well in absorbing the shedding vortices and accurately predicts the drag and lift forces on the wall with a relatively small computational domain.

Acknowledge

The authors would like to acknowledge the support for this work from the Department of Aerospace Engineering, Iowa State University, and partial support by the Air Force Office of Scientific Research.

Reference

[1] R. Abgrall and P.L. Roe, High order fluctuation schemes on triangular meshes, J. Sci. Compute., 19 (2003), 3-36.

[2] S. Abarbanel and D. Gottlieb, A mathematical analysis of the PML method, Journal of Computational Physics, 154, 266,283, 1997

[3] S. Abarbanel, D. Stanescu and M. Y. Hussaini, Unsplit variable perfectly matched layers for the shallow water equation with coriolis forces, Computational Geosciences, Vol. 7 (4), 265-294, 2003.

[4] B. Bacache, S. Fauqueus and P. Joly, Stability of perfectly matched layers, group velocities and anisotropic waves, Journal of Computational Physics, 188, 399-433, 2003.

[5] E. Bacache, A.-S. Bonnet-Ben Dhia and G. Legendre, Perfectly matched layers for the convected Helmholtz equations, SIAM J. Num. Anal., Vol. 42 (1), 409-433, 2004.

[6] T.J. Barth and P.O. Frederickso, High-order solution of the Euler equations on unstructured grids using quadratic reconstruction, AIAA Paper 96-0027, 1996.

[7] F. Bassi and S. Rebay, High-order accurate discontinuous finite element solution of the 2D euler equations, J. Comput. Phys., 138 (1997), 251-285.

[8] Bayliss, E. Turkel, Radiation boundary conditions for wave-like equations, Comm. Pure. Appl. Math, 33(1980), pp. 707-725.

[9] Bayliss, M. Gunzburger, E. Turkel, Boundary conditions for the numerical solution of elliptic equations in exterior regions, SIAM J. Appl. Math., 42(1982), pp. 430-451.

[10] J.-P. Berenger, A perfectly matched layer for the absorption of electromagnetic wave, Journal of Computational Physics, 144,185-200, 1994

[11] D.J. Bodony, analysis of sponge zones for computational aeroacoustics, Journal of Computational Physics, Vol. 212, 2006, 681-702

[12] Cockburn and C.W. Shu, TVB Runge-Kutta local projection discontinuous Galerkin finite element method for conservation laws II: General framework, Math. Comput., 52 (1989), 411-435.

[13] Cockburn and C.W. Shu, The Runge-Kutta discontinuous Galerkin method for conservation laws V: multidimentional systems, J. Comput. Phys., 141 (1998), 199-224.

[14] F. Collino and P. Monk, The perfectly matched layer in curvilinear coordinates, SIAM J. Sci, Comp, Vol. 19, No. 6, P. 2016, 1998.

[15] T. Colonius, S.K. Lele, and P. Moin, Boundary Condition for Direct Computation of Aerodynamic Sound Generation, AIAA Journal, Vol. 31, No. 9, 1993, pp.1574-1582

[16] T. Colonius, Modelling Artificial Boundary Conditions for Compressible Flow, Annual Review of Fluid Mechanics, Vol. 36, 2004,pp. 315-345.

[17] H. Ding, C. Shu, K.S. Yeo and D. Xu, Numerical simulation of flows around two circular cylinders by mesh-free least square-based finite difference methods. Int J. Numer Meth Fluids 2007; 53: 305–32.

[18] B. Engquist and A. Majda, Absorbing Boundary Conditions for the Numerical Evaluation of Waves, Math. of Comp., Volume 31, No. 139 (1977) pp. 629-651.

[19] J. B. Freund, Proposed inflow/outflow boundary condition for direct computation of aerodynamic sound, AIAA J., 35(4), 740-742(1997).

[20] S. D. Gedney, An anisotropic perfectly matched layer-absorbing medium for the truncation of FDTD lattices, IEEE Trans. Antennas Propagation, Vol. 44, P. 1630, 1996.

[21] M. B. Giles, Non-reflecting boundary conditions for Euler equation calculations, AIAA J., 28, 2050-2058(1990).

[22] J.S. Hesthaven, On the analysis and construction of perfectly matched layers for the linearized Euler equations, Journal of Computational Physics, 142, 129-147, 1998.

[23] T. Hagstrom and I. Nazarov, Absorbing layers and radiation boundary conditions for jet flow simulations, AIAA paper 2002-2606, 2002.

[24] T. Hagstrom and I. Nazarov, Perfectly matched layers and radiation boundary condtions for shear flow calculations, AIAA paper 2003-3298, 2003.

[25] R.L. Higdon, Absorbing Boundary Conditions for Difference Approximations to the Muti-Dimensional Wave Equation, Math of Comp, Volume 47, No.176 (1986) pp. 437-459.

[26] Hirsch, Numerical Computation Of Internal And External Flows: Fundamentals Of Computational Fluid Dynamics, (2007)

[27] C. Hu and C.W. Shu, Weighted essentially non-oscillatory schemes on triangular meshes, J. Comput. Phys., 150 (1999), 97-127.

[28] F.Q. Hu, On absorbing boundary conditions for linearized Euler equations by a perfectly matched layer, Journal of Computational Physics, Vol. 129, 201-219, 1996

[29] F.Q. Hu, On Perfectly Matched Layer as an absorbing boundary condition, AIAA paper 96-1664, 1996

[30] F.Q. Hu and J. L. Manthey, Application of PML absorbing boundary conditions to the Benchmark Problems of Computational Aeroacoustics, NASA CP 3352, 119-151, Second Computational Aeroacoustics (CAA) Workshop on Benchmark Problems, 1997

[31] F.Q. Hu, A stable, Perfectly Matched Layer for linearized Euler equations in unsplit physical variables, Journal of Computational Physics, Vol. 173, 455-480, 2001

[32] F.Q. Hu, On Constructing stable Perfectly Matched Layers as an absorbing boundary condition for Euler equations, AIAA paper 2002-0227, 2002

[33] F.Q. Hu, Solution of aeroacoustic benchmark problems by discontinuous Galerkin method and Perfectly Matched Layer for nonuniform mean flows , To appear in the Proceedings of the 4th CAA Workshop on Benchmark Problems, 2003

[34] F.Q. Hu, Absorbing boundary conditions (a review), International Journal of Computational Fluid Dynamics, Vol. 18, No. 6, 513-522, 2004

[35] F.Q. Hu, On using Perfectly Matched Layer for the Euler equations with a non-uniform mean flow , AIAA-paper 2004-2966, 2004

[36] F.Q. Hu, A Perfectly Matched Layer Absorbing Boundary Condition for Linearized Euler Equations With a Non-uniform Mean Flow , Journal of Computational Physics, Vol. 208, 469-492, 2005

[37] F.Q. Hu, On the construction of PML absorbing boundary condition for the non-linear Euler equations , AIAA paper 2006-0798, 2006

[38] F.Q. Hu, X.D. Li and D. K. Lin, PML absorbing boundary condition for non-linear aeroacoustics problems , AIAA paper 2006-2521, 2006

[39] F.Q. Hu, X.D. Li and D.K. Lin, Absorbing boundary conditions for nonlinear Euler and Navier-Stokes equations based on the Perfectly Matched Layer technique, Journal of Computational Physics,227-9(2008), 4398-4424.

[40] P.G. Huang, Z.J. Wang and Y. Liu, An implicit space-time spectral difference method for discontinuity capturing using adaptive polynomials, AIAA Paper 2005-5255, 2005.

[41] H.T. Huynh, A flux reconstruction approach to high-order schemes including discontinuous Galerkin methods, AIAA Paper 2007-4079.

[42] Jameson, A Proof of the stability of the spectral difference method for all orders of accuracy, ACL Report no. 2009-1, Stanford University, March, 2009.

[43] D.A. Kopriva, and J.H. Kolias, A conservative staggered-grid Chebyshev multidimain method for compressible flows, J. Comput. Phys., 125(1996), 244-261.

[44] D.A. Kopriva, A staggered-grid multidimain spectral method for compressible Navier-Stokes equations, J. Comput. Phys., 143(1998), 125-158.

[45] Lerat, J. Sides and V. Daru, Efficient computation of steady and unsteady transonic flows by an implicit solver, In W. G. Habashi, (ed.), Advances in Computtional Transonics, Pineridge, Press, 1984

[46] C.L. Liang , S. Premasuthan and A. Jameson, High-order accurate simulation of low-Mach laminar flow past two side-by-side cylinders using spectral difference method, Computers and Structures 87 (2009) 812–827

[47] Y. Liu, M. Vinokur and Z.J. Wang, discontinuous spectral difference method for conservation laws on unstructured grids, in: C. Groth, D.W. Zingg (Eds.), Proceeding of the 3rd international Conference in CFD, Toronto, Springer, 2004, pp. 449-454.

[48] Y. Liu, M. Vinokur and Z.J. Wang, Spectral (finite) difference method for conservation laws on unstructured grids I: Basic formulation, J. Compute. Phys.. 216 (2006), 780-801.

[49] Y, Liu, M. Vinokur and Z.J. Wang, Spectral (finite) volume method for conservation laws on unstructured grids V: Extension to three-dimensional systems, J. Comput. Phys., 212 (2006), 454-472.

[50] G. May and A. Jameson, A spectral difference method for the Euler and Navier-Stokes equations on unstructured grids, AIAA Paper 2006-304, 2006.

[51] A.T. Patera, A spectral element method for fluid dunamics: Laminar flow in a channel expansion, J. Comput. Phys., 54 (1984), 468-488

[52] S.A. Parrish and F. Q. Hu, Application of PML Absorbing Boundary Condition to Aeroacoustics Problems with An Oblique Mean Flow , AIAA paper 2007-3509, 2007

[53] P.G. Petropoulos, Reflectionless sponge layers as absorbing boundary conditions for the numerical solution of Maxwell's equations in rectangular, cylindrical and spherical coordinates, SIAM J. App. Math., Vol. 60, 1037-1058, 2000.

[54] T. Poinsot, and S.K. Lele, Boundary conditions for direct simulation of compressible viscous flows, J. Comput. Phys., 101, 104-129(1992)

[55] P. L. Roe, Approximate Riemann solvers, parameter vectors, and difference schemes, J. Comput. Phys. 43 (1981) 357-372.

[56] Y. Sun, Z.J. Wang and Y. Liu, Spectral (finite) volume method for conservation laws on unstructured grids VI: Extension to viscous flow, J. Comput. Phys., 215 (2006), 41-58.

[57] Y. Sun, Z.J. Wang, Y. Liu, High-Order Multidomain Spectral Difference Method for the Navier-Stokes Equations on Unstructured Hexahedral Grids, Communications in Computational Physics, Vol. 2, No. 2(2007) 310-333.

[58] Y. Sun, Z.J. Wang, Y. Liu and C.L. Chen, Efficient implicit LU-SGS algorithm for high-order spectral difference method on unstructured hexahedral grids, AIAA paper, (2007), 2007-0313

[59] S. Ta'asan, and D. M. Nark, An absorbing buffer zone technique for acoustic wave propagation, AIAA J. 95-0164 (1995).

[60] C.K.W. Tam, L. Auriault and F. Cambulli, Perfectly Matched Layer as an absorbing boundary condition for the linearized Euler equations in open and ducted domains, Journal of Computational Physics, 144,213-234, 1998.

[61] K.W. Thompson, Time-dependent boundary conditions for hyperbolic systems, J. Comput. Phys., 68, 1-24(1987).

[62] Turkel and A. Yefet, Absorbing PML boundary layers for wave-like equations, Applied Numerical Mathematics, Vol. 27, 533-557, 1998.

[63] K. Van den Abeele, C. Lacor and Z.J. Wang, "On the stability and accuracy of the spectral difference method," Journal of Scientific Computing, Journal of Scientific Computing 37, (2008) 162–188.

[64] Z.J. Wang, Spectral (finite) volume method for conservation laws on unstructured grids: Basic formulation, J. Comput. Phys., 178 (2002), 210-251.

[65] Z.J. Wang and Y. Liu, Spectral (finite) volume method for conservation laws on unstructured grids III: Extension to one-dimentional systems, J. Sci. Comput. 20 (2004), 137-157.

[66] Z.J. Wang, L. Zhang and Y. Liu, Spectral (finite) volume method for conservation laws on unstructured grids III: Extension to two-dimentional systems, J. Sci. Comput. 194 (2004), 716-741.

[67] Z.J. Wang and Y. Liu, The spectral difference method for the 2D Euler equations on unstructured grids, AIAA Paper 2005-5112, 2005.

[68] Z.J. Wang, Y. Liu, G. May and A. Jameson, Spectral difference method for unstructured grids II: Extension to the Euler equations, J. Sci. Comput., 32(1) (2007), 45-71.

[69] H.C. Yee, R.M. Beam and R.F. Warming, Boundary approximation for implicit schemes for one-dimensional inviscid equation of gas dynamics, AIAA Journal, 20, 1203-11, 1982.

[70] L. Zhao and A.C. Cangellaris, GT-PML: Generalized theory of Perfectly Matched Layers and its application to the reflectionless truncation of finite-difference time-domain grids, IEEE Trans. Microwave Theory Tech., Vol. 44, 2555-2563, 1996.

[71] Y. Zhou and Z.J. Wang, “Simulation of CAA Benchmark Problems Using High-Order Spectral Difference Method and Perfectly Matched Layers, AIAA-2010-838.

CHAPTER 3. A Low-Frequency Instability/Oscillation near the Airfoil Leading-Edge at Low Reynolds Numbers and Moderate Incidences

A paper submitted to AIAA Journal

Ying Zhou and Z.J. Wang

Abstract

Numerical simulations of the low-Reynolds number ($\mathrm{Re} = 10^4 \sim 10^5$) flows over a SD7003 airfoil at moderate incidences ($< 10°$) are performed in the current paper. A low-frequency convective instability is observed to dominate the spectrum near the leading edge and be responsible for the growth of the disturbance in the attached boundary layer. The characteristic frequency, the growth rate and the wave shape are investigated based on the numerical results. The growth of the low-frequency instability is not in agreement with parallel flow stability theory, nor with leading edge receptivity theory. And it has a higher growth rate than the Tollmien-Schlichting (T-S) wave. The effects of the angle-of-attack (AoA), the Reynolds number and the airfoil geometry on the low-frequency instability are investigated and discussed.

Nomenclature

AoA = angle of attack

α_r = wave number of the disturbances in x direction in linear stability theory

α_i = growth rate of the disturbances in linear stability theory

β = wave number of the disturbances in z direction in linear stability theory

c = chord length

F, G, H = vector of fluxes

i, j, k = index of coordinates in x, y, z direction

J = Jacobian matrix

M = Mach number

p = nondimensional pressure

$Q, \widetilde{Q}$ = vector of conservative variables in Cartesian coordiantes and standard unstructured elements

$\mathrm{Re_c}$	=	Reynolds number based on chord length
ρ	=	nondimensional density
s	=	wave speed of the disturbance in linear stability theory, $s = \omega/\alpha_r$
St	=	Strouhal number, $\mathrm{St} = \mathrm{fC}\sin\mathrm{AoA}/\mathrm{U}$ in airfoil literature
t	=	nondimensional time $t = t^*/(c/U_\infty)$
t^*	=	dimensional time
u, v, w	=	nondimensional velocity in x, y, z direction
U_∞	=	freestream velocity
u', v', w'	=	nondimensional velocity fluctuation in x, y, z direction
u_t, u_t'	=	nondimensional tangential velocity / fluctuation, normal to the wall surface
x, y, z	=	nondimensional Cartesian coordinates
ξ, η, ς	=	nondimensional coordinates in standard cubic
ω	=	frequency of the disturbances
Δx^+, $\Delta y^+, \Delta z^+$	=	cell size in wall units
Ω	=	computational spatial domain

1. Introduction

In the past decade, low-Reynolds-number flows and the associated laminar separation bubbles (LSBs) have been of great interest in the development of micro air vehicles (MAV), small scale wind turbines and low-pressure turbine/cascade. Since laminar boundary layers are less resistible to the significant adverse pressure gradient, LSBs are widely found over the suction side of low-Reynolds number airfoils/turbines at incidences. LSBs on an airfoil are classified into two types: a short bubble and a long bubble [1]. A short bubble is formed when the airfoil AoA is relatively small. The flow quickly transitions into a turbulent one and reattaches downstream after the breakdown of LSBs. A long bubble is formed at higher AoAs near the stall condition. For airfoils, the behavior of the LSB affects the aerodynamic performance and typically causes the increase of the pressure drag. Meanwhile, the existence of a turbulent boundary layer induces higher friction force on the airfoil than a laminar flow, and therefore can cause the degradation of the lift-to-drag ratio. Early works on LSB and associated hydrodynamic instability mechanisms can be traced back to the

1950s [1] and 1960s [2-5]. With the rapid development of numerical methods, numerical simulations of laminar-separated flows have been used to investigate the LSB and the associated turbulent transition. The two-dimensional simulations of separation bubbles were first carried out and investigated by Pauley et al. [6]. Pauley [7] and Rist [8] carried out three-dimensional studies of the primary instability later, but the transition was still not resolved due to the limitation of the computational resource and computer technology. More recently, direct numerical simulations (DNS) to fully resolve the transition of LSBs to turbulence were conducted by Alam & Sandham [9] and also Spalart & Strelets [10]. With the development of experimental techniques, Laser-Doppler-Anemometry (LDA) and Particle-Image-Velocity (PIV) technologies can provide the flow field measurements to quantify the evolution of the unsteady flow structure and investigate the dynamics of LSBs (see Marxen et al. [11]; Lang et al. [12]; Hu & Yang [13]; Yarusevych et al. [14]; Hain et al. [15]). In spite of considerable progresses in recent years, both the LSB and the transition mechanism still need further investigation. Distinct from the convective types of transition, the simultaneous presence of and the interaction between separation and transition make the problem highly complicated.

In the present study, the numerical simulations of the low-Reynolds number flows over a SD7003 airfoil at incidences are carried out. A high-order spectral difference (SD) method for the three-dimensional Navier-Stokes equations on hexahedral grids developed by Sun et al. [16] is used. The simulations started with a uniform freestream initial condition and no incoming disturbances are added explicitly. The 'short' bubbles and transitional flows are observed on the suctions side of the airfoil under the present conditions. In previous studies of the unforced flow over airfoils, the LSBs and the self-sustained transition process were found owing to the global instability of the acoustic-feedback loops (see Deng et al. [17]; Zhou & Wang [18]; Jones et al. [19]). In the acoustic-feedback loop, the acoustic disturbances generated in the wake of the trailing edge act as the initial disturbances and the transition is triggered by the receptivity of the boundary layer to acoustic waves (Deng et al. [17]). Jones et al. [19] found that the amplitude of the trailing-edge noise is sufficient to promote transition via the receptivity process in the vicinity of the leading edge and the feedback loop plays an important role in frequency selection of the vortex shedding that occurs in two dimensions.

The growth of the primary instability takes over a much longer distance comparing with the subsequent breakdown to turbulence. During the primary instability stage, the disturbances are amplified inside the attached boundary layer before separation and then inside the detached shear layer. After separation, an inflection point appears in the streamwise velocity profile. And the inviscid/Kelvin-Helmholtz (K-H) instability plays the dominant role in the growth of the disturbances. The inviscid flow has been found to be more unstable in a two-dimensional mode than in a three-dimensional mode according to the Rayleigh stability problem as shown in Drazin [20]. The two-dimensional disturbances grow exponentially inside the detached shear layer and the shedding of the two-dimensional vortices or 'rolling' is usually observed afterwards and the vortices grow in size after shedding. Yarusevych et al. [21] investigated the behavior of the shedding vortices at different Reynolds numbers and angles of attack. It was found that the fundamental frequency of the roll-up vortices developing in the separated shear layer scales with the Reynolds number and the precise correlations depend on the angle of attack. In Hain et al. [15], a band of vortex shedding frequencies was found instead of a single frequency. Although the K-H instability is well accepted to be dominant after separation, the precursor of the K-H instability, which is responsible for the disturbance growth inside the attached boundary layer, is not clear yet. The well-known T-S instability is usually regarded as the dominant instability inside the attached boundary layer. Marxen et al. [11] and Hein et al. [15] conclude that transition was driven by convective amplification of a two-dimensional T-S wave. However, in Spalart & Strelets [10], the T-S wave was discarded as the causes of the transition but a low frequency and long wavelength 'wavering' shear layer (or 'flapping') before separation was proposed because 'the u' profiles do not have the double-peak pattern of T-S waves'. Yang & Voke [22] found in their study that the initial two-dimensional instability waves grow downstream with an amplification rate usually larger than that of T-S waves. Watmuff [23] suggested that that the shear layer is viscously stable with respect to small-magnitude T-S disturbances while it remains attached.

The current study focuses on the primary growth of disturbances on a low-Reynolds number airfoil at moderate incidences when ‘short’ bubbles occur, and a low-frequency instability is found to be dominant near the leading edge and responsible for the growth of disturbances. The growth of the low-frequency instability is not in agreement with the parallel flow stability theory, nor with the leading edge receptivity theory. The AoA, Reynolds number and the geometry of the airfoil are varied to investigate their effects on the frequency and the growth rate of the low-frequency instability. The paper is organized as follows. In § 2, a high-order method for unstructured hexahedral meshes used for the numerical simulation and a numerical method for the linear stability theory (LST) are introduced. After that, the computational details are given. In § 3, a low-frequency instability observed in the attached boundary layer near the leading edge is discussed. The effects of the AoA, the Reynolds number and the geometry of the airfoil on the low-frequency instability are studied. The computation results and associated details will be discussed in § 4, followed by the conclusions in § 5.

2. Numerical Methods

2.1 Review of Multidomain Spectral Difference (SD) Method

We consider the unsteady three-dimensional compressible nonlinear Navier-Stokes equations written in the conservative form as

$$\frac{\partial Q}{\partial t}+\frac{\partial F}{\partial x}+\frac{\partial G}{\partial y}+\frac{\partial H}{\partial z}=0 \tag{1}$$

on domain $\Omega \times [0, T]$ and $\Omega \subset R^3$ with the initial condition

$$Q(x, y, z, 0) = Q_0(x, y, z) \tag{2}$$

and appropriate boundary conditions on $\partial\Omega$.

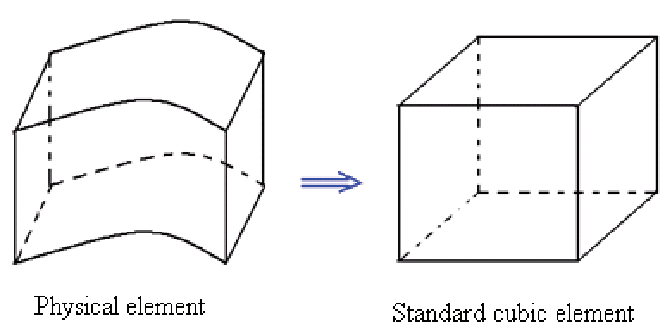

Figure 1. Transformation from a physical element to a standard element

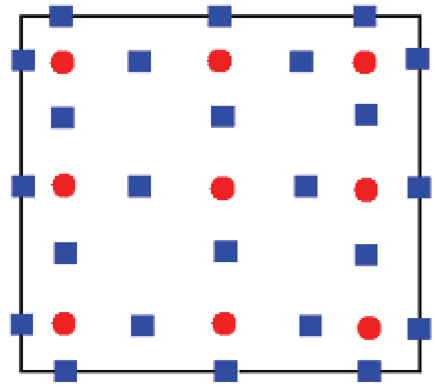

Figure 2. Distribution of solution points (circles) and flux points (squares) in a standard element for a 3rd-order SD scheme.

In SD method, it is assumed that the computational domain is divided into non-overlapping unstructured hexahedral cells or elements. In order to handle curved boundaries, both linear and quadratic isoparametric elements are employed, with linear elements used in the interior domain and quadratic elements used near high-order curved boundaries. In order to achieve an efficient implementation, all physical elements (x, y, z) are transformed into standard cubic element $(\xi, \eta, \varsigma) \in [-1,1] \times [-1,1] \times [-1,1]$ as shown in Fig. 1.

In the standard element, two sets of points are defined (Fig. 2), namely the solution points and the flux points. The solution unknowns or degrees-of-freedom (DOFs) are the conserved variables at the solution points, while fluxes are computed at the flux points in order to update the solution unknowns. At the interfaces between each two elements, a Riemann solver such as Roe flux [24] is used to compute the common inviscid flux, and the viscous flux at the interface is computed following the algorithm given in [25]. A detailed description of the space discretization and the algorithm in SD method to compute the inviscid flux and viscous flux derivatives can be found in [16].

2.2 Review of the linear stability theory

In this paper, the linear stability theory (LST) is used to analyze the stability characteristics of the attached boundary layer and detached shear layer. The linear stability analysis of the velocity profiles are presented based on the time- and span-averaged flow field. Here, the flow is assumed compressible. The compressible LST used in this paper follows the procedure of Malik [26]. Under the assumptions of parallel flow and small disturbances, and neglecting high order terms, the linearized governing equations can be derived from the non-linear N-S equations (1). By assuming the disturbances of the following travelling waves

$$\phi_i' = \widehat{\phi}_i e^{i(\alpha x+\beta z-\omega t)}, \tag{3}$$

where α and β are the complex wavenumber in the x and z directions respectively, and ω is the complex frequency of the travelling wave. Substituting (3) into the linearized governing equation, we obtain the following system of ordinary differential equations

$$\left(A\frac{d^2}{dy^2} + B\frac{d}{dy} + C\right)\widehat{\phi} = 0, \tag{4}$$

where $\widehat{\phi} = \{\hat{u}, \hat{v}, \hat{p}, \widehat{T}, \widehat{w}\}$ and matrices A, B and C can be found in Malik [26]. The boundary conditions for equation (4) are

$$y = 0;\ \hat{u} = \hat{v} = \widehat{w} = 0;\ \frac{d\widehat{T}}{dy} = 0 \text{ (adiabatic wall)}$$

$$y = \infty;\ \hat{u}, \hat{v}, \widehat{T}, \widehat{w} \to 0.0$$

Equation (4) constitutes an eigenvalue problem, which can be solved to find the complex dispersion relation $\omega = \omega(\alpha, \beta)$ for the temporal mode, or $\alpha = \alpha(\omega, \beta)$ for the spatial mode:

1) $\bar{A}\phi = \omega\bar{B}\phi$ for temporal stability
2) $\bar{A}\phi = \alpha\bar{B}\phi$ for spatial stability

where ω or α is the eigenvalue and ϕ is the discrete representation of the eigenvector. For spatial stability, the eigenvalue is determined by the determinant condition

$$\mathrm{Det}|\bar{A} - \alpha\bar{B}| = 0 \tag{5}$$

Equation (5) represents the dispersion relation of $\alpha = \alpha(\omega, \beta)$, and in this paper we employ the single domain spectral (SDSP) collocation method to discretize equation (5). The eigenvalue problem of the discretized equation can be solved with Linear Algebra PACKage (LAPACK) or Matlab software. The current code was verified through comparison with the LST results of viscous supersonic plane Couette flow in Hu & Zhong [27].

2.3 Details of numerical simulations

The numerical simulations are carried out at a Reynolds number based on the airfoil chord of $\mathrm{Re_c} = 6 \times 10^4$ and Mach number $\mathrm{M} = 0.2$. The AoA of the baseline case is $\mathrm{AoA} = 4°$. All the variables in this paper are non-dimensional unless noted. Figure 3 shows the computational mesh for the current simulation. The mesh is refined near the wall and around the physically important region where the separation bubble and vortex breakdown occur. The smallest cell is located at the trailing edge with dimension (in wall units) $\Delta y^+ = 2.5$ in the direction normal to the wall, $\Delta x^+ = 25.0$ along the chord and $\Delta z^+ = 12.0$ in the spanwise direction. Noting that inside the cell each direction is discretized by the solution/flux points (Fig. 2), the effective grid size near the wall for 3rd and 4th-order SD method is close to the requirement of a direct numerical simulation (DNS). The total number of cells is 253,600, resulting in 6,847,200 and 16,230,400 degree-of-freedom (per equation) for the 3rd and 4th-order SD schemes respectively. The grid resolution has been verified in previously published papers28 and good agreements of the mean and statistical results were found in a p-type grid refinement study.

In order to simulate an infinite wing, a periodic boundary condition is used in the spanwise direction. The span width of the wing is set to be 20% of the chord, which has been proved to be adequate long enough in [28]. A non-slip, adiabatic boundary condition is applied on the surface of the wing. Near the far-field of the computational domain, the absorbing sponge zone (ASZ) [29] is used to absorb the out-going disturbances.

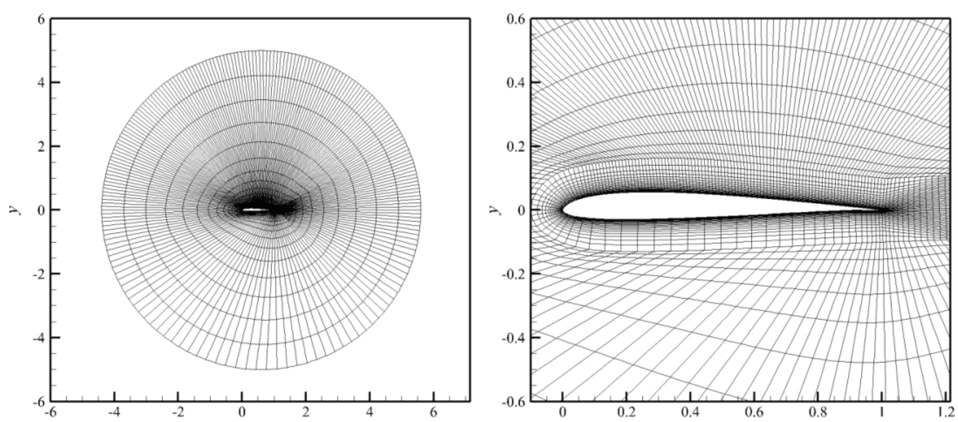

Figure 3. Computational mesh.

3. The growth of a low-frequency disturbance

The current cases are in the regime of low-speed and low-Reynolds number flow, in which laminar separation and turbulent transition occur over the suction side of the wing with incidences. The amplitude of the disturbances needs to reach a certain level before the turbulent breakdown could happen, and the growth of the disturbances in the laminar flow is due to the so-called primary instability. Comparing with the abrupt breakdown stage, the primary instability growth region is much longer and dominates the entire transition process. Figure 4 shows the iso-surfaces and contour lines of the Q-criteria [30]. The primary growth stage ($x = 0.0{\sim}0.55$) appears mainly two-dimensional. Vortex shedding is observed on the suction side after separation. And vortex breakdown occurs at the end of the LSB.

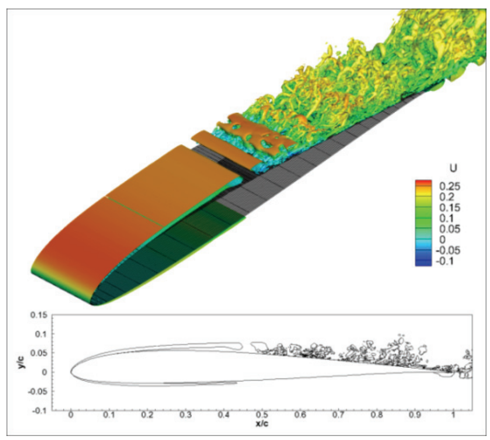

Figure 4. Iso-surface and contour line of Q-criteria at $\mathbf{Q = 1}$.

In order to find the major physical mechanisms of instabilities in the flow field, a series of probes are placed inside the shear layer of the flow filed to record the histories of flow variables as shown in Fig. 5. The spectra of velocity, derived through Fourier transformation based on the recorded flow variable histories for 20 non-dimensional time, are shown in Fig. 6. Probes 1-3 (Fig. 5) are placed inside the attached boundary layer in order to detect the instability of the boundary layer. The velocity spectrum at probe 2 is shown in Fig. 6.a, and a low-frequency mode (ω_1) dominates the spectrum. The spectra at probes 1 and 3 are similar. Probes 4-6 (Fig. 5) are placed inside the detached shear layer to detect the instability of the shear layer. The velocity spectrum at point 6 is shown in Fig. 6.b, and a high-frequency mode (ω_2) corresponding to the vortex shedding frequency takes the dominant role in the velocity spectrum. The spectra at probes 4 and 5 are similar. In the current case, the frequencies of ω_1 and ω_2 are found to be 1.81 and 36.09 respectively. It should be noted that beside the dominances of ω_1 and ω_2 components in the spectra, the overall disturbances also contain the acoustic signals generated near the trailing edge and dominated by ω_3 (Fig. 6). The receptivity of the boundary layer to the acoustic signals and the triggering of the initial disturbances exceed the scope of the current paper, and thus are not discussed here. The readers interested in this aspect can refer to Deng et al. [17] and Jones et al. [19].

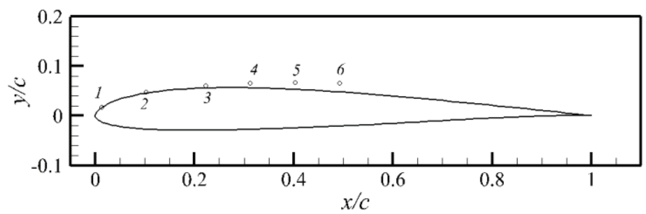

Figure 5. Probes in the flow filed.

Figure 7.a&b show the overall time histories of the velocity disturbances and the ω_1 component derived through the inverse Fourier transformation at probe 2 and 3 (Fig. 5). The dominance of ω_1 component and the growth of its amplitude can be clearly seen in Fig. 7.a&b from probe 2 to 3. Fig. 7.c&d show the time histories of the velocity disturbances and the ω_1 component at probe 5 and 6. Beside the ω_1 component, a high-frequency component corresponding to ω_2 appears in the overall histories of the velocity. The growth of the high-frequency ω_2 component can be seen in Fig. 7.c&d in comparison of the overall disturbances and the ω_1 component. Although the ω_1 mode is still quite important in the spectrum of Fig. 6.b, it is observed that the ω_2 component is more dominant at probe 6 (Fig. 7.d).

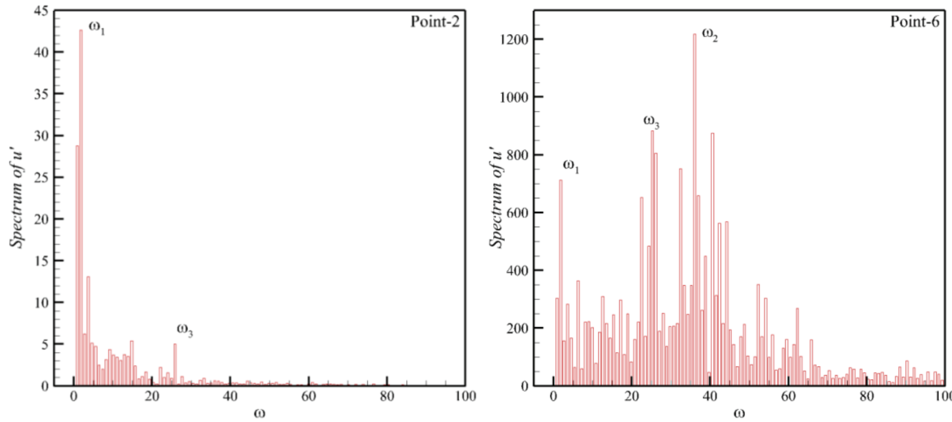

a) b)

Figure 6. Spectra of velocity at the probes a) Point-2 and b) Point-6 shown in Fig. 5.

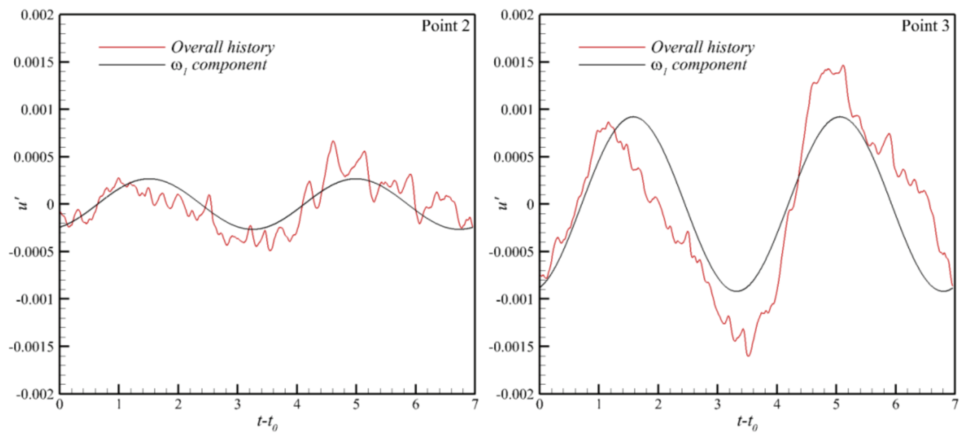

a) b)

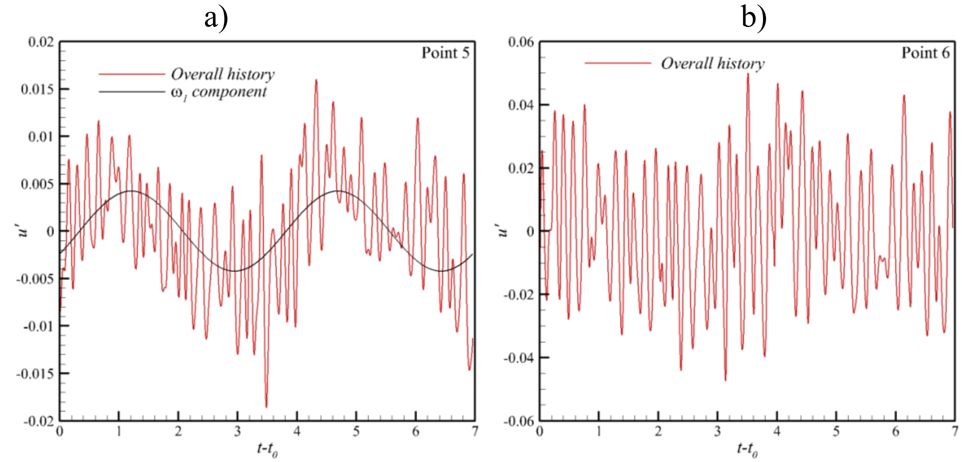

c) d)

Figure 7. Time histories of the velocity disturbances and the $\boldsymbol{\omega_1}$ component derived through the inverse Fourier transformation at probe points (Fig. 5): a) Point-2; b) Point-3; c) Point-5; d) Point-6.

Both the ω_1 and ω_2 components are convectively unstable as shown in Fig. 7. And it seems that the ω_1 component leads the growth of the overall disturbances in the attached boundary layer, while the ω_2 component dominates in the detached shear layer. Figure 8.a shows the normalized profiles of the mean tangential velocity at different locations and Fig. 8.b shows the corresponding normalized profiles of RMS tangential velocity disturbances at the corresponding locations. The mean flow separates at $\mathrm{x} = 0.225$ and the development of the mean shear layer and the detachment can be seen in Fig. 8.a. The profiles of the RMS of tangential velocity disturbance u_t' change the shapes along the mean shear layer as shown in Fig. 8.b. It appears that due to the dominances of the ω_1 and ω_2 components at different locations, the shape of the disturbance profile has two difference patterns in the attached boundary layer and the detached shear layer. In the following, the two types of the profile are further investigated. In order the detect the characters of the instabilities, the LST is applied based on the mean flow field and the LST results are used for comparison with the numerical results.

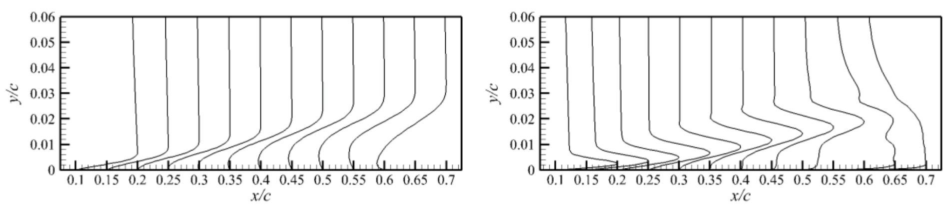

a) b)

Figure 8. Numerical results for Case-4: a) normalized profiles of the mean tangential velocity at different locations; b) normalized profiles of the RMS tangential velocity disturbances at different locations.

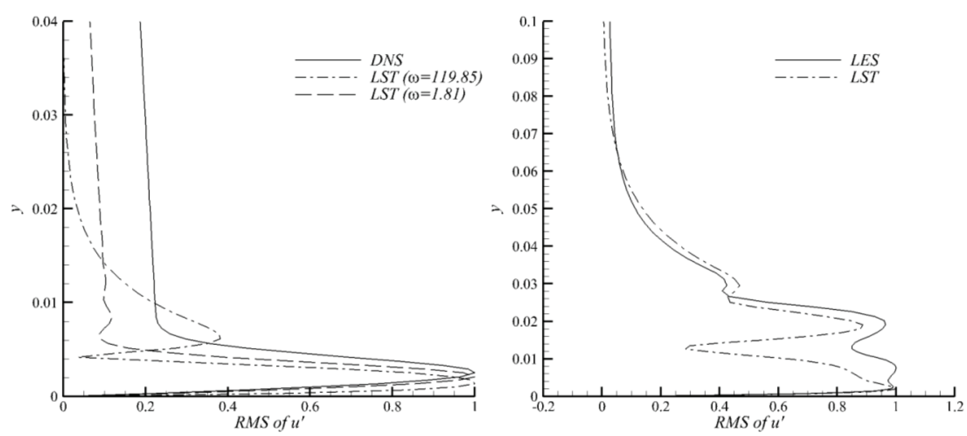

a) b)

Figure 9. Comparison of the RMS of the tangent velocity disturbances $\mathbf{u}_t'$ and the LST results at a) $\mathbf{x = 0.1}$ and b) $\mathbf{x = 0.55}$.

Inside the attached boundary layer, a T-S wave is usually thought to be the dominant instability which causes the growth of the disturbances. However, in the present cases, the T-S wave does not appear to play a role here. Based on the mean profile at $x = 0.1$, the most unstable T-S wave predicted by the LST appears at a frequency $\omega_{T-S} = 119.85$, which is much higher than the dominant frequency $\omega_1 = 1.81$. The profile of the RMS of u_t' in the current numerical simulation is presented in Fig. 9.a, and the profiles of the most unstable T-S wave at $\omega_{T-S} = 119.85$ and the T-S wave corresponding to $\omega_1 = 1.81$ are also shown for comparison. It is observed that the RMS of u_t' does not possess the two-peak feature of the normal T-S waves. Spalart and Strelets10 found a good agreement between the peak location of the RMS of u_t' profile and the peak location of du_t/dn (n being the wall normal direction) profile. Table 1 compares the wave speed and growth rate of the numerical and LST results. The wave speed and the growth rate of the numerical simulation are derived based on the numerical results, which can be seen in detail in the next section. It can be seen that at frequency $\omega_1 = 1.81$, the T-S wave is predicted to be stable. Meanwhile the growth rate of the low-frequency instability is much higher than that of the predicted most unstable T-S wave (also see Yang & Voke22).

After separation, an inflection point is observed in the mean velocity profiles shown in Fig. 8.a and the K-H instability becomes more dominant. Figure 9.b shows the profiles of the disturbances at $x = 0.55$. The LES curve denotes the profile of the overall disturbances, and the LST curve is the profile of the most unstable (has the highest growth rate) K-H mode. Although the curve of the numerical simulation contains all the modes, the LST curve predicts the peaks and valleys of the profile quite well, as at $x = 0.55$ the vortex shedding frequency dominates the spectrum. Table 2 compares the wave speed and growth rate of the present numerical simulation and LST results and the agreement is quite good for this stage. The most unstable wave found in the LST based on the mean profiles at $x = 0.55$ has been found to be $\omega_{K-H} = 39.85$, which is quite close to the frequency $\omega_2 = 36.09$ of the shedding vortices. Meanwhile, the growth rate of the most unstable wave ω_{unstable} predicted with LST is $\alpha_i = 29.10$ and is also in very good agreement with the growth rate of the shedding vortices $\alpha_i \approx 30.17$ as shown in Table 2.

The T-S wave component is not visible in the attached boundary layer near the leading edge. The K-H instability in the present cases is similar to but not a purely inviscid instability due to the viscous effects near the wall. From the LST, it is found that the K-H instability in the present cases belongs to the family of the T-S instability. In comparison with the LST results, the low-frequency instability seems not of the T-S wave type and appears to be an unusual mechanism to the authors, while the high-frequency instability agrees well with the LST results. For better understanding of the low-frequency instability, the AoA, Reynolds number and the airfoil geometry are varied to study the associated characters in the following sections.

Table 1. Comparison between LES and LST results at $\mathbf{x = 0.1}$

	ω	s	α_i
LES	1.81	≈0.53	≈16.69
LST	119.85	0.63	3.30
LST	1.81	0.18	stable

Table 2. Comparison between LES and LST results at $\mathbf{x = 0.55}$

	Frequency ω	s	α_i
LES	36.09	≈0.55	≈30.17
LST	39.85	0.56	29.10

3.1 Angle-of-attack effects

In this section, the numerical simulations are carried out at AoA = 2° and 6° for comparison with the baseline case and the AoA effects on the low-frequency instability are investigated based on the numerical results at all three AoAs. In the following text, each case is named after its AoA at which it has been carried out, i.e. Case-2 represents the case at AoA = 2° and so on so forth. In order to quantitatively study the growth of the disturbances, probes are placed at the locations of the velocity RMS peaks as shown in Fig. 10.a-c to record the histories of flow variables in the primary growth region of all three cases. The RMSs of u_t' recorded with the probes along the streamwise direction are shown in Fig. 10.d-f. Note that the shape of the growth curves is quite similar in all three cases. According to the rate of disturbance growth α, the overall growth of the disturbances can be divided into two major stages by a sign change of $d^2\alpha/dx^2$ and the region between the two stages is the transient region. $d\alpha/dx$, the changing of the growth rate measures the tendency of the instability and the sign change of $d^2\alpha/dx^2$ indicates the extremum of the tendency.

As discussed above that the two frequencies ω_1 and ω_2 are found to be dominant in the attached and detached shear layers respectively, it is natural to find that the two major growth stages are caused by the two types of instabilities respectively. The dash line in Fig. 10.e derived through the inverse Fourier transformation based on the recorded variable histories shows the contribution of disturbance growth from the ω_1 component for Case-4. Note that the overall growth of disturbances is dominated by the low frequency component (ω_1) for a long distance from $x = 0.0$ to $x = 0.5$. The dash-dot line in Fig. 10.e shows the contribution of the disturbance growth from the K-H instability (ω_2) for Case-4. After $x = 0.5$ the ω_1 component decays and the ω_2 component grows from a very small amplitude $\sim 10^{-4}$ after the separation point $x = 0.225$. It can be seen in Fig. 10.e that the K-H instability leads to the second major growth of the overall disturbances in Case-4, and similar processes can be observed in the other two cases (Fig. 10.d and Fig. 10.e). The growth trend of the overall disturbances in Case-4 agrees well with the spectra shown in Fig. 6 and the evolvement of the disturbance RMS profile shown in Fig. 7.b.

The average growth rates of the instabilities in the two stages are labeled in Fig.s 10.d-f for all three cases. The growth rate of the low-frequency ω_1 instability is high near the leading edge and gradually decreases in the streamwise direction. And the average growth rate of the low-frequency instability increases with the AoA. Table 3 lists the frequencies of ω_1 and ω_2 for all three cases, and the frequency ω_1 decreases with the AoA. The Strouhal number lies around $St \approx 0.02$ as shown in Table 3. It is interesting to find that the Strouhal number $St \approx 0.02$ is close to that of the low-frequency oscillation of the LSB on airfoils near stall condition in the literatures31-34. Near stall condition the 'long' LSBs were found to oscillate at a very low frequency, and the Strouhal numbers of the low-frequency are reported to be ranging from $St = 0.005 \sim 0.02$ in Ref. [31-34], which is much lower than that of the oscillating wake of a bluff body ($St \approx 0.2$). Here, it seems the low-frequency oscillation also exists in current 'short' bubbles.

Table 3. Characteristic frequencies and Strouhal number

Case	AoA	ω_1	St	ω_2
Case-2	2°	3.42	0.019	22.22
Case-4	4°	1.81	0.020	36.09
Case-6	6°	1.09	0.018	60.73

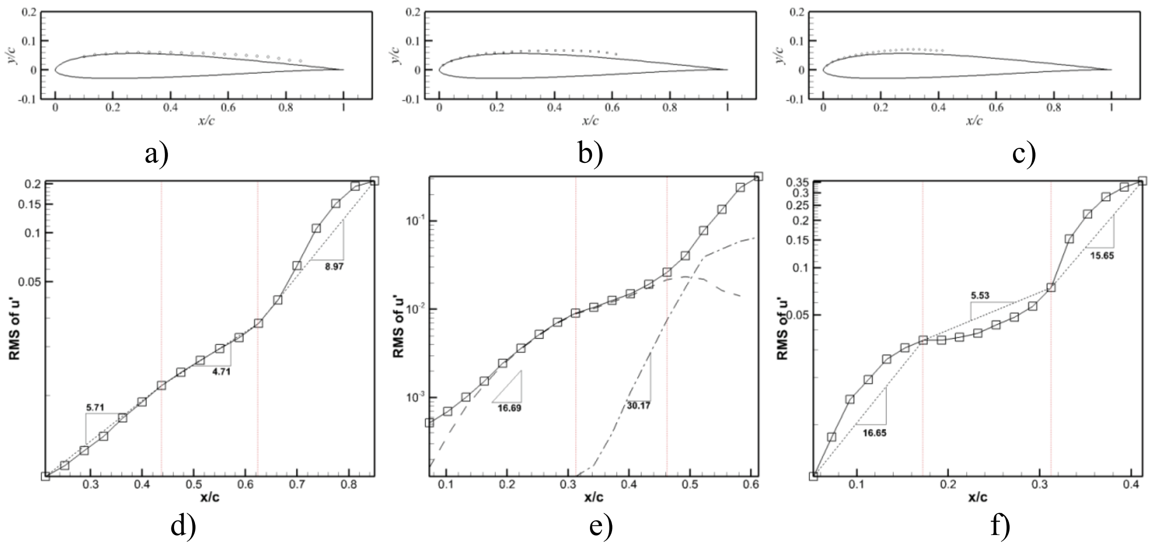

Figures 10. Numerical results of Case-2, Case-4 and Case-6 (left to right): a-c): location of probes in the flow filed; d-f): RMS tangential velocity disturbances at locations of probes.

3.2 Effects of Reynolds number

It has been seen previously that the low-frequency instability and the K-H instability are two-dimensional. For saving the computation time and being efficient, two-dimensional simulations are carried out in this section to investigate the Reynolds number effects on the low-frequency instability. Four cases in Reynolds number range $Re = 3 \times 10^4 \sim 1.2 \times 10^5$ at $AoA = 4°$ are performed by changing the viscosity as listed in Table 5. The baseline case at $Re = 6 \times 10^4$ is also included here. The contour line of Q-criteria of the instantaneous flow field and the spanwise vorticity contour of the mean flow field are shown in Fig. 11 for all cases. With the increase of the Reynolds number, the scale of the shedding vortices and the region of the separated flow decrease (Fig. 11). The separation is almost avoided at

$\mathrm{Re} = 1.2 \times 10^5$. The low-frequency component is again observed to be dominant in the attached boundary layer of all cases.

Table 5 lists the frequency, the corresponding Strouhal number and the mean growth rate of the ω_1 component for all the cases. Like the T-S and K-H instability, the frequency and growth rate can be largely affected by the Reynolds number. The frequency of ω_1 decreases with the increase of the Reynolds number, which results in the Strouhal number in a range of $\mathrm{St} = 0.005 \sim 0.130$. Although the Strouhal number at $\mathrm{Re} = 3 \times 10^4$ is close to that of the oscillating wake of a bluff body, the rest Strouhal numbers locates in a similar range in which the near stall low-frequency oscillation was observed. The average growth rate of the ω_1 component does not have a monotone trend with the increase of the Reynolds number. And the baseline case has the highest growth rate among all the four cases.

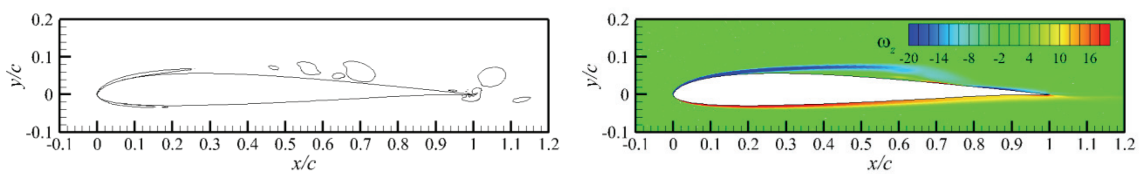

a)

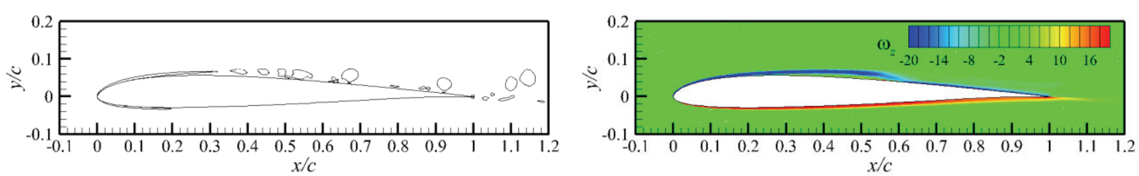

b)

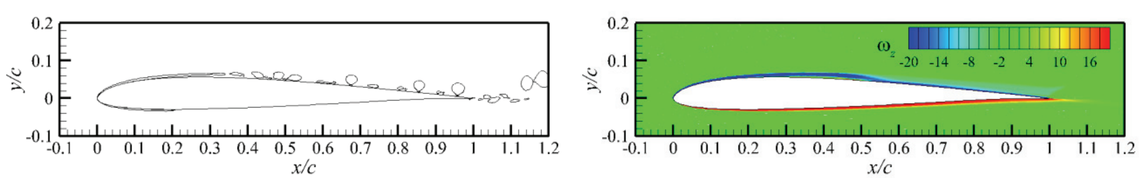

c)

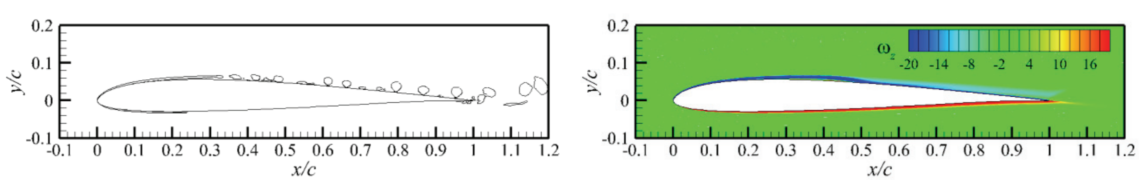

d)

Figure 11. The contour line of Q-criteria $\mathbf{Q} = \mathbf{1}$ of the instantaneous flow field (left) and the spanwise vorticity contour of the mean flow field (right). a) Case-Re-1; b) Case-Re-2; c) Case-Re-3; d) Case-Re-4.

Table 5. Characteristic frequency, Strouhal number and growth rate

Case	Re	ω_1	St	α_i
Case-Re-1	3×10^4	11.365	0.1262	≈1.672
Case-Re-2	6×10^4	3.565	0.0396	≈18.230
Case-Re-3	9×10^4	3.450	0.0383	≈13.438
Case-Re-4	1.2×10^5	0.401	0.0045	≈11.920

3.3 Effects of airfoil geometry

The effects of airfoil geometry on the low-frequency instability are further tested in this section. By changing the camber length of the original SD7003 airfoil, two cases are carried out at the same condition as the baseline case at $\mathrm{Re} = 6 \times 10^4$, $\mathrm{Ma} = 0.2$ and $\mathrm{AoA} = 4°$. As listed in Table 6, the airfoil geometries in Case-G-1 and Case-G-2 are derived by decreasing and increasing the baseline camber length by 25% respectively. Again, two dimensional simulations are carried out for computation time saving and efficiency. The 2D baseline model Case-Re-2 is also included for comparison.

Table 6 lists the frequency, the corresponding Strouhal number and the mean growth rate of the ω_1 component for the three cases. Both the frequency and growth rate vary monotonically with the camber length. The low-frequency ω_1 increases with the increase of the camber length, and the Strouhal number varies slightly around 0.038.

Table 6. Characteristic frequency, Strouhal number and growth rate

Case	ω_1	St	α_i
Case-G-1	3.311	0.0368	≈9.436
Case-Re-2	3.565	0.0396	≈18.230
Case-G-2	3.723	0.0413	≈22.334

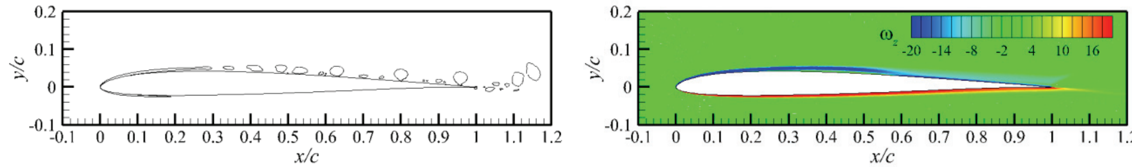

a)

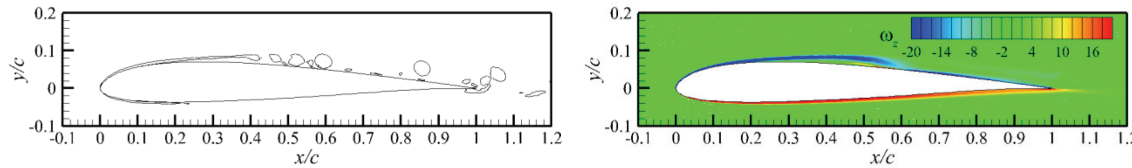

b)

Figure 12. The contour line of Q-criteria $\mathbf{Q} = \mathbf{1}$ of the instantaneous flow field (left) and the spanwise vorticity contour of the mean flow field (right). a) Case-G-1; b) Case-G-2.

4. Discussions

The present paper documents data on a phenomenon of two-dimensional low-frequency instability/oscillation of flow over an airfoil that is different in many ways from the well-known T-S wave. The instability wave oscillates at a much lower frequency but has a much higher growth rate than the T-S wave. It was suggested by Jones et al. [19] that during the process of receptivity the Lam-Rott eigensolutions (Lam & Rott [35]) of the linearized boundary layer equation is excited near the leading edge and the wavelength is much larger than that of a T-S wave. The Lam-Rott disturbance which is caused by non-parallel flow effects was found to be excited in the boundary layer receptivity process. It decreases in both amplitude and wavelength in the streamwise direction, and finally continues as a T-S wave (also see Goldstein [36] and Ricco & Wu [37]). In addition, the leading effect of a non-zero pressure gradient is to introduce a purely oscillatory factor into the disturbances as discussed in Lam & Rott [35]. However, a similar process is not observed here in all three cases. Unlike the Lam-Rott eigensolutions, the low-frequency wave is unstable and the decreasing of its wavelength in streamwise direction to continue as a T-S wave is not observed in all present cases. The K-H disturbances grow from a small amplitude $\sim 10^{-4}$ instead of being excited by the low-frequency disturbances. Near the leading edge with the increase of the AoA, the pressure gradient and growth rate of the low-frequency instability increase, but the frequency of the low-frequency decreases. However, since the airfoil flow is very complicated and usually nonlinear, the changes of the frequency and growth rate at different AoA are unlikely to be purely caused by the change of the pressure gradient. Although the pressure gradient effects are still not clear, the low-frequency instability seems unlikely to be the Lam-Rott disturbance suggested by Jones et al. [35].

Flapping of the laminar separated bubble (LSB) was observed in many previously published works of low-Reynolds number flows [10,38,39]. The flapping is an up-and-down motion of the separated shear layer. However, the low-frequency instability/ oscillation dominant in the attached boundary layer does not appear to be caused directly by the downstream flapping of the LSB to the authors. Figure 13 shows histories of the ω_1 velocity component in the range of $x = 0.1 \sim 0.25$ for the two dimensional baseline case Case-Re-2, which are derived using the inverse Fourier transformation based on the recorded velocity histories. It could be seen clearly through the peaks and valleys that the wave is downstream convective and unstable, rather than caused by the wavering of the shear layer associated with the flapping of the downstream LSB. The same conclusion can also be derived by comparing Fig. 7.a and Fig. 7.b. Spalart and Strelets [10] suggested that the transition mechanism involves the wavering/flapping of the shear layer and then K-H vortices. A wavering shear layer was defined to have a dependence of the type $u(x, y, z, t) = \tilde{u}(x, y - \tilde{y})$, where $\tilde{y}(x, z, t)$ is a statistical variable with small variations. The formula represents that the wave oscillates in y direction (normal direction). However, at the current Reynolds numbers the transverse viscosity wave is unlikely to sustain and thus their hypothesis of the wavering behavior of the shear layer seems inappropriate. The up-and-down flapping motion of the separated shear layer seems more likely to be combination result of the low-frequency oscillation in the attached boundary layer upstream and the pressure change inside the bubble.

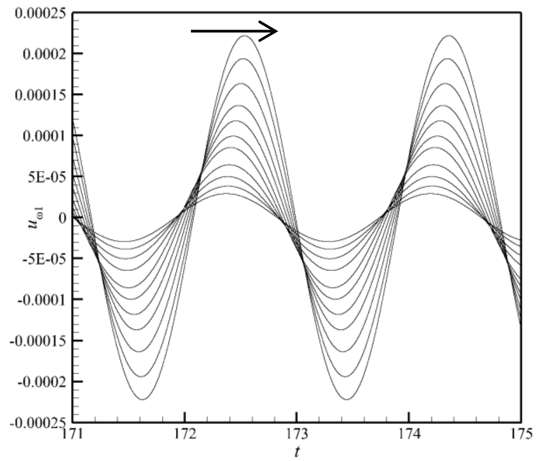

Figure 13. The histories of the $\boldsymbol{\omega_1}$ velocity component in the range of $\mathbf{x = 0.1 \sim 0.25}$ in Case-Re-2.

5. Conclusions

Various questions have remained unanswered but the following inferences have been clearly made: (1) A low-frequency oscillation in the attached boundary layer is observed in the present study. The low-frequency instability is found to be apparently two dimensional and convective unstable. (2) The primary growth of the disturbances before the turbulent breakdown over the suction side of the airfoil consists of two stages. The first stage is dominated by the low-frequency instability and the second growth stage is caused by the K-H instability. (3) The phenomenon is hydrodynamic in nature. The low-frequency instability is neither the famous T-S instability nor the result of the Lam-Rott eigensolutions of the receptivity theory. And it seems not to be caused by the flapping of the downstream bubble and the detached shear layer.

The low-frequency oscillation in the present cases occurs in the Strouhal number range of $\mathrm{St} = 0.005 \sim 0.130$, and the Strouhal numbers are in the same magnitude of the low-frequency oscillation of the airfoil flow near stalling conditions as reported in several previously published papers. It is conjectured that the low-frequency instability in the present cases may be the same mechanism of the near stall low-frequency oscillation. It is interesting to find that the Strouhal number keeps almost constant at moderate $\mathrm{AoA} = 2°, 4°$ and $6°$. In the testing of the airfoil geometry effects, the frequency and growth rate vary monotonically with the camber length. However, unlike the low-frequency oscillation near the stalling condition, the Strouhal number and the growth rate of the low-frequency instability change largely with the Reynolds number.

Acknowledgments

The authors would like to acknowledge the support from the Air Force Office of Scientific Research and the Department of Aerospace Engineering, Iowa State University.

References

[1] Owen, P. R. and Klanfer, L. On the laminar boundary layer separation from the leading edge of a thin aerofoil. 1953 ARC Conf. Proc. 220.

[2] Gaster, M. 1963 On stability of parallel flows and the behaviour of separation bubbles. PhD Dissertation, University of London.

[3] GASTER, M. 1967 The structure and behaviour of separation bubbles. Aero. Res. Counc. R&M 3595. Aerodynamics Division NPL.

[4] HORTON, H. P. 1967 A semi-empirical theory for the growth and bursting of laminar separation bubbles. Aero. Res. Counc. Current Paper 1073.

[5] HORTON, H. P. 1968 Laminar separation in two and three-dimensional incompressible flow. PhD Dissertation, University of London.

[6] PAULEY, L. L., MOIN, P. & REYNOLDS, W. C. 1990 The structure of two-dimensional separation. J. Fluid Mech. 220, 397-411.

[7] PAULEY, L. L. 1994 Response of two-dimensional separation to three-dimensional disturbances. Trans. ASME: J. Fluids Engng 116, 433–438.

[8] RIST, U. 1994 Nonlinear effects of 2D and 3D disturbances on laminar separation bubbles. Proc. IUTAM Symp. on Nonlinear Instability of Nonparallel Flows, pp. 324–333. Springer.

[9] ALAM, M. & SANDHAM, N. D. 2000 Direct numerical simulation of 'short' laminar separation bubbles with turbulent reattachment. J. Fluid Mech. 410, 1–28.

[10] SPALART, P. R. & STRELETS, M. K. H. 2000 Mechanisms of transition and heat transfer in a separation bubble. J. Fluid Mech. 403, 329–349.

[11] MARXEN, O., LANG, M., RIST, U. & WAGNER, S. 2003 A combined experimental/numerical study of unsteady phenomena in a laminar separation bubble. Flow, Turbulence Combust. 71, 133–146.

[12] LANG, M., RIST, U. & WAGNER, S. 2004 Investigations on controlled transition development in a laminar separation bubble by means of LDA and PIV. Exp. Fluids 36, 43–52.

[13] H. HU AND Z. YANG, "An Experimental Study of the Laminar Flow Separation on a Low Reynolds Number Airfoil", ASME Journal of Fluid Engineering, Vol.130, No.5, 051101, 2008.

[14] YARUSEVYCH, S., SULLIVAN, P.E. & KAWALL, J.G. 2009 On vortex shedding from an airfoil in low-Reynolds-number flows. J. Fluid. Mech. 632, 245-271

[15] HAIN, R., KAHLER, C. J. & RADESPIEL, R. 2009 Dynamics of laminar separation bubbles at low-Reynolds-number aerofoils. J. Fluid Mech. 630, 129–153.

[16] Y. Sun, Z.J. Wang, Y. Liu, High-Order Multi-domain Spectral Difference Method for the Navier-Stokes Equations on Unstructured Hexahedral Grids, Communications in Computational Physics, Vol. 2, No. 2(2007) 310-333.

[17] DENG, S., JIANG, L. & LIU, C. 2007 DNS for flow separation control around an airfoil by pulsed jets. Comp. Fluids 36 (6), 1040–1060.

[18] ZHOU, Y. & WANG, Z. J. 2010 Implicit Large Eddy Simulation of Transitional Flow over a SD7003 Wing Using High-order Spectral Difference Method, AIAA-2010-4442

[19] JONES, L. E., SANDBERG, R. S. & SANDHAM, N. D 2010 Stability and receptivity characteristics of a laminar separation bubble on an aerofoil. J. Fluid Mech. 648, 257–296.

[20] DRAZIN, P. G. 2002 Introduction to hydrodynamic stability. Cambridge University Press, ISBN 0 521 00965 0.

[21] YARUSEVYCH, S., SULLIVAN, P.E. & KAWALL, J.G. 2009 On vortex shedding from an airfoil in low-Reynolds-number flows. J. Fluid. Mech. 632, 245-271.

[22] YANG, Z. & VOKE, P.R. 2001 Large-eddy simulation of boundary-layer separation and transition at a change of surface curvature. J. Fluid. Mech. 439, 305-333.

[23] WATMUFF, J. H. 1999 Evolution of a wave packet into vortex loops in a laminar separation bubble. J. Fluid Mech. 397, 119–169.

[24] P. L. Roe, Approximate Riemann solvers, parameter vectors, and difference schemes, J. Comput. Phys. 43 (1981) 357-372.

[25] D.A. Kopriva, J.H. Kolias, A Staggered-Grid Multi-domain Spectral Method for the Compressible Navier-Stokes Equations, J. Comput. Phys. 143 (1998) 125-158.

[26] Malik, M. R. 1990 Numerical methods for hypersonic boundary layer stability, Journal of Computational Physics 86, 376-413.

[27] HU, S.AND ZHONG, X. L. 1998 Linear stability of viscous supersonic plane Couette flow, Phys. Fluids 10, 709 (1998).

[28] Zhou, Y. & Wang, Z. J. 2010 Implicit Large Eddy Simulation of Transitional Flow over a SD7003 Wing Using High-order Spectral Difference Method, AIAA-2010-4442.

[29] Zhou, Y. & Wang, Z. J. 2010 Absorbing Boundary Conditions for the Euler and Navier-Stokes Equations with the Spectral Difference Method, Journal of Computational Physics 229, 8733-8749.

[30] Hunt, J. C. R., Wray, A. A. and Moin, P. (1988). Eddies, stream, and convergence zones in turbulent flows. In Center for Turbulence Research Report, pp. 193-208. Stanford, USA: Center for Turbulence Research.

[31] K. B. M. Q. Zaman, D. J. Mckinzie and C. L. Rumsey, A natural low-frequency oscillation of the flow over an airfoil near stalling conditions. Journal of Fluid Mechanics (1989), 202: 403-442.

[32] Bragg M. B., Heinrich D. C. and Khodadoust A. Low-Frequency Flow Oscillation over Airfoils near Stall, AIAA Journal, Vol. 31, No. 7, pp 1341-1343, 1993.

[33] Rinoie K and Takemura N. Oscillating Behaviour of Laminar Separation Bubble Formed on an Airfoil Near Stall, Aeronautical Journal, Vol. 108, No. 1081, pp 153-163, 2004.

[34] A. P. Broeren and M. B. Bragg low-frequency flowfield unsteadiness during airfoil stall and the influence of stall type. AIAA paper AIAA-98-2517

[35] Lam, S. H. & Rott, N. 1960 Theory of Linearized Time-Dependent Boundary Layers. Graduate School of Aeronautical Engineering, Cornell University.

[36] GOLDSTEIN, M. E. 1983 The evolution of Tollmien–Schlichting waves near a leading edge. J. Fluid Mech. 127, 59–81.

[37] P. RICCO AND X. WU. Response of a compressible laminar boundary layer to free-stream vortical disturbances. J. Fluid Mech., 587:97–138, 2007.

[38] Wissink, J. & Rodi, W. 2004 DNS of a Laminar Separation Bubble Affected by Free-Stream Disturbances. Springer/Kluwer Academic.

[39] Wilson, P. G. & Pauley, L. L. 1998 Two- and three-dimensional large-eddy simulations of a transitional separation bubble. Phys. Fluids 10, 2932–2940.

CHAPTER 4. The breakdown of laminar separation bubbles on a low-Reynolds number airfoil at incidences

A paper submitted to AIAA Journal

Ying Zhou and Z.J. Wang

Abstract

The present paper focuses on the study of breakdown processes of laminar separation bubbles on an SD7003 airfoil at Reynolds number $Re = 60{,}000$ at three angles of attack (AoAs) $= 2°, 4°$ and $6°$. Extensive numerical simulations are performed to determine the transition mechanism for such flows. In an earlier paper (Zhou & Wang 2011), the primary growth in the boundary layer and the subsequent vortex shedding due to the Kelvin-Helmholtz instability before the vortex breakdown are investigated. It is observed that the breakdown of the shedding vortices starts at approximately the location with the maximum negative streamwise flow velocity. We also found that the reverse flow in the separation region directly triggers the generation of three dimensional disturbances and the streamwise vorticities. In addition, the secondary instability which initiates the breakdown process differs for cases at different AOAs. The elliptic and hyperbolic instabilities observed in bluff-body wakes are found to occur in the breakdown process of current cases. Furthermore, the sequence of breakdown states at various incidences is found to be similar to that of the bluff-body wakes at various Reynolds numbers.

1. Introduction

In the past decade, low-Reynolds-number flows and the associated laminar separation bubbles (LSBs) have been of great interest in the development of micro air vehicles (MAV), small scale wind turbines and low-pressure turbine/cascade. Since laminar boundary layers are less resistible to the significant adverse pressure gradient (APG), LSBs are widely found over the suction side of low-Reynolds-number airfoils/turbines at moderate incidences. The flow quickly transitions into a turbulent one and reattaches downstream after the breakdown of LSBs. For airfoils, the behavior of the LSB affects the aerodynamic performance and typically causes the increase of the pressure drag. Meanwhile, the existence of a turbulent boundary layer induces higher friction force on the airfoil than a laminar flow, and therefore can cause the degradation of the lift-to-drag ratio. Jones (1938) made the first observations of laminar separation bubbles. Early works on LSB and associated hydrodynamic instability mechanisms can be traced back to the 1950s (Owen & Klanfer 1953) and 1960s (Gaster 1963, 1967; Horton 1968, 1969). At the current Reynolds number and incidences, the LSBs can all be classified as the 'short' bubbles according to Owen & Klanfer (1953). The general development of the separated and transitional 'short' bubble flow and the typical distribution were depicted by Horton (1968 & 1969). Distinct from the convective types of transition, the simultaneous presence of and the interaction between separation and transition make the problem highly complicated.

With the rapid development of numerical methods, numerical simulations of laminar separated flows have been used to investigate the LSB and the associated turbulent transition. Two-dimensional simulations of separation bubbles were first investigated by Pauley et al. (1990). Pauley (1994) and Rist (1994) carried out three-dimensional studies of the primary instability later, but the transition was still not resolved due to the limitation of the computational resource and computer technology. More recently, direct numerical simulations (DNS) to fully resolve the transition of LSBs to turbulence were conducted by Alam & Sandham (2000) and also Spalart & Strelets (2000). With the development of experimental techniques, Laser-Doppler-Anemometry (LDA) and Particle-Image-Velocity (PIV) technologies can provide the flow field measurements to quantify the evolution of the unsteady flow structure and investigate the dynamics of LSBs (see Marxen et al. 2003; Lang et al. 2004; Hu & Yang 2008; Yarusevych et al. 2009; Hain et al. 2009). A review of the receptivity process in generating the initial disturbances, the primary growth of the disturbances and the possible absolute instability in the separated and transitional flows can be found in Zhou & Wang (2011). In spite of considerable progresses in recent years, both the LSB and the transition mechanism still need further investigation. In a previous paper of the authors (Zhou & Wang 2011), the primary instabilities which accounts for the growth of disturbances in the laminar flow region were investigated under the same initial conditions. A low-frequency instability was found in the attached boundary layer, which has a high growth rate than the Tollmien-Schlichting wave and could not be predicted by the linear stability theory (LST). The Kelvin-Helmholtz instability plays the dominant role in disturbance growth after the flow separates, where both the disturbance growth rate and vortex shedding frequency were found in good agreement with the results of LST.

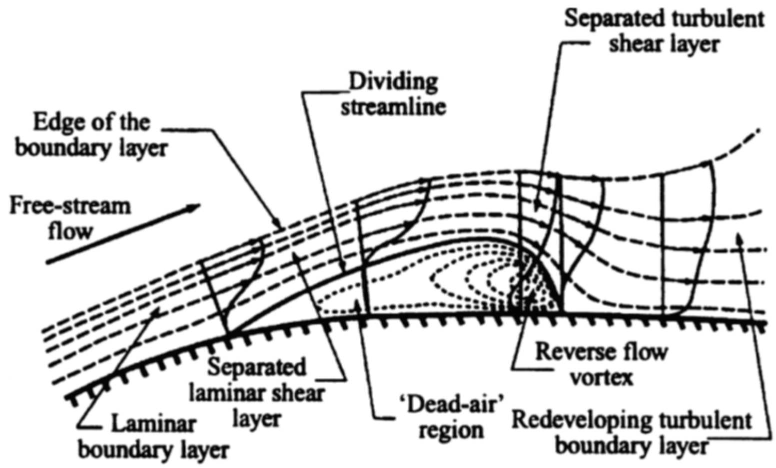

FIGURE 1. Time-averaged laminar separation bubble (Horton 1968).

This paper is concerned with the breakdown of the LSBs on a low-Reynolds number SD7003 airfoil at incidences. The breakdown to turbulent flow occurs more abruptly than the receptivity and disturbance-growth stages. In different flows, there are different possible scenarios for the breakdown process but it is generally accepted the breakdown is caused by the uncontrolled growth of unstable three dimensional waves. The so-called secondary instability in compare with the primary instability is responsible for the growth of the three dimensional disturbances. The counter-rotating vortex pairs (e.g. Λ-vortex and hairpin vortex) are widely observed in the breakdown process of various flows. The fundamental mode (K-type by Klebanoff et al. 1962) and the subharmonic mode (H-type by Herbert 1984) are two types of breakdown identified in the early study of transition process. With the increase of the disturbance level, bypass transition would occur and the turbulent spot associated with the local breakdown triggers the fully turbulent flow by its own growth and merging with the laminar flow (e.g. Jacob & Durbin 2001 and Ovchinnikov et al. 2008). Obviously, the breakdown process occurring in nature does not limit to these types.

For LSB flows, the breakdown process usually occurs in the separated turbulent shear layer region (figure 1) at where the perturbed velocity distribution is observed by Horton (1969). The separated flow reattaches to the wall after the process of breakdown and the LSBs are usually followed by turbulent flow. Alam & Sandham (2000) found that the separated shear layer undergoes transition via oblique modes and Λ-vortex induced breakdown. The occurrence of counter-rotating vortex pairs was also observed in the breakdown of LSBs in Lang et al. (2004). Yang & Voke (2001) suggested that the breakdown is characterized by the irregular shedding of large-scale vortices associated with free shear-layer roll-up. After impinging on the wall and the formation of hairpin vortices a turbulent boundary layer forms rapidly. In McAuliffe & Yaras (2010), breakdown occurs in a time-periodic manner within the braid high-shear region between spanwise vortices. It was found by Jones et al. (2008) that the perturbations of a braid region are convected into the region of the upstream developing vortex and affects the vortex tube. The braid region was first observed in the breakdown of a mixing-layer flow (Moser & Rogers 1991), then later in the bluff-body wakes (Williamson 1996) and the flows over airfoils (Jones et al. 2008). However, the streamwise vortices and braid region were not observed in the separated bubble of Spalart & Strelets (2000), instead a mechanism of 'transition by contact' due to flow reversal near the end of the separated bubble was proposed. In the separation bubble, the return flow brings turbulent fluid into contact with laminar fluid and the three dimensional disturbances are brought to the shedding vortices which trigger the breakdown process.

Jones et al. (2008) observed that the elliptical and hyperbolic instabilities may have appeared during the breakdown process of the shedding vortex in the low-Reynolds number airfoil flow, and the instability in their case was found to be hyperbolic instability. In the context of bluff body-wakes, the generation and stretching of streamwise vortex pairs around the primary Karman vortex structures are commonly attributed to elliptic instability (Thompson, Leweke & Williamson 2001) and hyperbolic instability (Leweke & Williamson 1998), which were denoted as mode-A and mode-B respectively (Williamson 1996). Bayly et al. (1988) suggested that the elliptic instability is an important mechanism in the breakdown process of many flows. Elliptic and hyperbolic instabilities are the names given to the instability of elliptical and hyperbolic two-dimensional streamlines to three-dimensional perturbations. It has been suggested that, elliptical instability is basically caused by the instability of the shedding vortex core (Williamson 1996; Thompson, Leweke & Williamson 2001), which occurs in conjunction with deformation of the cortex core and the streamwise vortices show an out-of-phase pattern. The spanwise wavelength of the most amplified elliptical instability was suggested to be of the order $\lambda = 3D$ by Williamson (1996) and Thompson, Leweke & Williamson (2001), where D is the diameter of the region of elliptical core. Hyperbolic instability (Mode-B) involves instability of the braid shear layers (Leweke & Williamson 1998) associated with spanwise wavelength $\lambda = D$, which occurs with no deformation of the vortex core and the streamwise vortices in braid region show an in-phase pattern (Williamson 1996). In bluff body wakes, Mode-A is first observed at $Re_d > 190$ and Mode-B is first observed at $Re_d > 240$, where Re_d is the Reynolds number based on cylinder diameter.

As a continuous work of Zhou & Wang (2011), the current study focuses on the breakdown process of the current LSBs, and aims at providing the possible strategies of flow control and improving the aerodynamic design of airfoils. The paper is organized as follows. In § 2, the computational details are briefly introduced. § 3 presents the instantaneous and statistical numerical results. And the description and investigation of the breakdown process are then made based on the results. Discussion and conclusions are given in § 4 and § 5.

2. Details of numerical simulations

Spectral difference method on unstructured hexahedral mesh is used to solve the unsteady compressible Navier-Stokes equations in this paper, and an introduction of this method is introduced in detail in Zhou & Wang (2011). All the variables in this paper are non-dimensional unless specifically noted. Figure 2 shows the computational mesh for the present simulations. The mesh is refined near the wall and around the physically important region where the separation bubble and vortex breakdown occur. The smallest cell is located at the trailing edge with dimension (in wall units) $\Delta y^+ = 2.5$ in the direction normal to the wall, $\Delta x^+ = 25.0$ in the flow direction and $\Delta z^+ = 12.0$ in spanwise direction, noting that inside the cell each direction is discretized by the solution/flux points. The total number of cells is 253,600, resulting in 6,847,200 and 16,230,400 degree-of-freedom (per equation) for the 3rd-order and 4th-order SD schemes respectively. The numerical simulations are carried out at a Reynolds number based on the airfoil chord of $Re_c = 6 \times 10^4$ and Mach number $M = 0.2$. Three cases with different AoA are investigated in this paper, as shown in Table 1. In the current simulation, no subgrid-scale model is used so the numerical simulations can be regarded as an Implicit Large Eddy Simulation (ILES).

TABLE 1. Numerical simulation cases

Case	AoA
Case-2	2
Case-4	4
Case-6	6

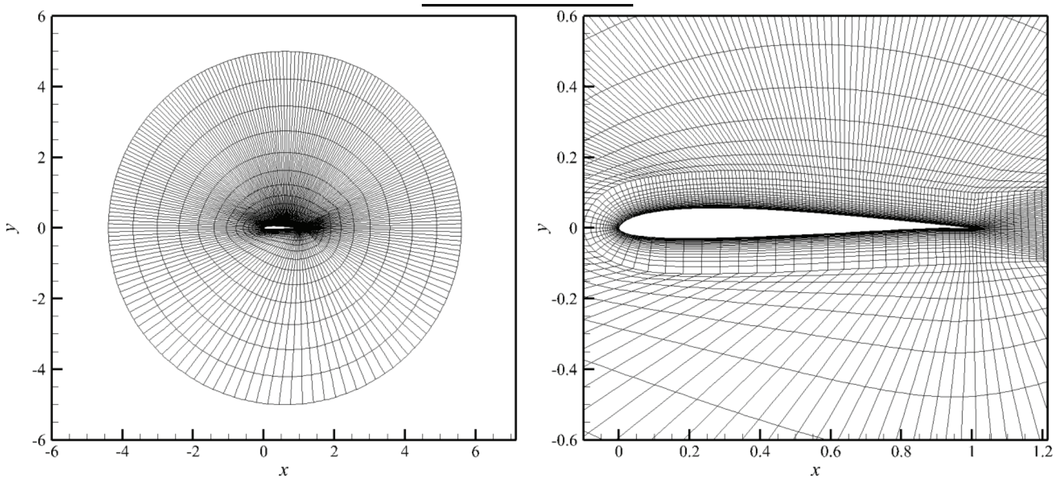

FIGURE 2. Computational mesh.

The flow field is initiated with the freestream condition. In order to simulate an infinite wing, a periodic boundary condition is used in the spanwise direction and the span width of the wing is set to be 20% of the chord. A no-slip, adiabatic boundary condition is applied on the surface of the wing. The far-field boundary is set to be 5 times of the chord length. At the far-field of the computational domain, the absorbing sponge zone (ASZ) (Zhou & Wang 2010) is used to absorb the out-going disturbances.

A polynomial order (p) refinement study is carried out in Zhou & Wang (2011) by increasing the order of the polynomial in each element cell from 2 (resulting in 3rd-order accuracy) to 3 (resulting in 4th-order accuracy). The averaged and statistical results computed with both the 3rd and 4th order schemes have been shown to be very close to each other (Zhou & Wang 2011), which indicates that the unsteady solution is nearly order independent on this mesh, and the mean flow has been order-independent and the spatial resolution provided by 4th-order method is capable of capturing the main flow features at the current Reynolds number. In both Zhou & Wang (2011) and this paper, the mean flow field and the statistical results are obtained by averaging the instantaneous flow field at each time step and performed over 5 non-dimensional time ($=t^{*}/(C/U_{\infty})$) units. The numerical results shown in the rest of the paper are the results of 4^{th}-order SD scheme unless specified.

3. Breakdown of the shedding vortices

The LSBs and turbulent transition are observed over the suction side of the airfoil in all the present cases. Figure 3 shows the iso-surfaces and contour lines of the Q-invariant (Dubeif and Delcayre 2000) for all three cases. Vortex shedding is observed on the suction side in all three cases after separation and the vortex breakdown occurs in a later stage. Turbulent boundary layer forms on the suction side at $\mathrm{AoA}=4^{\circ}$ and 6°. At $\mathrm{AoA}=2^{\circ}$ three dimensional structures appear on the suction side and pass the trailing edge without the formation of smaller turbulent structures. The separation moves upstream and the length of the LSB reduces with the increase of the AoA.

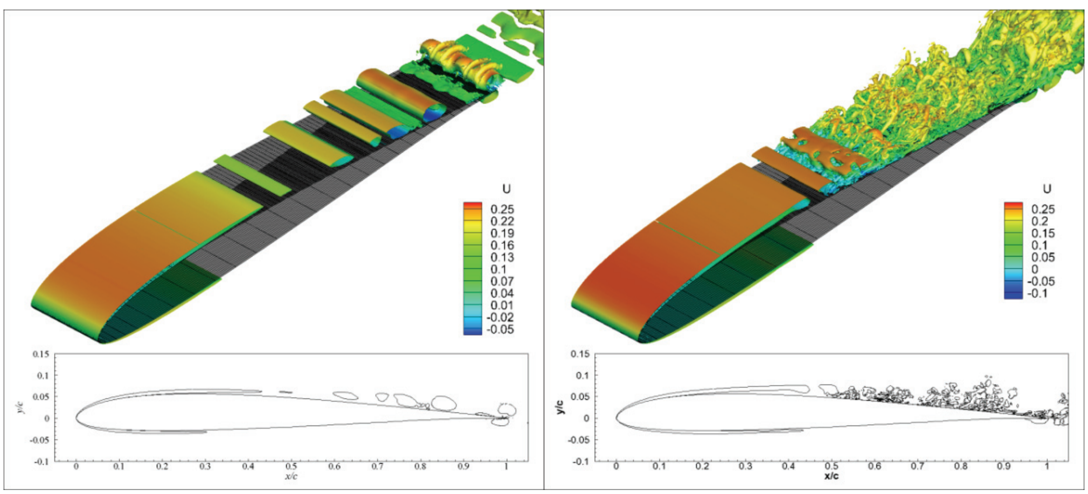

(a) (b)

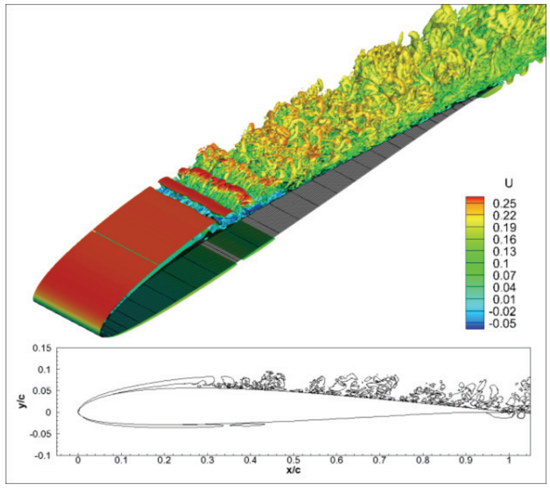

(c)

FIGURE 3. Iso-surface and contour line of Q-invariant: (a) Case-2; (b) Case-4; (c) Case-6.

The averaged and statistical results of Case-4 are shown in figure 4. Figure 4.a shows the mean streamlines around the wing and the mean streamwise velocity field averaged in both time and spanwise direction. The mean separation bubble and the reattachment of the flow are clearly shown. In Figure 4.b, on the suction side of the airfoil, the low value of the mean spanwise vorticity ($\omega_z \approx -20$) at interval $x = [0.0,0.6]$ displays the laminar shear layer before the flow transitions to turbulence. The interval $x = [0.0,0.6]$ corresponds to the so-called primary instability region of the transition process. Shedding vortices due to the K-H instability are observed in the detached shear layer (figure 3). The LSB is closed after the breakdown of shedding vortices, and a turbulent boundary layer forms at $x = [0.7,1.0]$ (figures 3.b and 4.b). Figure 4.c&d show the statistical distribution of the normalized turbulent kinetic energy $\left(T.K.E. = 1/2\left(\overline{u'^2} + \overline{v'^2} + \overline{w'^2}\right)/U_\infty^2\right)$ and the normalized Reynolds stress $\left(\tau_{xy} = -\overline{u'v'}/U_\infty^2\right)$, respectively. Both the $T.K.E.$ and Reynolds stress τ_{xy} concentrate and reach the maximum around $x = 0.65$ where the shedding vortex breakdown occurs (figure 3.b). The above results of the other two cases are found quite similar to Case-4, thus are not shown here for briefness.

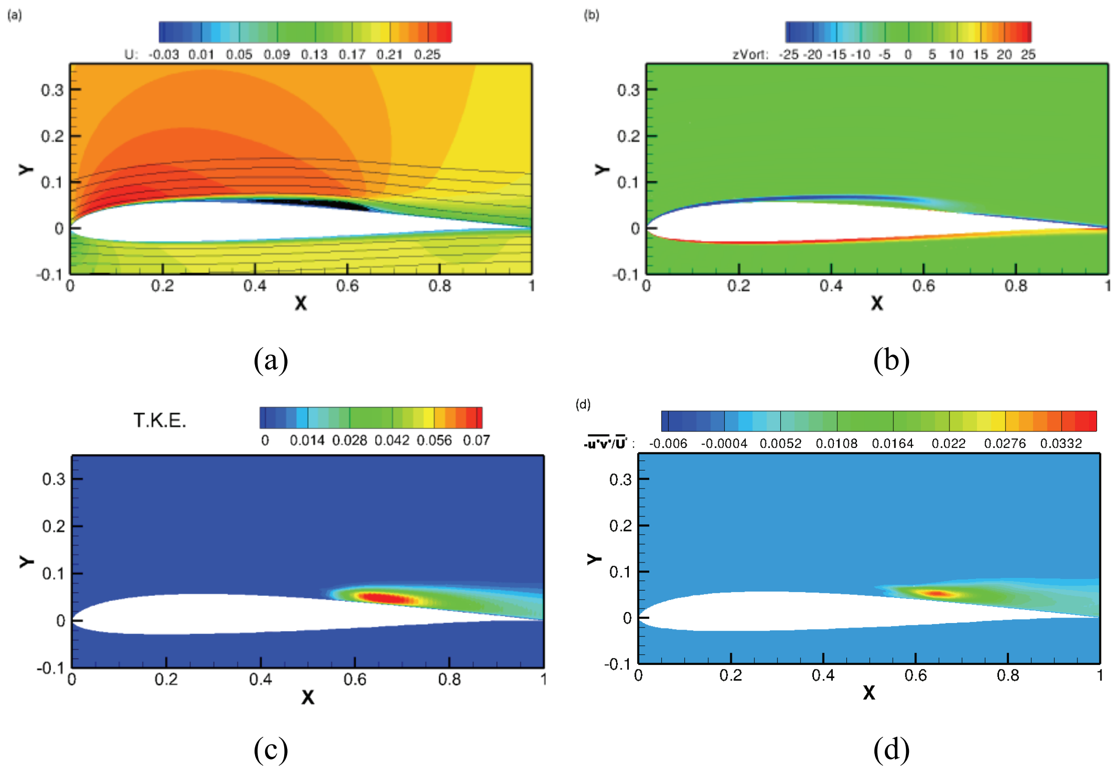

(a) (b)

(c) (d)

FIGURE 4. Mean and statistical results of Case-4: (a) mean streamlines around the wing and mean streamwise velocity field; (b) mean spanwise vorticity field; (c) normalized Reynolds stress (τ_{xy}) distribution.

The breakdown of the shedding vortices is the last stage of the transition process. Similar to the various types of transition in the attached boundary layer flow, the breakdown of the separated flows in current cases abrupts in a sudden and is much shorter than the primary instability stage. The breakdown of the shedding vortices is caused by the secondary instability, but the precise nature of the secondary instability mechanism is not fully understood. It is interesting to find that in all the current cases the breakdown stage occurs in the region where the separated flow reattaches to the wall and the separated bubble is closed. This region was previously labeled as separated turbulent shear layer associated with the reverse flow vortex in figure 1 by Horton (1968). In this section, the breakdown processes in the current cases are investigated and discussed. For comparison, 2D simulations with the same initial condition and AoAs are also presented.

Figure 5 shows the mean pressure coefficient C_p and mean friction coefficient C_f of both 3D and 2D simulations for Case-2, Case-4 and Case-6. The features and tendencies of the C_p and C_f curves are quite similar between 2D and 3D results at the same incidence, which can be summarized as:

Feature-1. A pressure plateau in the LSB region.

Feature-2. A rapid increase/recovery of the pressure accompanied by a strong separation.

Feature-3. Reattachment of the flow.

Reattaching of the separated flow (feature-3) occurs in both 2D and 3D cases, and at the same incidence the mean flow reattaches the wall even a bit earlier in 2D cases than in 3D cases, as shown in figure 5. The pressure plateau (feature-1) has been widely declared in the low-Reynolds number airfoil flows at incidences, which implies that pressure keeps almost constant inside the LSBs. At all three incidences, the mean separation region appears to be of two stages. In the first stage ($x = 0.23 \sim 0.55$ in 3D Case-4), the separation is moderate and coincides to the pressure plateau region as shown in figure 5. In the second stage ($x = 0.55 \sim 0.68$ in 3D Case-4), the separation is much stronger (figure 5). It seems that the second separation region is always associated with a rapid increase/recovery of the pressure (feature-2), which can also be found in many low-Reynolds number airfoil/turbine flows, e.g. Fasel et al. (2008), Jones et al. (2008) and Zaki et al. (2010). In the current 3D simulations, the secondary instability and breakdown process are found to start in the same zone where feature-2 is observed and near the location with the maximum negative streamwise flow velocity. In the following of this paper, we call this zone the Recovery-Separation (R-S) region, which should be distinguished from the leading-edge separation. The R-S region for 3D simulations refers to $x = (0.75,\ 0.90)$ in Case-2, $x = (0.55,\ 0.68)$ in Case-4 and $x = (0.33,\ 0.48)$ in Case-6, as shown in figure 5.a. The similarity between 2D and 3D results shows that the three features of C_p and C_f curves does not directly relate to the breakdown process. It will been seen later that in all 3D cases the flow becomes three dimensional after passing this region, and the R-S region is strongly associated with the secondary instability and the breakdown of the shedding vortices. The $T.K.E.$ and τ_{xy} are also found to be concentrated in the same R-S region for 3D Case-4 as shown in figure 4.c&d.

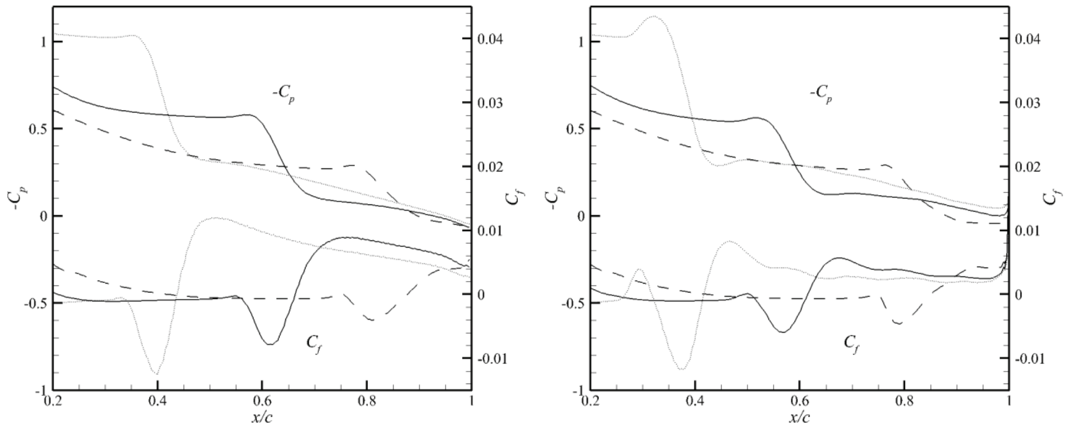

(a) (b)

FIGURE 5. Pressure coefficient C_p and friction coefficient C_f along the suction surface: (a) 3D results; (b) 2D results. (dash line) Case-2, (solid line) Case-4, (dot line) Case-6

The contours of the mean total pressure $P_{Total} = \frac{1}{2}\rho U^2 + P$ normalized by $\frac{1}{2}\rho_\infty U_\infty^2$, the mean pressure coefficient C_p distribution and the pressure gradient magnitude $|\nabla P|$ for the 3D Case-4 are shown in figure 6. Both the total pressure and the static pressure are almost constant inside the LSB region and are lower inside the LSB than those outside the LSB. In other words, in the averaged sense the LSBs persist a constant low pressure inside and are pressed by high-pressure outside. Around the location $x = 0.65$, there exists a region of high APG as shown in figure 6.c and the APG terminates the LSB. This area around $x = 0.65$ is exactly the R-S region where the breakdown and reattachment are observed in 3D Case-4. In the sense of the mean flow field, the pressure difference is balanced by the friction force over the wall as shown in figure 5.a. The above characters illustrates that the breakdown process is highly related with feature-2 in the R-S region. The above tendencies and phenomena of the mean flow filed in the breakdown region are found to be quite similar in the other two cases. However, the instantaneous breakdown processes are quite different from case to case. The different breakdown processes are described and discussed in detail in the following sections.

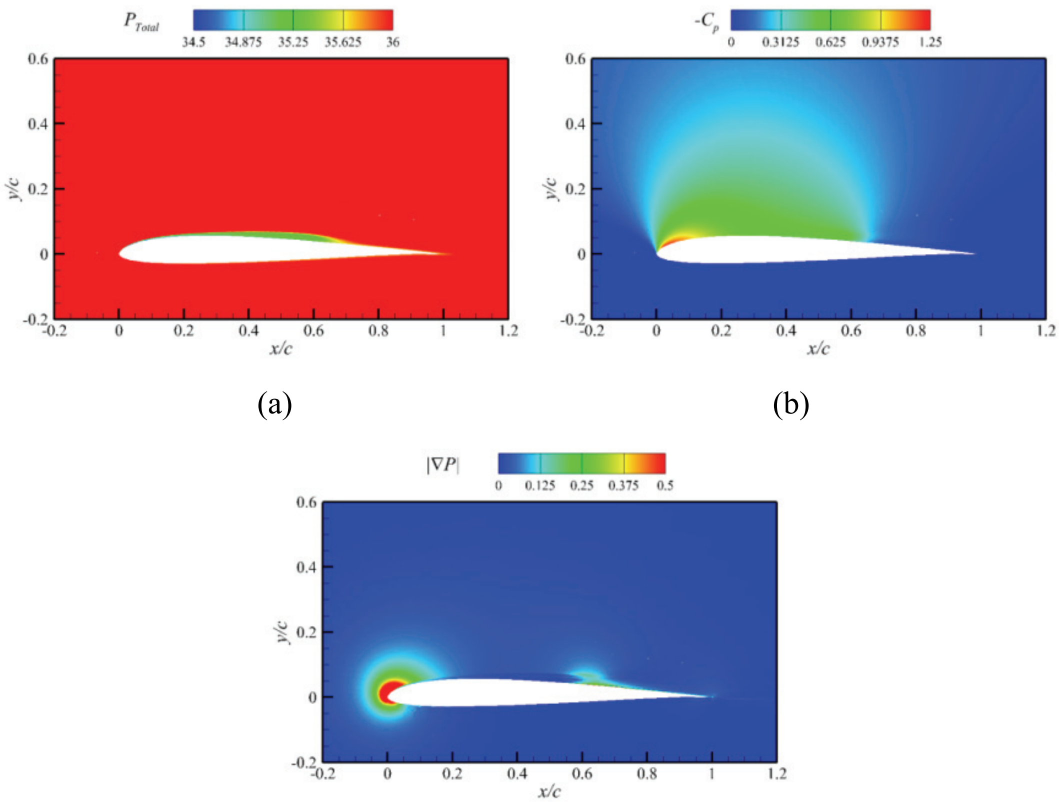

(a) (b)

(c)

FIGURE 6. Averaged numerical results for Case-4: Contours of (a) normalized total pressure P_{Total}; (b) pressure coefficient C_p; (c) pressure gradient magnitude $|\nabla P|$.

3.1 The breakdown process of Case-2

Figures 7 and 8 show the side view of the contours of Q-invariant and spanwise vorticity ω_z in Case-2 for both the 2D and 3D simulations. For similarity and briefness, four phases for roughly a period of the shedding vortex are shown for the 2D simulation and only one instantaneous phase is shown for 3D simulation. These results are quite close between the 2D and 3D simulations, although three dimensional disturbances appear close to the trailing edge for 3D Case-2 (figure 3.a). The shedding vortices grow convectively in the detached shear layer. After entering the R-S region $x = (0.75,\ 0.90)$ in both 2D and 3D Case-2, the shedding vortex contacts with the wall and aggregates due to the slowdown of propagation. The vortex rotates in the clockwise direction, thus would gain the friction force which help the vortex propagate downstream. The slowdown of the shedding vortices in the R-S region is mainly due to the strong APG in the same region, as shown in figure

6.c for Case-4 and similarly for Case-2. Forced by the mainstream flow and the skin-friction force, the vortex propagates from the low-pressure side towards the high-pressure side and finally escapes the R-S region (figures 7 and 8). After leaving this region, the vortex propagates towards the traling edge rapidly.

The appearance of the three dimensional disturbances in 3D Case-2 is clearly illustrated in figure 9 by the instantaneous iso-surfaces of Q-invariant $Q = 0.25$ and streamwise vorticity $\omega_x = \pm 0.25$ for four phases within one shedding cycle. Three dimensional disturbances appear after the shedding vortex passing through the R-S region. In figure 9, two periods of the spanwise wave are observed in the figures of ω_x, and the corresponding skewness of the vortex core is shown by the iso-surfaces of Q-invariant (figure 9). Figure 10 shows the side views of the spanwise vorticity and streamlines at phase $\phi = 0$. In the current case, the vortex core is perturbed at spanwise wavelength $\lambda = 0.1$ (figure 9) and the diameter of the vortex core ($x = 0.85$) in the R-S region is approximately $D_s \approx 0.016$ in wall normal direction and $D_L \approx 0.048$ in wall tangential direction as shown in figure 10. The resulting $\lambda/\bar{D} \approx 3.125$ $(\bar{D} = (D_s + D_L)/2)$ is quite close to feature of the most amplified elliptical instability (Mode-A) $\lambda/D \approx 3$ which was early identified in bluff-body wakes (Williamson 1996). As shown by the iso-surfaces of Q-invariant in figure 9, the deformation of the primary shedding vortex core can be seen clearly and no braid region between two consecutive shedding vortices is observed in the R-S region.

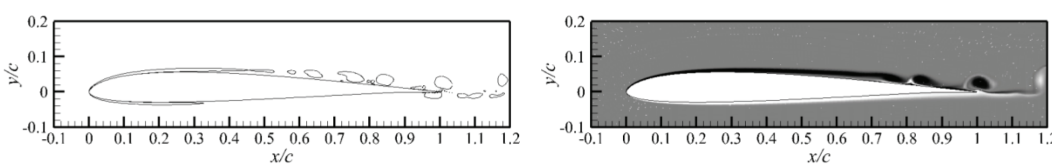

(a)

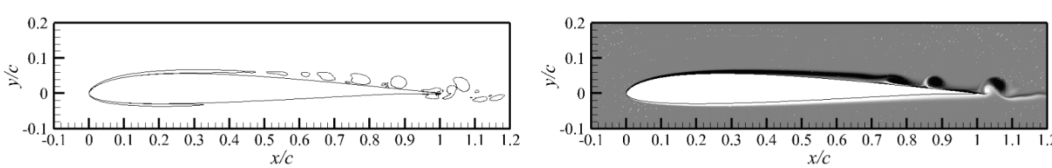

(b)

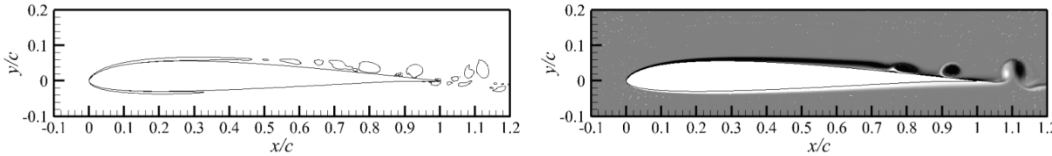

(c)

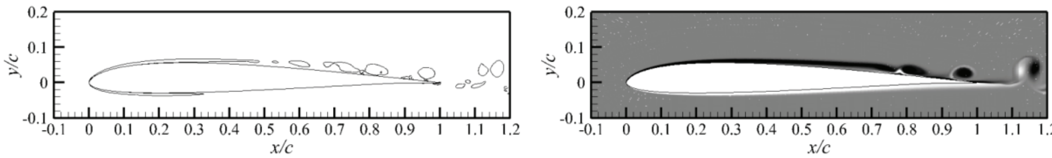

(d)

FIGURE 7. Contours of Q-invariant (left) and spanwise vorticity (right) of the 2D Case-4 for four phases in one shedding period: (a) $\phi = 0$, (b) $\phi = \frac{\pi}{2}$, (c) $\phi = \pi$, (d) $\phi = \frac{3\pi}{2}$.

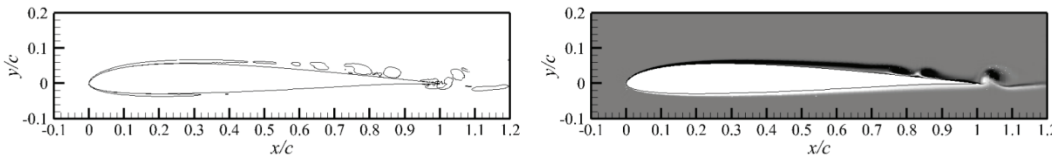

FIGURE 8. Contours of Q-invariant (left) and spanwise vorticity (right) of the 3D Case-4 at phase $\phi = 0$.

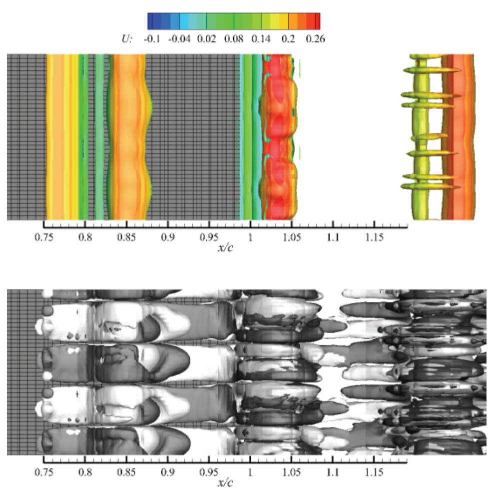

(a)

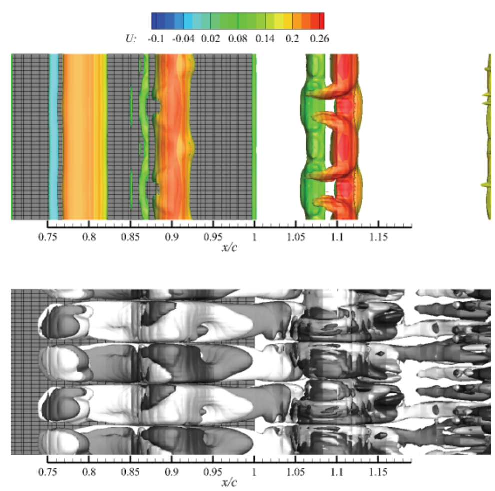

(b)

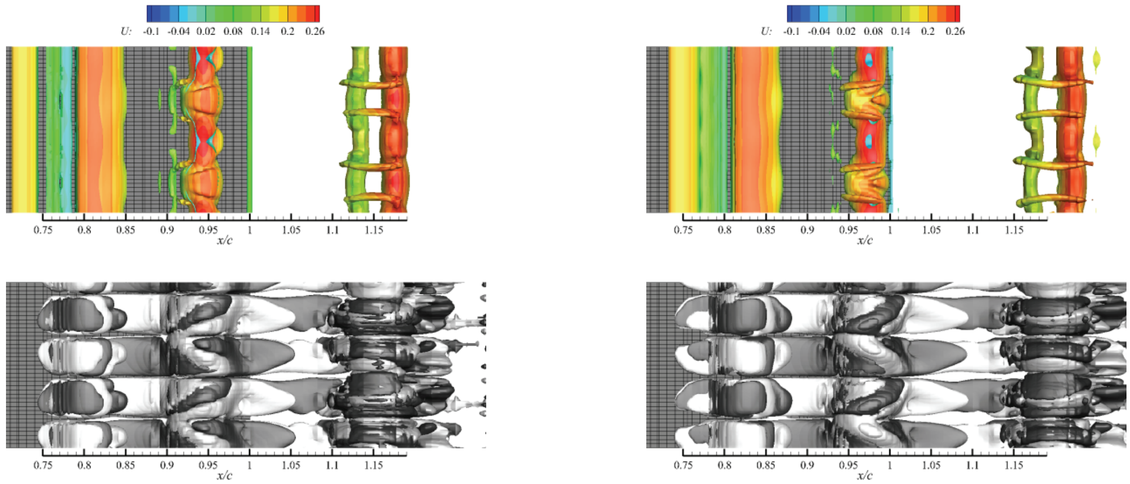

(c) (d)

FIGURE 9. Iso-surface of Q-invariant ($Q = 0.25$, upper) and streamwise vorticity ($\omega_x = \pm 0.25$, lower) for four phases in one shedding period: (a) $\phi = 0$, (b) $\phi = \frac{\pi}{2}$, (c) $\phi = \pi$, (d) $\phi = \frac{3\pi}{2}$

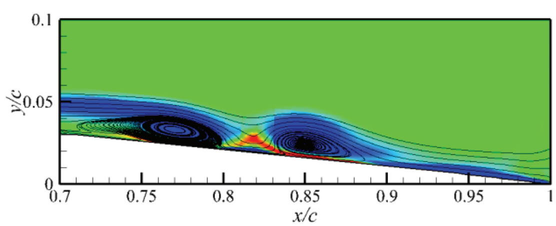

FIGURE 10. Spanwise vorticity and streamlines (side view) at $\phi = 0$.

As shown in figure 9, in the R-S region the oncoming vortex tube is perturbed in an out-of-phase pattern comparing with the previous shedding period. The out-of-phase pattern is a typical feature of the streamwise vortices in elliptic instability (Mode-A) in bluff body-wakes. Williamson (1996) suggested that the out-of-phase symmetry of Model A is due to the elliptical instability of the core and the feedback/self-sustaining mechanism in the reversed flow. The origin of the three dimensional instability of either Mode-A or Mode-B is brought by the reversed flow behind the bluff body due to a feedback mechanism (Williamson 1996). In 3D Case-2, the feedback mechanism is also observed in the reserved flow of the R-S region. Figure 11 shows the contour of the mean streamwise velocity and the side view of ω_x iso-surface at phase $\phi = 0$. In the R-S region $x = (0.75,\ 0.90)$, the streamwise vorticity from the previous vortex tube stay closely attached to the surface (figure 11.b). The reversed flow in the same R-S region (figure 11.a) brings the streamwise vorticities upstream. The next shedding vortex tube coming from upstream interacts with these near wall streamwise vorticities (figure 9). During the interaction between the vortex tube and these streamwise vorticities, the two-dimensional vortex tube first gets affected and new streamwise vorticities is induced and generated on the bottom part of the vortex tube. The whole oncoming vortex tube evolves to a three dimensional one through its own rotation and stretching and propagates downstream. Before leaving the R-S region, it passes the streamwise vorticities to the next vortex tube through the same process. In such a way, the feedback mechanism results in the self-sustaining secondary instability in the R-S region. Figure 12 shows streamwise vorticity contour slice at $x = 0.75$ at phase $\phi = 0$, and two layers of streamwise vorticity can be seen. The near wall vorticity layer is from the previous shedding vortex, and the second vorticity layer is the streamwise vorticities induced on the oncoming shedding vortex. An imprint mechanism occurs: a mirror-image of the previous streamwise vorticities appears on the bottom of the upstream oncoming vortex tube. The induced streamwise vorticities have the opposite signs of the near wall streamwise vorticities. The opposite signs between the original and induced streamwise vorticities explain the out-of-phase pattern observed in 3D Case-2. Based on the above features of the secondary instability occurs in 3D Case-2, the elliptic instability appears to occur in 3D Case-2 and the hyperbolic instability in the braid region is absent.

After leaving the trailing-edge, the perturbed shedding vortices further interact with the vortices from the pressure side of the airfoil, and the generation and stretching of streamwise vortical tube can be found in figure 9. And the features and pattern of the streamwise vortices is more close to the elliptical instability (Mode-A) in bluff body-wakes (Williamson 1996).

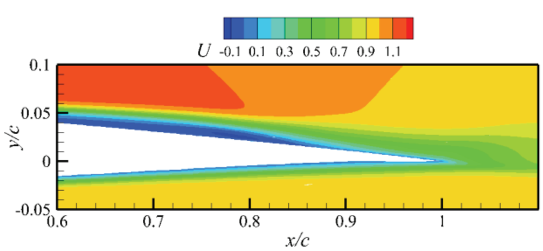

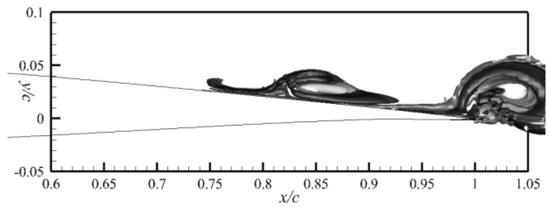

FIGURE 11. 3D Case-2 (a) contour of the mean streamwise velocity and (b) Iso-surface of streamwise vorticity ω_x (side view) at $\phi = 0$.

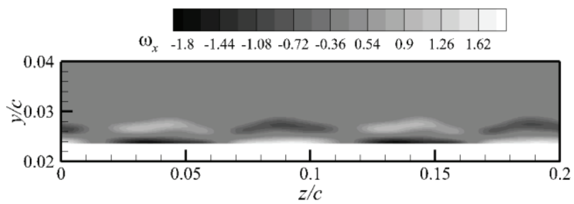

FIGURE 12. Streamwise vorticity contour on $z - y$ plane at $x = 0.775$ at $\phi = 0$.

3.2 The breakdown process of Case-4

In Case-4, the breakdown of the shedding vortices occurs in a different way. Figure 13 shows the instantaneous contours of the side view of spanwise vorticity ω_z for the 2D and 3D simulations in Case-4. As shown in figure 5, the separation and reattachment points move upstream as the AoA increases. The process of separation and reattachment of 2D Case-4 (figure 13.a) is close to those of 2D Case-2 described above and shown in figure 7. The 3D Case-4 (figure 13.b) shows different phenomena from 3D Case-2: small scale three-dimensional structures are generated in the R-S region ($x = (0.55,\ 0.68)$), and a turbulent boundary layer forms after the vortex breakdown (also in figure 3.b).

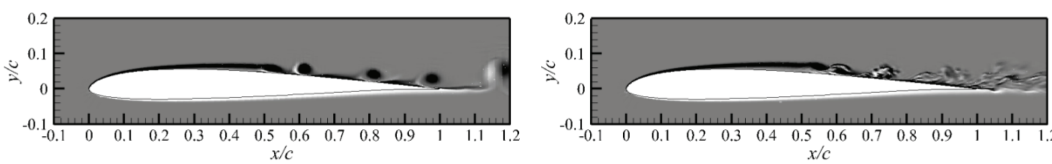

(a) (b)

FIGURE 13. Contour of spanwise vorticity ω_z : (a) 2D Case-4; (b) 3D Case-4.

Four phases within one shedding cycle of the breakdown process in 3D Case-4 is shown in figure 14 by the instantaneous iso-surfaces of Q-invariant $Q = 1$ and streamwise vorticity $\omega_x = \pm 3$. The breakdown of the vortex tube and the generation of the streamwise vorticities can be clearly observed. Braid-like streamwise vorticities appear in the region between two shedding vortices (as shown inside the dash box, figure 14.b), and are then amplified in the interval region and inside the vortex tube (as shown inside the dash box, figure 14.c&d). Figure 15 shows the contours of streamwise velocity and streamwise vorticity at phase $\phi = \pi$ on $x - z$ plane extracted at $y = 0.07$. The high streamwise velocity region corresponds to where the streamwise vorticities are generated in the R-S region (figure 15.a). Braid-like vorticities are generated in an alternative 'peak' and 'valley' pattern as shown in figure 18.b-d, in which a positive one appears next to a negative one (figure 15.b). As shown in figure 15, the flow in the region between two shedding vortices is perturbed at spanwise wavelength $\lambda = 0.025 \sim 0.03$ and the diameter of the vortex core is approximately $D \approx 0.03$ as shown in figure 14, which results in $\lambda/D \approx 1$. The above features of the breakdown process in 3D Case-4 suggests that the dominant secondary instability occurring here is quite close to the instability of two-dimensional hyperbolic streamline (Mode-B) named by Williamson (1998). Hyperbolic instability (Mode-B) involves instability of the braid shear layers (Leweke & Williamson 1998b) which has a spanwise wavelength $\lambda \approx D$. In bluff body wake, the streamwise vorticities are produced and amplified in the braid region and the vortex core deforms uniformly (Williamson 1996). John et al. (2008) first suggested the appearance of the hyperbolic instability in the breakdown process on a NACA-0012 airfoil at $Re_c = 5 \times 10^4$ and incidence $5°$. The vortical structures and wave characters are found quite close to those in John et al. (2008).

Again in Case-4, the secondary instability triggered breakdown is originated in the R-S region and similar to Case-2 the feedback mechanism seems to play the critical role in generating the three dimensional disturbances. Figure 16 shows the contour of the mean streamwise velocity and the side view of ω_x iso-surface at phase $\phi = 0$. Similar to 3D Case-2, the streamwise vorticities from the previous vortex tube stay closely attached to the surface in the R-S region $x = (0.55,\ 0.68)$ (figure 16.b). The reversed flow in the same region (figure 16.a) brings the streamwise vorticities upstream. As shown in the dashed box of figure 14.d, the near wall streamwise vorticities extend in streamwise direction and overlaps with the oncoming shedding vortex. The bottom of the oncoming vortex gets affected by the near wall streamwise vorticities which triggers the secondary instability and breakdown of the oncoming vortex. The circulation in the R-S region provides the necessary condition for the self-sustaining secondary instability.

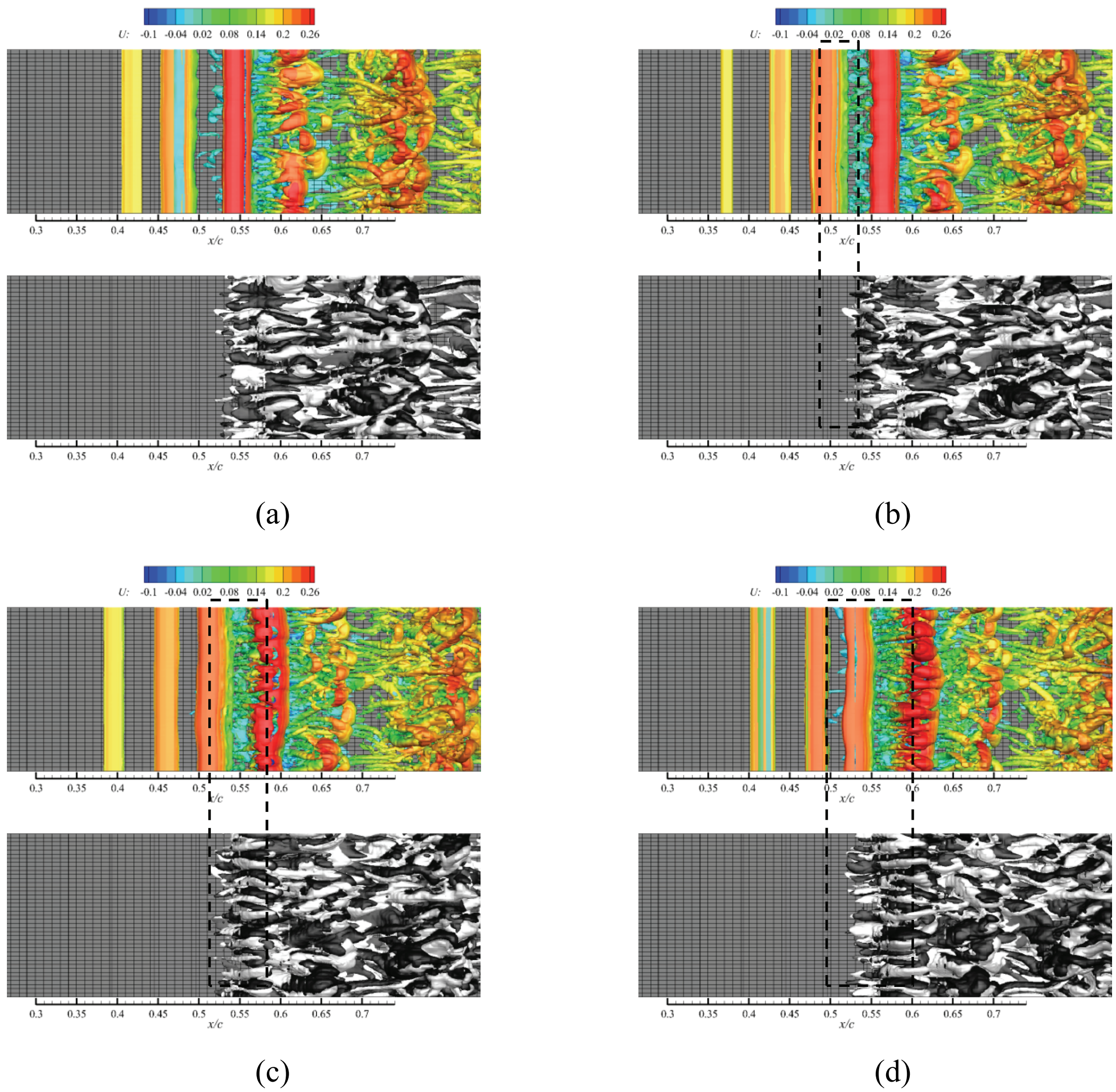

FIGURE 14. Iso-surface of Q-invariant $Q = 1$ (upper) and streamwise vorticity $\omega_x = \pm 3$ (lower) for four phases in one shedding period: (a) $\phi = 0$, (b) $\phi = \frac{\pi}{2}$, (c) $\phi = \pi$, (d) $\phi = \frac{3\pi}{2}$.

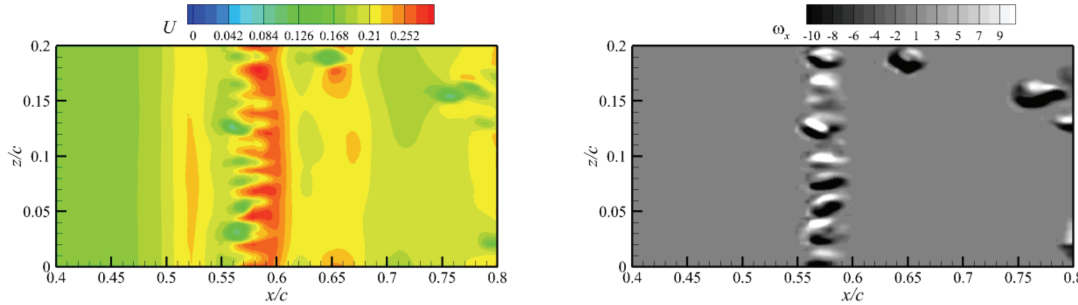

FIGURE 15. Contours of (a) streamwise velocity U and (b) streamwise vorticity ω_x at phase $\phi = \pi$ on $x - z$ slice at y $= 0.07$.

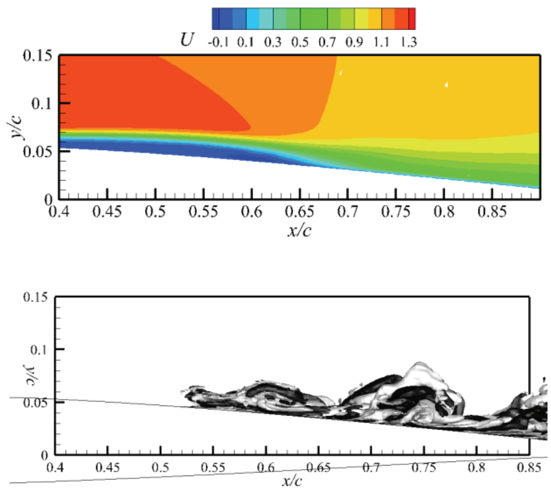

FIGURE 16. 3D Case-4 (a) contour of the mean streamwise velocity and (b) Iso-surface of streamwise vorticity (side view) at $\phi = 0$.

3.3 The breakdown process of Case-6

Figure 17 compares the instantaneous spanwise vorticity ω_z between the 2D and 3D simulations in Case-6. With the increase of AoA, the separation and reattachment points move further upstream for both 2D and 3D simulations. The result of 2D Case-6 shows a similar process as in the previous two 2D cases. Similar to 3D Case-4, small scale structures appear in the R-S region $x = (0.33,\ 0.48)$ in 3D Case-6 and a turbulent boundary layer forms after the turbulent breakdown (also in figure 3.c).

The instantaneous iso-surfaces of Q-invariant $Q = 2$ and streamwise vorticity $\omega_x = \pm 5$ for four phases within the shedding cycle in 3D Case-6 are shown in figure 18. Unlike the previous two cases, the deformation of the shedding vortex and the generation of the streamwise vorticities show an irregular and random pattern. It is neither periodic nor repeatable. As shown in figure 19.b, a layer of small three dimensional structures/eddies inside the circulation region and overlaps with negative mean streamwise velocity (figure 19.a) exists attaching to the wall. The streamwise vorticity layer stays on the wall around $x \approx 0.35$ in the R-S region (figure 18). The oncoming shedding vortex enters the region of near wall streamwise vorticity layer, and the bottom part of the oncoming vortex interact with the three dimensional small scale eddies in the streamwise vortical layer. The breakdown of the oncoming vortex carries out by further interaction with small scale structures and the self-rolling. The feedback mechanism and process is again close to the previous two cases in triggering the self-sustain secondary instability. This type of breakdown is close to the "transition by contact" due to flow reversal proposed by Spalart (2000). In Spalart (2000), the transitional flow instantly becomes three-dimensional without pairing, and no primary Gortler vortices (braid region) are found. A similar type of transition can also be found in Fasel et al. (2004), in which the shedding vortex was found running into the turbulent region.

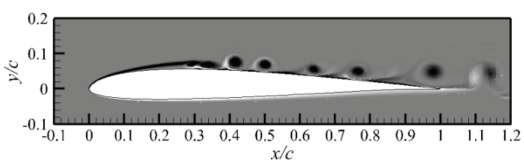

FIGURE 17. Contour of spanwise vorticity ω_z : (a) 2D Case-6; (b) 3D Case-6.

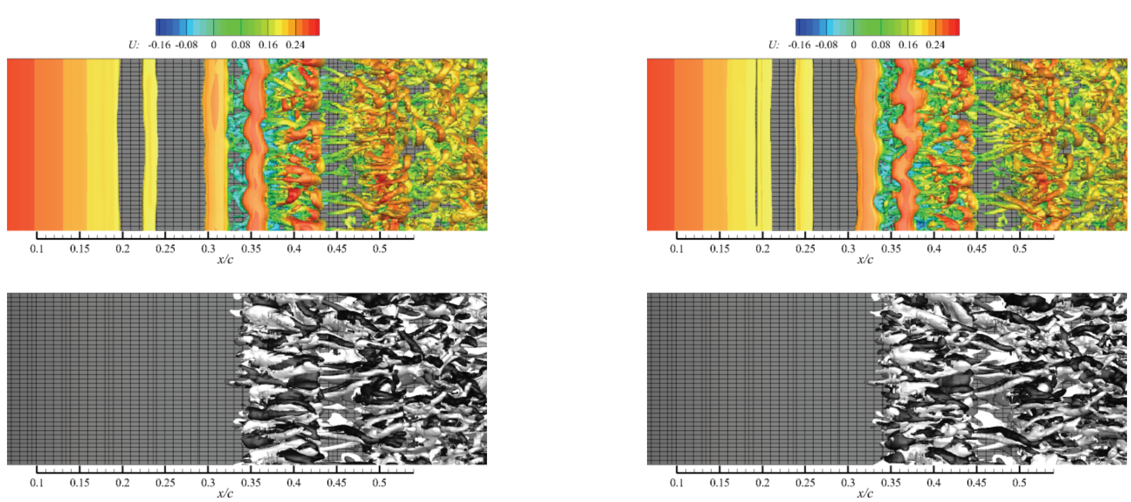

(a) (b)

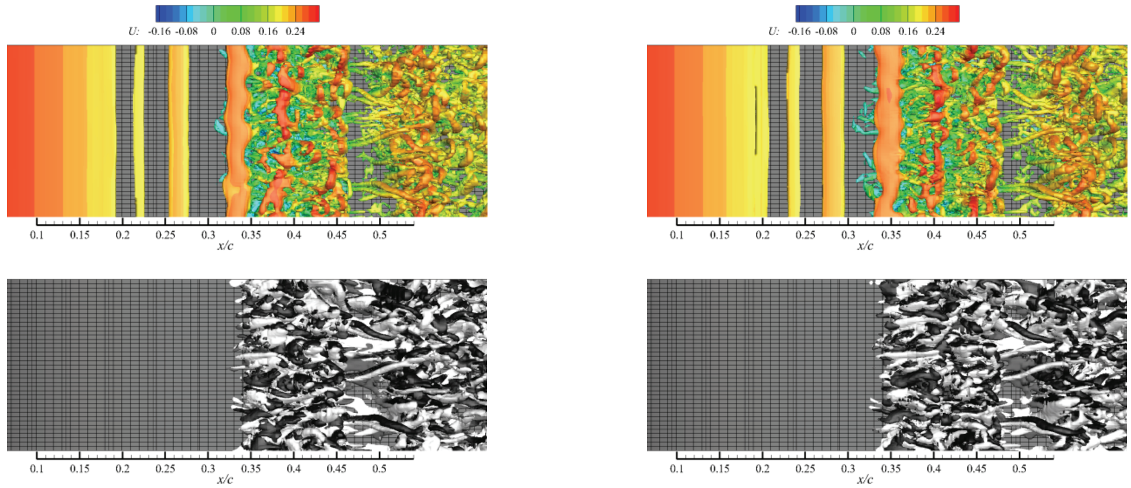

(c) (d)

FIGURE 18. Iso-surface of Q-invariant $Q = 2$ (upper) and streamwise vorticity $\omega_x = \pm 5$ (lower) for four phases in one shedding period: (a) $\phi = 0$, (b) $\phi = \frac{\pi}{2}$, (c) $\phi = \pi$, (d) $\phi = \frac{3\pi}{2}$.

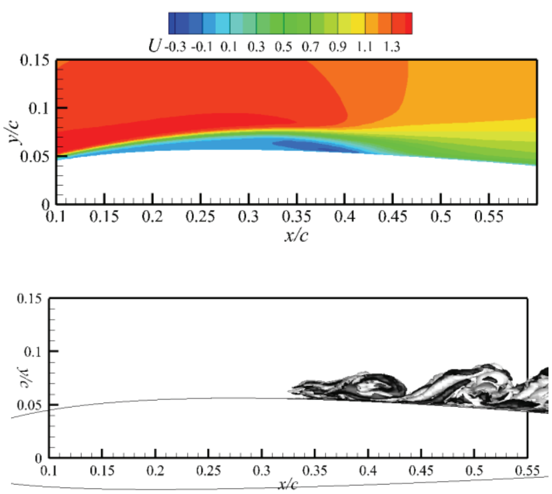

FIGURE 19. 3D Case-6 (a) contour of the mean streamwise velocity and (b) Iso-surface of streamwise vorticity (side view) at $\phi = 0$.

Although the breakdown process shows a random manner, the hyperbolic instability observed in 3D Case-4 is also observed in some intermittent shedding cycle. Figure 20 shows an instantaneous iso-surfaces of Q-invariant and streamwise vorticity in 3D Case-6. The braid-like streamwise vorticities are generated in the region between two shedding vortices and the sign of the streamwise vorticities appears the alternative pattern. However, the elliptical instability observed in 3D Case-2 is not observed in 3D Case-6. In the current case, the breakdown process occurs mainly by contacting with the turbulent flow and appears of an irregular pattern. Thus we call this type of breakdown the contact instability.

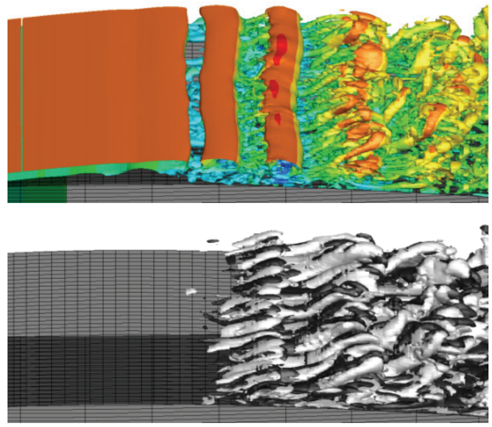

Figure 20. Iso-surface of Q-invariant ($Q = 2$, upper) and streamwise vorticity ($\omega_x = \pm 5$, lower) in 3D Case-6.

4. Discussions

The breakdown process occurs in different pattern at different AoA as described above. However, the feedback mechanism is found in all three cases and plays a critical role in triggering the breakdown process. In Williamson (1996), the reverse flow behind the bluff-body was identified to cause the formation of the self-sustaining elliptical and hyperbolic instabilities due to the feedback mechanism. Here, the circulation of the separated flow on the suction side of the airfoil plays the same role in bringing the three dimensional disturbances upstream and keeping the breakdown process self-sustaining.

Note that in low-Reynolds number airfoil and low-pressure turbine flows with moderate upstreaming disturbances (Fasel et al. 2008, Zhou & Wang 2011 & Zaki et al. 2010), the shedding vortex is more energetic and the R-S region moves upstream. Thus the separation region is reduced and the pressure recoveries smoothly. Although the R-S region is weakened, the feedback mechanism still dominates in triggering the breakdown process. So the feedback process in the R-S region usually occurs when the shedding vortex grows and makes contact with the near wall streamwise vorticities generated in the breakdown of the previous shedding cycle. The growth of the shedding vortices and the approaching to reattach the wall is a necessary condition for the breakdown process, but seems not a sufficient one as the same process occurs in the 2D flows. By keeping increasing upstreaming disturbances, the R-S region can totally avoided and breakdown process occurs convectively (Zaki et al. 2010 and Zhou & Wang 2011). In such a case, the feedback process is avoided due to the absence of the separation.

Table 2 lists the frequency of vortex shedding in all three cases. The frequency increases with the AoA. Figure 21 shows the tangential velocity profiles extracted at the location of the minima of C_f curve in the R-S region (figure 5.a) for the three cases. The velocity outside the boundary layer is higher at higher AoA, and the near wall shearing becomes stronger with the increase of the AoA. The elliptic instability, hyperbolic instability and contact instability appear gradually with the increase of AoA as shown above, in which the sheding frequency and local velocity also increases. A similar sequence of states was also observed in bluff-body wakes with the increase of Reynolds number. In bluff body wakes, the elliptical instability (Mode-A) is first observed at $Re_d > 190$ and the hyperbolic instability (Mode-B) is first observed at $Re_d > 240$ (Williamson 1996). Roshko (1954) found that for $Re = 300 \sim 10{,}000 +$ an 'irregular' regime is observed, where velocity fluctuations showed distinct irregular. A similar region was confirmed by Bloor (1964). With a fixed geometry of bluff body, increasing the Reynolds number by increasing the flow velocity also increases the vortex shedding frequency. Although the feedback process is different between the separated flows on the airfoil suction side and the bluff-body wakes, the sequence of states is analogous between these two types of flows. With the increase of AoA in airfoil flows or with the increase of Reynolds number in bluff-body flows, the scenario of the breakdown occurs: elliptic instability → hyperbolic instability → contact instability. By further increasing the AoA to 8°, the authors carry out another 3D simulation. The breakdown process is found to quite close to 3D Case-6, and the breakdown of the shedding vortex is caused by the contact instability as shown in figure 22.

Table 2. Frequency of vortex shedding

Case	ω
Case-2	22.22
Case-4	36.09
Case-6	60.73

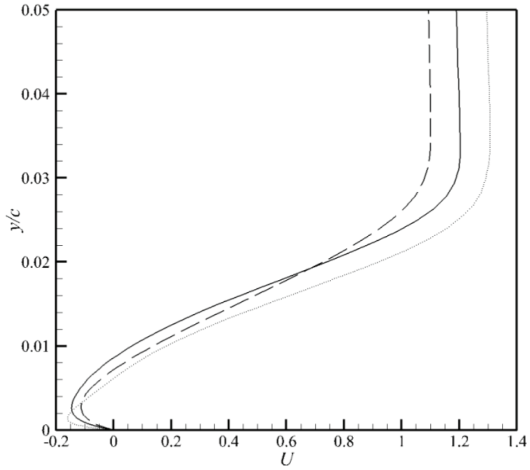

FIGURE 21. Tangential velocity profiles: (dash line) Case-2, (solid line) Case-4, (dot line) Case-6.

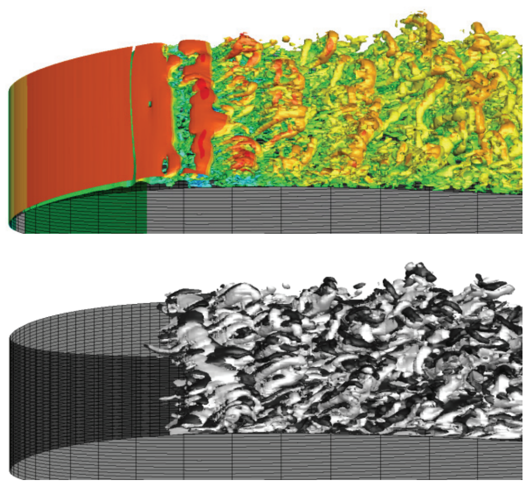

FIGURE 22. Iso-surface of Q-invariant (upper) and streamwise vorticity (lower) at AoA = 8°.

5. Conclusion

The unforced separated and transitional flows over a SD7003 wing at moderate incidences are numerically investigated in this paper. The averaged and statistical results agree well in a p-type grid refinement study. As a new generation numerical method, the SD method with unstructured hexahedral mesh captures the LSB and the transition process well over the suction side of the airfoil.

The breakdown processes associated with the laminar separation bubbles are numerically investigated. The appearances of the separation and pressure gradient make the transition of the LSBs highly non-linear and complicated. In the rear region of the laminar separation bubbles, a Recovery-Separation region with a rapid increase/recovery of the pressure and a strong separation is observed in all cases. The secondary instability is found to originate in the R-S region. And both the $T.K.E.$ and Reynolds stress reach the maximum and concentrate in this region.

It is shown in all three cases that the breakdown process mainly occurs in the Recovery-Separation region and the feedback mechanism due to the flow circulation inside the LSB plays a critical role in passing the three dimensional disturbances from downstream to the upstream which causes the breakdown of the next shedding vortex. The secondary mechanism in the breakdown process appears differently at different AoAs. The oblique modes and Λ-vortex-induced breakdown were not observed in the current unforced LSBs. In Case-2 the breakdown is triggered by the elliptical instability of the vortex core; in Case-4 the hyperbolic instability dominates in the breakdown process; and in Case-6 the breakdown is caused by the direct contact and interaction with circulated turbulent flow which shows an irregular pattern. With the increase of AoA in current cases, the sequence of states is analogous to the sequence of breakdown states observed in bluff-body wakes with the increase of the Reynolds number, which follows the scenario: elliptic instability → hyperbolic instability → contact instability.

Acknowledgments

The authors would like to acknowledge the support from the Air Force Office of Scientific Research and the Department of Aerospace Engineering, Iowa State University.

Reference

[1] ALAM, M. & SANDHAM, N. D. 2000 Direct numerical simulation of ‘short’ laminar separation bubbles with turbulent reattachment. J. Fluid Mech. 410, 1–28.

[2] BLOOR, M. S. 1964 The transition to turbulence in the wake of a circular cylinder. J. Fluid. Mech. 19, 290.

[3] DENG, S., JIANG, L. & LIU, C. 2007 DNS for flow separation control around an airfoil by pulsed jets. Comp. Fluids 36 (6), 1040–1060.

[4] DUBEIF, Y. & DELCAYRE, F. 2000 On Coherent-vortex Identification in Turbulence, Journal of Turbulence, Vol. 1, No. 11, 2000, pp. 1-22.

[5] DESQUESNES, G., TERRACOL, M. & SAGAUT, P. 2007 Numerical investigation of the tone noise mechanism over laminar airfoils. J. Fluid Mech. 591, 155–182.

[6] DRAZIN, P. G. 2002 Introduction to hydrodynamic stability. Cambridge University Press, ISBN 0 521 00965 0.

[7] FASEL, H. F. & POSTL, D. 2004 Interaction of separation and transition in boundary layers: direct numerical simulations. Sixth IUTAM Symposium on Laminar-Turbulent Transition. Invited lectures, 71-88.

[8] H. F. FASEL, W. BALZER and A. GROSS. 2008 Investigation of separation control for low-pressure turbines using cfd. 26TH INTERNATIONAL CONGRESS OF THE AERONAUTICAL SCIENCES.

[9] GASTER, M. 1963 On stability of parallel flows and the behaviour of separation bubbles. PhD Dissertation, University of London.

[10] GASTER, M. 1967 The structure and behaviour of separation bubbles. Aero. Res. Counc. R&M 3595. Aerodynamics Division NPL.

[11] GOLDSTEIN, M. E. 1983 The evolution of Tollmien–Schlichting waves near a leading edge. J. Fluid Mech. 127, 59–81.

[12] HAIN, R., KAHLER, C. J. & RADESPIEL, R. 2009 Dynamics of laminar separation bubbles at low-Reynolds-number aerofoils. J. Fluid Mech. 630, 129–153.

[13] HAMMOND, D. A. & REDEKOPP, L. G. 1998 Local and global instability properties of separation bubbles. Eur. J. Mech. B/Fluids 17, 145–164.

[14] HANNEMANN, K. & OERTEL, H. 1989 Numerical simulation of the absolutely and convectively unstable wake. J. Fluid Mech. 199, 55–88.

[15] HORTON, H. P. 1968 Laminar separation in two and three-dimensional incompressible flow. PhD Dissertation, University of London.

[16] HORTON, H. P. 1969 A semi-empirical theory for the growth and bursting of laminar separation bubbles. Aero. Res. Counc. Current Paper 1073.

[17] H. HU & Z. YANG, “An Experimental Study of the Laminar Flow Separation on a Low Reynolds Number Airfoil”, ASME Journal of Fluid Engineering, Vol.130, No.5, 051101, 2008.

[18] HU, S. & ZHONG, X. L. 1998 Linear stability of viscous supersonic plane Couette flow, Phys. Fluids 10, 709 (1998).

[19] HUERRE, P. & MONKEWITZ, P. A. 1985 Absolute and convective instabilities in free shear layers. J. Fluid Mech. 159, 151–168.

[20] JACOBS, R. & DURBIN, P. A. 2001 Simulations of Bypass Transition, J. Fluid Mech., 428 , 185-212.

[21] JAMESON A., 2009, A Proof of the stability of the spectral difference method for all orders of accuracy, ACL Report no. 2009-1, Stanford University, March.

[22] JONES, L. E., SANDBERG, R. S. & SANDHAM, N. D 2008 Direct numerical simulations of forced and unforced separation bubbles on an airfoil at incidence. J. Fluid Mech. 602, 175–207.

[23] JONES, L. E., SANDBERG, R. S. & SANDHAM, N. D 2010 Stability and receptivity characteristics of a laminar separation bubble on an aerofoil. J. Fluid Mech. 648, 257–296.

[24] LAM, S. H. & ROTT, N. 1960 Theory of Linearized Time-Dependent Boundary Layers. Graduate School of Aeronautical Engineering, Cornell University.

[25] LANG, M., RIST, U. & WAGNER, S. 2004 Investigations on controlled transition development in a laminar separation bubble by means of LDA and PIV. Exp. Fluids 36, 43–52.

[26] LEWEKE, T. & WILLIAMSON, C. H. K. 1998 Three-dimensional instabilities in wake transition. Eur. J. Mech. B/Fluids 17, 571–586.

[27] MALIK, M. R. 1990 Numerical methods for hypersonic boundary layer stability, Journal of Computational Physics 86, 376-413.

[28] MARQUILLIE, M. & EHRENSTEIN, U. W. E. 2003 On the onset of nonlinear oscillations in a separating boundary-layer flow. J. Fluid Mech. 490, 169–188.

[29] MARXEN, O., LANG, M., RIST, U. & WAGNER, S. 2003 A combined experimental/numerical study of unsteady phenomena in a laminar separation bubble. Flow, Turbulence Combust. 71, 133–146.

[30] MARXEN, O., RIST, U. & WAGNER, S. 2004 The effect of spanwise-modulated disturbances on transition in a 2-D separated boundary layer. AIAA 42, 937–944.

[31] MCALPINE, A., NASH, E. C. & LOWSON, M. V. 1999 On the generation of discrete frequency tones by the flow around an airfoil. J. Sound Vib. 222 (5), 753–779.

[32] McAuliffe, B. R. & Yaras, M. I. 2010 Transition Mechanisms in Separation Bubbles Under Low and Elevated Freestream Turbulence. Journal of Turbomachinery. Vol. 132 / 011004-1.

[33] MORKOVIN, M., RESHOTKO, E. & HERBERT, T. 1994 Transition in open flow systems – a reassessment. Bull. Am. Phys. Soc. 39 (9), 1882.

[34] MOSER, M. M. and ROGERS, R. D. 1991 Mixing transition and the cascade to small scales in a plane mixing layer, Phys. Fluids A 3 (1991), pp. 1128–1134

[35] Ovchinnikov, V. Choudhari, M. M. and Piomelli, U. 2008 Numerical simulations of boundary-layer bypass transition due to high-amplitude free-stream turbulence Journal of Fluid Mechnanics, vol. 613, p.135-169

[36] OWEN, P. R. & KLANFER, L. 1953 On the laminar boundary layer separation from the leading edge of a thin aerofoil. ARC Conf. Proc. 220.

[37] PAULEY, L. L., MOIN, P. & REYNOLDS, W. C. 1990 The structure of two-dimensional separation. J. Fluid Mech. 220, 397-411.

[38] PAULEY, L. L. 1994 Response of two-dimensional separation to three-dimensional disturbances. Trans. ASME: J. Fluids Engng 116, 433–438.

[39] P. RICCO & X. WU. Response of a compressible laminar boundary layer to free-stream vortical disturbances. J. Fluid Mech., 587:97–138, 2007.

[40] RIST, U. 1994 Nonlinear effects of 2D and 3D disturbances on laminar separation bubbles. Proc. IUTAM Symp. on Nonlinear Instability of Nonparallel Flows, pp. 324–333. Springer.

[41] RIST, U. & MAUCHER, U. 2002 Investigations of time-growing instabilities in laminar separation bubbles. Eur. J. Mech. B/Fluids 21, 495–509.

[42] ROE, P. L. 1981 Approximate Riemann solvers, parameter vectors, and difference schemes, J. Comput. Phys. 43 (1981) 357-372.

[43] ROSHKO, A. 1954 On the development of turbulent wakes from vortex streets. NACA Rep. 1191.

[44] ROSSITER, J. E. 1964 Wind-tunnel experiments on the flow over rectangular cavities at subsonic and transonic speeds. Aeronaut. Res. Counc. Rep. Memo 3838.

[45] SPALART, P. R. & STRELETS, M. K. H. 2000 Mechanisms of transition and heat transfer in a separation bubble. J. Fluid Mech. 403, 329–349.

[46] SUN, Y., WANG, Z.J., LIU, Y. 2007 High-Order Multidomain Spectral Difference Method for the Navier-Stokes Equations on Unstructured Hexahedral Grids, Communications in Computational Physics, Vol. 2, No. 2(2007) 310-333.

[47] THOMPSON, M. C., LEWEKE, T. & WILLIAMSON, C. H. K. 2001 The physical mechanism of transition in bluff body wakes. J. Fluids Struct. 15, 607–616.

[48] WATMUFF, J. H. 1999 Evolution of a wave packet into vortex loops in a laminar separation bubble. J. Fluid Mech. 397, 119–169.

[49] WILLIAMSON, C. H. K. 1996 Three-dimensional wake transition. J. Fluid Mech. 328, 345–407.

[50] YANG, Z. & VOKE, P.R. 2001 Large-eddy simulation of boundary-layer separation and transition at a change of surface curvature. J. Fluid. Mech. 439, 305-333

[51] YARUSEVYCH, S., SULLIVAN, P.E. & KAWALL, J.G. 2009 On vortex shedding from an airfoil in low-Reynolds-number flows. J. Fluid. Mech. 632, 245-271

[52] ZHOU, Y. & WANG, Z. J. 2010 Implicit Large Eddy Simulation of Transitional Flow over a SD7003 Wing Using High-order Spectral Difference Method, AIAA-2010-4442

[53] ZHOU, Y. & WANG, Z. J. 2010 Absorbing Boundary Conditions for the Euler and Navier-Stokes Equations with the Spectral Difference Method, Journal of Computational Physics 229, 8733-8749

CHAPTER 5. Effects of Surface Roughness on Laminar Separation Bubble over a Wing at a Low-Reynolds Number

A paper submitted to AIAA Journal (in revision process)

Ying Zhou and Z.J. Wang

Abstract

Laminar separation bubbles (LSBs) are often found over the wing of micro air vehicles (MAV) at low Reynolds numbers, and strongly influence the lift, drag and other aerodynamic performance parameters. A numerical investigation of passive LSB control techniques using roughness bumps on a low-Reynolds number wing is conducted in the present study. A high-order spectral difference unstructured grid Navier-Stokes solver is employed in the simulations. The study of surface roughness on laminar separation and turbulent transition can provide insights into the design of future passive control devices on wings. The transitional flow with LSB past a SD7003 rectangular wing with Reynolds number of 60,000 is used as the baseline (uncontrolled) case. In the controlled cases, roughness bumps are strategically placed near the leading edge of the wing for the purpose of improving aerodynamic performance in terms of the lift to drag ratio. The location, bump size, the number of bumps and the angle-of-attack are varied to study the effects. The pressure drag forces in the controlled cases are found to be reduced significantly when the LSB are reduced or avoided, resulting in much improved lift over drag ratio.

Nomenclature

AoA = angle of attack

α_r = wave number of the disturbances in x direction in linear stability theory

α_i = growth rate of the disturbances in linear stability theory

β = wave number of the disturbances in z direction in linear stability theory

C_p = pressure coefficient

C_f = skin friction coefficient

C_D = drag coefficient

C_{Df} = drag coefficient contributed by friction

C_{Dp} = drag coefficient contributed by pressure

C_L = lift coefficient

c = chord length

$F, G, H, \tilde{F}, \tilde{G}, \tilde{H}$ = vector of fluxes in Cartesian coordiantes and standard unstructured elements

$\tilde{F}^i, \tilde{F}^v$= inviscid and viscous vector of fluxes in standard unstructured elements

$h_i, l_{i+1/2}$ = coefficient of Lagrange polynomial interpolation at solution points and flux points

H_{EF}, L_{BD}, W_{AC} = height, length and width the of the roughness bump

i, j, k = index of coordinates in x, y, z direction

J = Jacobian matrix

K = number of points in physical element

L/D = lift-to-drag ratio

M = Mach number

M_i = shape function in coordinate transformation

N_{bump} = number of roughness bumps

p = nondimensional pressure

P_{Total} = normalized mean total pressure, $\left(\frac{1}{2}\rho U^2 + P\right)/\frac{1}{2}\rho_\infty U_\infty^2$

$|\nabla P|$ = magnitude of pressure gradient

$Q, \tilde{Q}$ = vector of conservative variables in Cartesian coordiantes and standard unstructured elements

Q_L, Q_R = vector of conservative variables from the two elements beside the interface

Re_c = Reynolds number based on chord length

ρ = nondimensional density

s = wave speed of the disturbance in linear stability theory, $s = \omega/\alpha_r$

t = nondimensional time $t = t^*/(c/U_\infty)$

t^* = dimensional time

T = nondimensional temperature

T. K. E. = normalized turbulent kinetic energy, $\frac{1}{2}\left(\overline{u'^2} + \overline{v'^2} + \overline{w'^2}\right)/U_\infty^2$

δ_E = boundary layer thickness at the location of bump in uncontrolled case

u, v, w = nondimensional velocity in x, y, z direction

U_∞ = freestream velocity

u', v', w' = nondimensional velocity fluctuation in x, y, z direction

u_t, u_t' = nondimensional tangential velocity / fluctuation, normal to the wall surface

x, y, z = nondimensional Cartesian coordinates

$\xi_x, \eta_x, \varsigma_x, \xi_y, \eta_y, \varsigma_y, \xi_z, \eta_z, \varsigma_z$ = metric coefficients of the coordinate transformation

ω = frequency of the disturbances in linear stability theory

X_s = solution points in spectral difference method

$X_{s+1/2}$ = flux points in spectral difference method

X_E = location of the roughness bump

τ_{xy} = normalized Reynolds stress, $\overline{u'v'}/U_\infty^2$

∇Q = gradient of conservative variables

$\Delta x^+, \Delta y^+, \Delta z^+$ = cell size in wall units

ϕ = vector of primitive variables

Ω = computational spatial domain

1. Introduction

Flow control, the technique to manipulate a flow field to achieve a desired change, is of immense technological importance, and thus is pursued by many scientists and engineers in various areas of fluid mechanics field for many years. The configuration lift, drag and L/D ratio are the principal considerations in the design and construction of air vehicles. The decrease in drag and increase in L/D ratio can increase the range and reduce the required thrust, which result in improved fuel economy. Low-Reynolds number ($Re_c = 10^4 \sim 10^5$) flow has been of interest for many decades with the development of Micro Air Vehicles (MAV). In the low-Reynolds number flows over airfoils, the formation of a LSB has a dominant effect on the flow field and usually causes high pressure drag force on the airfoil. Reducing or avoiding the LSB on the surfaces of the airfoils is one way of achieving reduced drag. Because of this, aerodynamicists and aircraft designers have pursued the objective of separation control for many decades.

Since laminar boundary layers are less resistible to the significant adverse pressure gradient, LSBs are widely found over the suction side of low-Reynolds-number airfoils at moderate incidences. At moderate AoAs, the laminar flow detaches from the suction wing surface near the leading edge and a LSB is formed. After separation, vortex shedding due to the Kelvin-Helmholtz (K-H) instability is usually observed within the LSB region. Thereafter, the separated laminar boundary layer rapidly transitions to turbulent flows and the turbulent boundary layer reattaches after the vortex breakdown.

Active flow control techniques have been widely adopted for the separation and transition control of flow over airfoils. Periodic air suction/blowing through a slot on the airfoil surface, which introduces momentum into the flow field, might be the most popular means of active control. With properly chosen frequency and magnitude of the suction/blowing speed, the technique is often found to be effective in reducing the separation region and improving performance. Plasma actuators are applied as another technique of active flow control. However, active control techniques such as suction/blowing usually require additional devices and power, and is less applicable to the separation control over a MAV wing, which should be light and small. The passive means of flow control involves 'inert' devices including changes to the wing shape and surface finish. By introducing the surface roughness, the laminar boundary layers can be perturbed or become turbulent, and thus are more resistible to the adverse pressure gradient. In such a way, the separation can be delayed or avoided.

Surface roughness has been adopted as a method of altering the flow pattern in various types of flows. Saric et al. [1, 2] used surface roughness as a means of passive flow control in experimental studies of transition flow over swept wings. White and Saric [3] examined roughness effects on transition and found that three-dimensional static roughness can be an effective tool in delaying the transition to turbulence on a swept wing by distributing roughness elements at a spacing approximately equal to one-half of the spanwise wavelength of the critical mode. Carpenter el al. [4, 5] continued the work of Saric et al. [1] and found that the flow is very sensitive to both the shape and height of the discrete roughness elements. In the experimental study of unsteady and transitional flows behind roughness elements in Ergin and White [6], it is found that with the increase of roughness height, the initial amplitudes of the steady disturbances and the growth rates of the unsteady disturbances increase. The surface roughness was also applied in altering the supersonic flows, e.g. [7], [8]. At Mach 2.8 Latin and Bowersox [8] found as the roughness height was increased, the turbulence production relative to the frictional losses increased. Fransson et al. [9, 10] applied roughness elements on a flat plate in a wind-tunnel and found that this passive control technique can delay transition to turbulence. Zhang et al. [11] experimentally investigated the performance degradation of a low-Reynolds number airfoil with distributed leading edge roughness and found that the roughness height appears to be a more critical factor for roughness induced performance degradation than other factors such as distribution patterns. Honsaker and Huebsch [12] used a Prandtl transposition to model the surface roughness on airfoils and found that the dynamic surface roughness is effective on the stall separation control. Rizzetta and Visbal [13] employed a high-order overset-grid approach to model cylindrical roughness elements and studied the flow past an array of distributed roughness elements. More recently, Rizzetta et al. [14] performed a direct numerical simulation of discrete roughness on a swept-wing leading edge and studied the stability of crossflow with roughness. Redford et al. [15] studied the compressibility effects on boundary-layer transition induced by an isolated roughness element and suggested that the boundary layer near the roughness element is particularly receptive to external disturbances.

Surface roughness is also applied in controlling flow separation. Santhanakrishnan and Jacob [16] investigated the separation behavior with "large-scale" roughnesses on an airfoil surface and showed that the separation is delayed and the separation region is smaller for the perturbed airfoil case at moderate Re and higher angle of attack. Boiko et al. [17] experimentally applied surface humps for the control of laminar separated flows and suggested that the injection of stationary disturbances in the separation region followed by their transient amplification is a promising way of flow control. It was found that with a suitable size of the roughness elements placed close to separation line and span-wise spacing between them, it is possible to generate streamwise stationary disturbances subject to transient growth accompanied by secondary instability to unsteady disturbances promoting laminar flow breakdown.

High-order methods on unstructured grids are known for their advantages of accuracy and flexibility in the numerical simulation of multi-scale flow with complex geometries. In the last two decades, there have been intensive research efforts on high-order methods for unstructured grids [18-30]. In this paper, a high-order SD method for the three dimensional Navier-Stokes equations on unstructured hexahedral grids developed by Sun et al. [30] is used. This approach is capable of capturing the laminar separation and the vortex breakdown, and has been previously shown in the numerical simulation of the attached/detached laminar flow and the reattached turbulent flow in the case of the uncontrolled baseline model [31].

In this paper, a passive flow control technique using surface roughness (bumps) near the leading-edge of the wing is numerically studied. The roughness bumps can affect the formation of the LSBs and be used for the purpose of aerodynamic performance improvement. The flow over a SD7003 wing at $\mathrm{AoA} = 4$ deg, $\mathrm{Re_c} = 6 \times 10^4$ and $\mathrm{M} = 0.2$ is used as the baseline model and the starting point for the controlled models. The rest of the paper is organized as follows. In the next section, the spectral difference method on unstructured hexahedral mesh is briefly reviewed. In Section III, numerical results of the baseline model are presented and the flow features associated with LSBs are discussed. In Section IV, a series of cases with different bump size, bump number and AoAs are numerical simulated. The numerical results of the controlled cases are compared with those of the baseline model and the detail effects of the surface roughness are investigated. Concluding remarks are given in Section V.

2. Review of Multidomain Spectral Difference (SD) Method

Governing equations

Consider the three-dimensional compressible non-linear Navier-Stokes equations written in the conservation form as

$$\frac{\partial \mathrm{Q}}{\partial \mathrm{t}} + \frac{\partial \mathrm{F}}{\partial \mathrm{x}} + \frac{\partial \mathrm{G}}{\partial \mathrm{y}} + \frac{\partial \mathrm{H}}{\partial \mathrm{z}} = 0 \tag{1a}$$

on domain $\Omega \times [0, \mathrm{T_0}]$ and $\Omega \subset \mathrm{R}^3$ with the initial condition

$$\mathrm{Q}(\mathrm{x}, \mathrm{y}, \mathrm{z}, 0) = \mathrm{Q_0}(\mathrm{x}, \mathrm{y}, \mathrm{z}) \tag{1b}$$

and appropriate boundary conditions on $\partial\Omega$.

Coordinate transformation

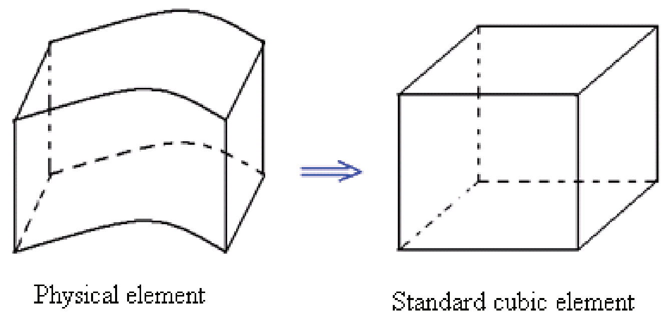

Figure 1 Transformation from a physical element to a standard element

In the SD method, it is assumed that the computational domain is divided into non-overlapping unstructured hexahedral cells or elements. In order to handle curved boundaries, both linear and quadratic isoparametric elements are employed, with linear elements used in the interior domain and quadratic elements used near high-order curved boundaries. In order to achieve an efficient implementation, all physical elements (x, y, z) are transformed into standard cubic element $(\xi, \eta, \varsigma) \in [-1,1] \times [-1,1] \times [-1,1]$ as shown in Figure 1.

The transformation can be written as

$$\begin{bmatrix} x \\ y \\ z \end{bmatrix} = \sum_{i=1}^{K} M_i(\xi, \eta, \varsigma) \begin{bmatrix} x_i \\ y_i \\ z_i \end{bmatrix} \tag{2}$$

For the transformation given in (2), the Jacobian matrix J takes the following form

$$J = \frac{\partial(x,y,z)}{\partial(\xi,\eta,\varsigma)} = \begin{bmatrix} x_\xi & x_\eta & x_\varsigma \\ y_\xi & y_\eta & y_\varsigma \\ z_\xi & z_\eta & z_\varsigma \end{bmatrix}.$$

The governing equations in the physical domain are then transformed into the standard element, and the transformed equations take the following form

$$\frac{\partial \tilde{Q}}{\partial t} + \frac{\partial \tilde{F}}{\partial \xi} + \frac{\partial \tilde{G}}{\partial \eta} + \frac{\partial \tilde{H}}{\partial \varsigma} = 0 \tag{3}$$

where

$$\tilde{Q} = |J| \cdot Q$$

$$\begin{bmatrix} \tilde{F} \\ \tilde{G} \\ \tilde{H} \end{bmatrix} = |J| \begin{bmatrix} \xi_x & \xi_y & \xi_z \\ \eta_x & \eta_y & \eta_z \\ \varsigma_x & \varsigma_y & \varsigma_z \end{bmatrix} \cdot \begin{bmatrix} F \\ G \\ H \end{bmatrix}$$

Spatial Discretization

In the standard element, two sets of points are defined, namely the solution points and the flux points, illustrated in Figure 2 for a 2D element. The solution unknowns (Q) or degrees-of-freedoms (DOFs) are stored at the solution points, while fluxes are computed at the flux points. The solution points in 1D are chosen to be the Gauss points defined by

$$X_s = \cos\left(\frac{2s-1}{2N} \cdot \pi\right), s = 1,2,\cdots,N. \tag{4}$$

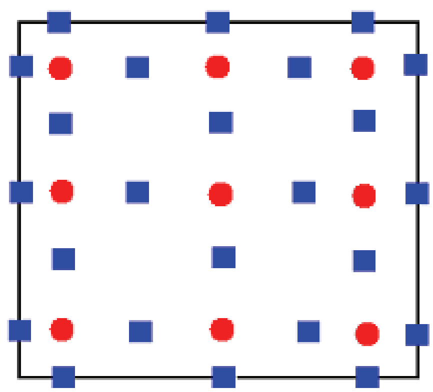

Figure 2 Distribution of solution points (circles) and flux points (squares) in a standard element for a 3rd-order SD scheme.

With solutions at N points, we can construct a degree $(N-1)$ polynomial in each coordinate direction using the following Lagrange basis defined as

$$h_i(X) = \prod_{s=1,s\neq i}^{N} \left(\frac{X - X_s}{X_i - X_s}\right) \tag{5}$$

The reconstructed solution for the conserved variables in the standard element is just the tensor products of the three one-dimensional polynomials, i.e.

$$Q(\xi,\eta,\varsigma) = \sum_{k=1}^{N}\sum_{j=1}^{N}\sum_{i=1}^{N} \frac{\tilde{Q}_{i,j,k}}{|J_{i,j,k}|} h_i(\xi) \cdot h_j(\eta) \cdot h_k(\varsigma) \tag{6}$$

The flux points in 1D are chosen to be the $(N-1)$ Gauss quadrature points plus the two ending points. With fluxes at $(N+1)$ points, a degree N polynomial can be constructed in each coordinate direction using the following Lagrange bases defined as

$$l_{i+1/2}(X) = \prod_{s=0,s\neq i}^{N} \left(\frac{X - X_{s+1/2}}{X_{i+1/2} - X_{s+1/2}} \right) \tag{7}$$

Similarly, the reconstructed flux polynomials take the following form:

$$\tilde{F}(\xi,\eta,\varsigma) = \sum_{k=1}^{N}\sum_{j=1}^{N}\sum_{i=0}^{N} \tilde{F}_{i+1/2,j,k}\, l_{i+1/2}(\xi)\cdot h_j(\eta)\cdot h_k(\varsigma) \tag{8a}$$

$$\tilde{G}(\xi,\eta,\varsigma) = \sum_{k=1}^{N}\sum_{j=0}^{N}\sum_{i=1}^{N} \tilde{G}_{i,j+1/2,k}\, h_i(\xi)\cdot l_{j+1/2}(\eta)\cdot h_k(\varsigma) \tag{8b}$$

$$\tilde{H}(\xi,\eta,\varsigma) = \sum_{k=0}^{N}\sum_{j=1}^{N}\sum_{i=1}^{N} \tilde{H}_{i,j,k+1/2}\, h_i(\xi)\cdot h_j(\eta)\cdot l_{k+1/2}(\varsigma) \tag{8c}$$

Algorithm

Because the SD method is based on the differential form of the governing equations, the implementation is straightforward even for high-order curved boundaries. All the operations are basically one-dimensional in each coordinate direction and each coordinate direction shares the collocated solution points with others, resulting in improved efficiency. In summary, the algorithm to compute the inviscid flux and viscous flux and update the unknowns (DOFs) consists the following steps:

1. Given the conserved variables $\{Q_{i,j,k}\}$ at the solution points, compute the conserved variables $\{Q_{i+1/2,j,k}\}$ at the flux points using polynomial (6).

   Note that inviscid flux is a function of the conserved solution and the viscous flux is a function of both the conserved solution and its gradient, taking flux $\tilde{F}$ for example:

$$\begin{cases} \tilde{F} = \tilde{F}^i - \tilde{F}^v \\ \tilde{F}^i_{i+1/2,j,k} = \tilde{F}^i\left(Q_{i+1/2,j,k}\right) \\ \tilde{F}^v_{i+1/2,j,k} = \tilde{F}^v\left(Q_{i+1/2,j,k}, \nabla Q_{i+1/2,j,k}\right) \end{cases} \tag{9}$$

2. Compute the inviscid fluxes $\{\tilde{F}^{i}_{i+1/2,j,k}\}$ at the interior flux points using the solution $\{Q_{i+1/2,j,k}\}$ computed at Step 1. Compute the viscous fluxes $\{\tilde{F}^{v}_{i+1/2,j,k}\}$ using the solution $\{Q_{i+1/2,j,k}\}$ computed at Step 1 and the gradient of the solutions $\{\nabla Q_{i+1/2,j,k}\}$ computed based on $\{Q_{i+1/2,j,k}\}$.

3. Compute the common inviscid flux at element interfaces using a Riemann solver (10), such as the Roe solver [32] and Russanov solver [30].

$$\tilde{F}^{i} = \tilde{F}^{i}(Q_L, Q_R) \tag{10}$$

Compute the common viscous flux at element interfaces using a viscous approach (11), such as the averaged approach and DG-like approach [30].

$$\tilde{F}^{v} = \tilde{F}^{v}(Q_L, Q_R, \nabla Q_L, \nabla Q_R) \tag{11}$$

Then compute the derivatives of the fluxes at all the solution points by using (12).

$$\left(\frac{\partial \tilde{F}}{\partial \xi}\right)_{i,j,k} = \sum_{r=0}^{N} \tilde{F}_{r+1/2,j,k}\, l'_{r+1/2}(\xi_i) \tag{12a}$$

$$\left(\frac{\partial \tilde{G}}{\partial \eta}\right)_{i,j,k} = \sum_{r=0}^{N} \tilde{G}_{i,r+1/2,k}\, l'_{r+1/2}(\eta_j) \tag{12b}$$

$$\left(\frac{\partial \tilde{H}}{\partial \varsigma}\right)_{i,j,k} = \sum_{r=0}^{N} \tilde{H}_{i,j,r+1/2}\, l'_{r+1/2}(\varsigma_k) \tag{12c}$$

4. Update the DOFs using a multistage TVD scheme for time integration of (13).

$$\frac{\partial \tilde{Q}_{i,j,k}}{\partial t} = -\left(\frac{\partial \tilde{F}}{\partial \xi} + \frac{\partial \tilde{G}}{\partial \eta} + \frac{\partial \tilde{H}}{\partial \varsigma}\right)_{i,j,k} \tag{13}$$

For more details about SD method on hexahedral mesh, the readers can refer to [30].

3. Baseline model

The flow over the SD7003 wing at $AoA = 4\ deg$, Reynolds number $Re_c = 6 \times 10^4$ and Mach number $M = 0.2$ without surface roughness is used as the baseline model. This case is chosen due to the variety of previously experimental and numerical results [33]. The baseline model is numerically simulated first and then the results are used to compare with and assess the performance of the controlled models in the next section. The computational grid and boundary conditions are introduced below, and a p-type grid resolution study is carried out. The statistical numerical results are presented. Then the features associated with the LSBs and the mechanisms of turbulent transition are discussed.

In this paper, the Reynolds number and Mach number are fixed for all the cases. The cases with different geometry and parameters are named according to the AoA, w/ or w/o bumps and the additional bump parameters, e.g. 'AoA_4c' represents the controlled case at $AoA = 4\ deg$ and 'AoA_4' refers to the current case of the baseline model.

a. Computational grid and boundary conditions

Figure 3 shows the computational grid for the case AoA_4. Fine grid cells are generated near the wall and around the physically important region where the separation bubble and vortex breakdown occur. The smallest cells are located at the trailing edge corner with dimensions (in wall units) $\Delta y^+ = 2.5$ in the direction normal to the wall, $\Delta x^+ = 25.0$ in the flow direction and $\Delta z^+ = 12.0$ in the spanwise direction. The total number of cells used in the present study is 253,600 for the baseline model, resulting in 6,847,200 and 16,230,400 degrees-of-freedom (DOFs) per equation for the 3rd-order and 4th-order SD schemes respectively. In the SD method, extra DOFs are associated with each cell, so the resolution of the current mesh is close to what is required of a direct numerical simulation.

To model a wing with an infinite-span , a periodic boundary condition is used in the spanwise direction and the span width of the wing is chosen to be 20% of the chord, which was shown to be wide enough in [31, 33]. At the far-field of the computational domain, an absorbing sponge zone boundary condition [34] is imposed, and a no-slip, adiabatic boundary condition is applied on the surface of the wing.

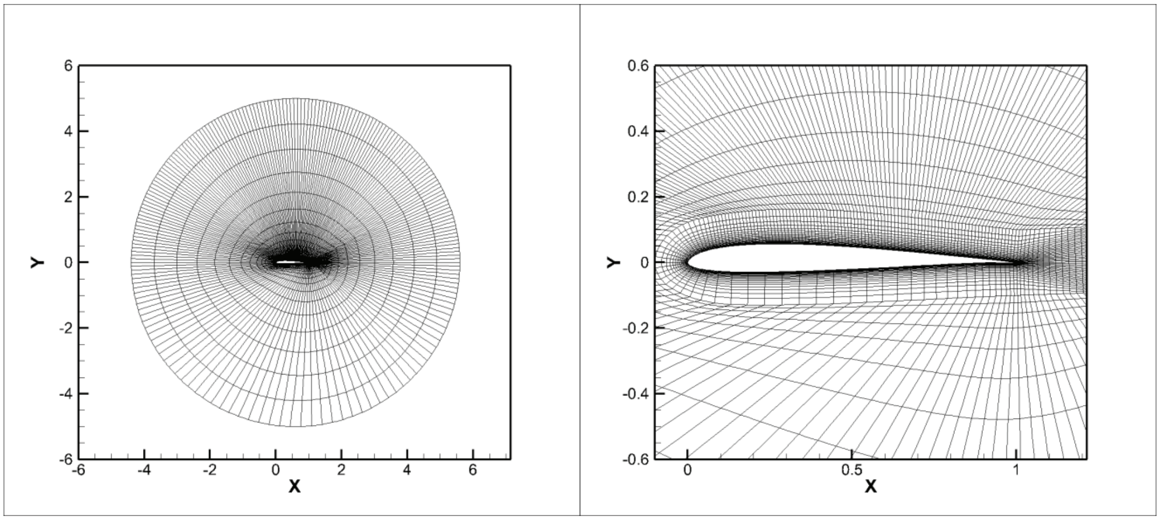

Figure 3 Computational mesh

Averaged and statistical results

In the present numerical simulations, the mean flow field and the statistical results are obtained by averaging the instantaneous flow field over 8 non-dimensional time units. In Figure 4, the mean pressure coefficient C_p and the mean skin friction coefficient C_f distributions on the wing surface are shown. A polynomial order (p) refinement study is carried out by increasing the order of the polynomial in each element from 2 (resulting in 3rd-order accuracy) to 3 (resulting in 4th-order accuracy). A very good agreement between the 3rd-order method and 4th-order method has been found in Figure 4 for both the mean pressure coefficient and the mean skin friction coefficient on the wing surface, thus indicating that the mean flow is p-independent and the spatial resolution provided by the SD method is capable of capturing the main flow features at this Reynolds number.

Table 1 compares the locations of separation, transition and reattachment between the 3rd-order and the 4th-order results. The onset location of transition is defined by a critical value of 0.001 of the normalized Reynolds stress τ_{xy} as used in [33, 35-38]. The differences between the above measurements of the 3rd-order and the 4th-order results are all less than 2%. The results from Galbraith and Visbal [33] are also listed here and the agreement is also good.

Table 1 Separation, transition and reattachment locations

Case	Separation	Transition	Reattachment

3rd-order	0.223	0.515	0.675
4th-order	0.227	0.521	0.685
Galbraith and Visbal [33]	0.23	0.55	0.65

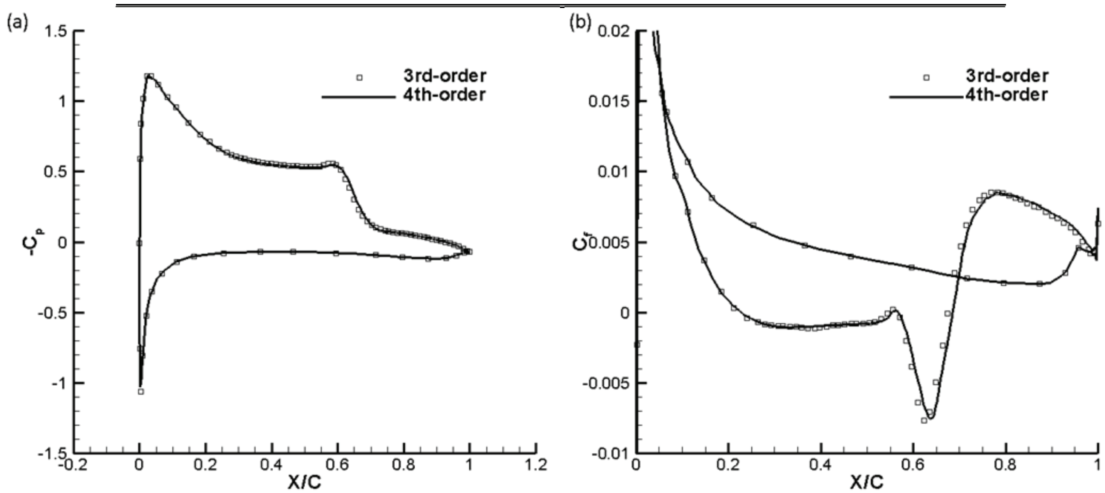

(a) (b)

Figure 4 Mean pressure coefficient (a) and mean skin friction coefficient (b) on the wing surface. Square symbols: 3rd-order result; solid line: 4th-order result.

Flow features associated with the LSB and turbulent transition

Figure 5a displays the mean streamlines around the wing and the mean streamwise velocity field averaged in both time and the spanwise direction. The mean separation bubble and the reattachment of the flow are clearly shown. In Figure 5b, the negative value of the mean spanwise vorticity on the suction surface of the wing at interval $x = [0.0,0.6]$ represents the laminar shear layer before the flow transitions into turbulent flow. The amplitude of the disturbance inside this interval has been found to grow exponentially due to the Kelvin-Helmholtz instability after separation [31, 36-38]. The shear layer terminates around $x = 0.65$ at the end of the LSB (Figure 5a) where the vortex breakdown occurs. A turbulent boundary layer forms at interval $x = [0.75,1.0]$. Figs. 5c and 5d show the statistical distribution of the normalized turbulent kinetic energy $T.K.E.$ and the normalized Reynolds stress τ_{xy}, respectively. Results of both 3rd-order and 4th-order SD schemes are shown and are quite close to each other. The concentration of both $T.K.E.$ and τ_{xy} around $x \approx 0.65$ is strongly related to the process of vortex breakdown, and is discussed later in this section.

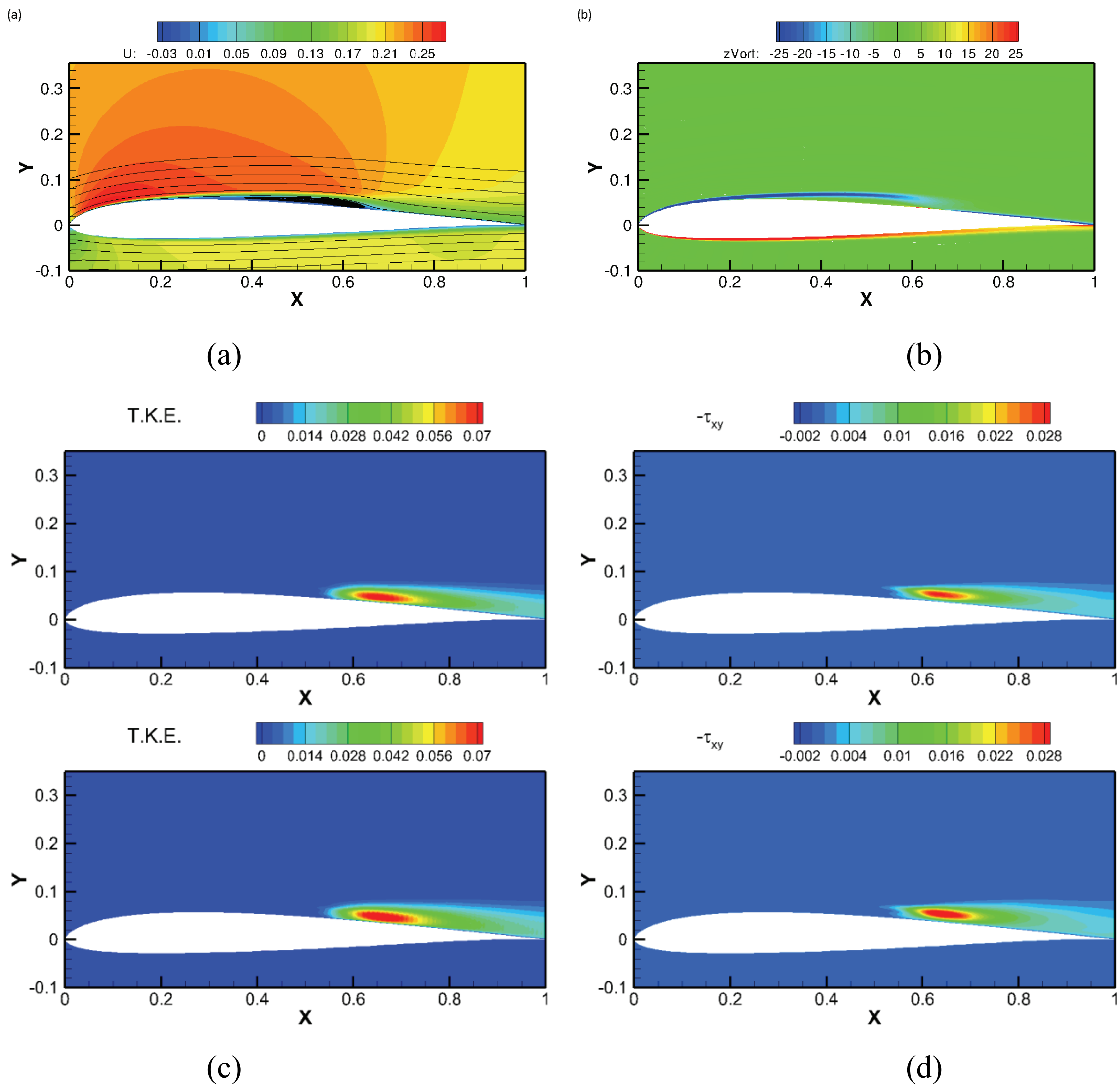

Figure 5. Mean and statistical results of baseline model: (a) mean streamlines around the wing and mean streamwise velocity field; (b) mean spanwise vorticity field; (c) normalized turbulent kinetic energy ($T.K.E.$) distribution (upper: 3rd-order SD scheme; lower: 4th-order scheme); (d) normalized Reynolds stress (τ_{xy}) distribution (upper: 3rd-order SD scheme; lower: 4th-order scheme).

Figure 6 shows the profiles of the mean tangential velocity $\mathrm{u_t}$ at different locations and the corresponding profiles of RMS tangential velocity disturbance $\mathrm{u_t'}$ at the corresponding locations of the baseline model. The development of the mean shear layer from an attached layer to a detached one can be clearly seen. The profiles of RMS of $\mathrm{u_t'}$ vary along with the mean shear layer. After separation, the inflection point gradually shows in the mean velocity profiles (Figure 6.a) and the K-H instability becomes dominant accompanied by the vortex shedding.

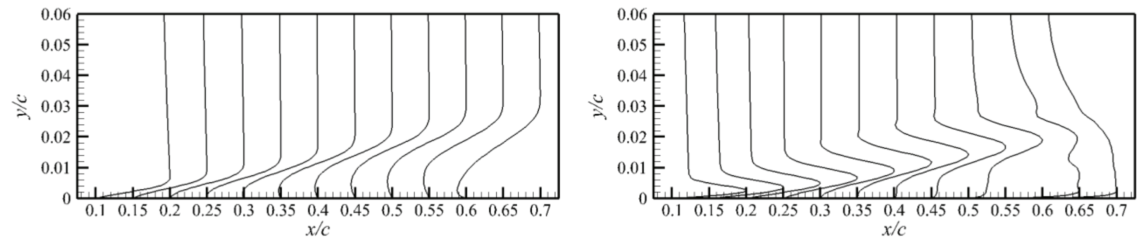

(a) (b)

Figure 6 Numerical results for baseline model: (a) normalized profiles of the mean tangential velocity at different locations; (b) normalized profiles of RMS tangential velocity disturbances at different locations

Figure 7 shows the instantaneous contour lines of the Q-invariant [39] for about a shedding period. Inside the detached shear layer (Figure 5b), vortical tubes (rolls) are shed and grow convectively, as shown in Figure 7. The K-H instability is also called inviscid instability, in which the disturbance is more unstable in two dimensions than in three dimensions. The shedding vortices remain two-dimensional until entering the breakdown stage.

It is observed that two-dimensional vortices break down to small scale structures rapidly in the region $x = [0.6, 0.7]$, as shown in Figure 7. And in the same region, the skin friction and the wall pressure increase suddenly (Figure 4). Finally the flow reattaches to the wall and the LSB is terminated by turbulent flow. As shown in Figure 7, the vortex breakdown process extends from the bottom to the top and the small scale structures close to the wall at interval $x = [0.6, 0.7]$ with upstream-going velocity play an important role in this process. A layer of small scale structures stay near the wall in this region right below the shedding vortices. As the layer remains within the separation bubble region, the small scale structures move upstream due to the reversed flow direction. When the shedding vortices pass the region, the bottom part of the shedding vortices meets and interacts with the upstream going small scale structures. The bottom part of the vortices breaks down to small scale structures first, then the upper part is affected and breaks down by the swirling motion of the vortices. In such a way, the vortex tube breaks down from the bottom to the top due to a feedback mechanism [31]. After the breakdown of the large scale vortices into smaller scale eddies, the flow becomes turbulent. Spalart et al. [40] concluded this process as a simple mechanism of 'transition by contact'. Jones et al. [41] attributed a similar process to be caused by the three dimensional absolute instability.

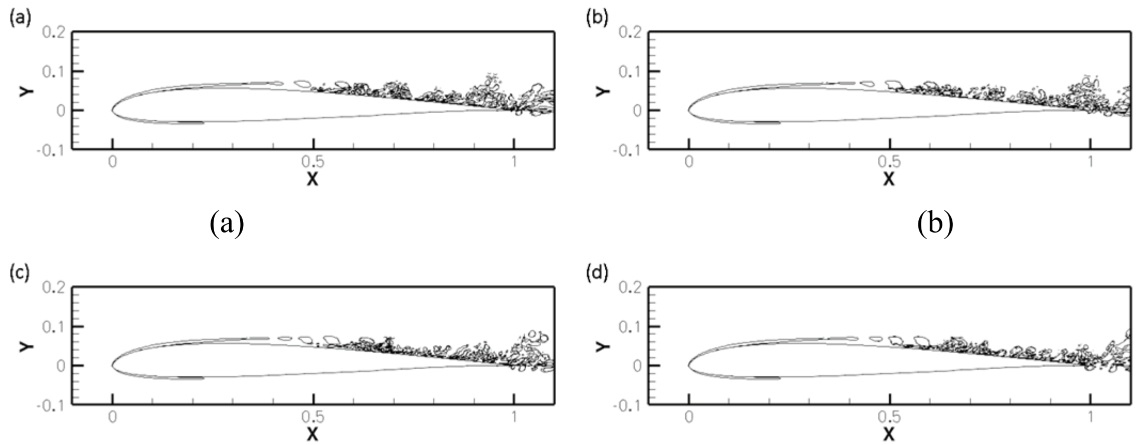

(a) (b)

(c) (d)

Figure 7. Instantaneous contour line of $Q = 1$ for about one shedding period

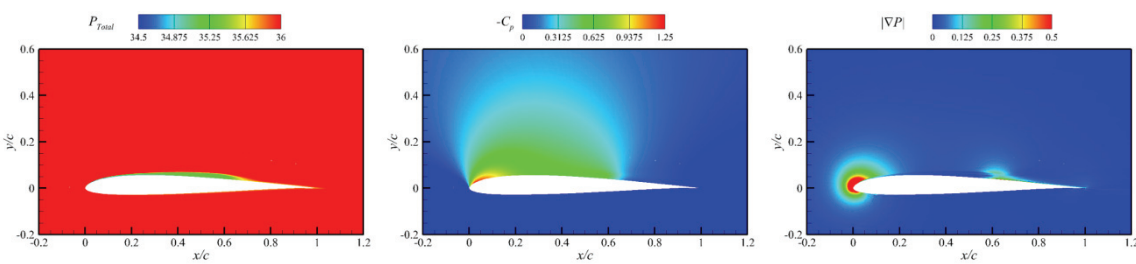

(a) (b) (c)

Figure 8. Averaged numerical results of case AoA_4: Contours of (a) normalized total pressure P_{Total}; (b) pressure coefficient $-C_p$; (c) pressure gradient magnitude $|\nabla P|$.

The contours of the normalized mean total pressure P_{Total}, the mean pressure coefficient C_p distribution and the pressure gradient magnitude $|\nabla P|$ for the case AoA_4 are shown in Figure 8. Both the total pressure and the static pressure are almost constant inside the LSB region and are lower inside the LSB than those outside the LSB. In other words, in the averaged sense the LSB persists a constant low pressure inside and is pressed by high-pressure outside. Around the location $x = 0.65$, there exists a region of high adverse-pressure-gradient (APG) as shown in Figure 8c and a high pressure gradient terminates the LSB. This region around $x = 0.65$ is exactly the same region where the breakdown and reattachment are observed. In the sense of the mean flow field, the pressure difference is balanced by the friction force over the wall as shown in Figure 4. The $\mathrm{T.K.E.}$ and τ_{xy} are also found to be concentrated in the same region as shown in Figure 5c&d. The above features illustrate that this region is physically important to the formation of the LSB and the breakdown process thereafter, to which the attention should be paid when investigating the effects of the surface roughness. It will be shown later that the typical feature of the sudden recovery of pressure and the associated separation in region $x = [0.6, 0.7]$ on the suction side of the baseline model can be altered with the surface roughness.

4. Effects of Surface Roughness

The numerical simulations of the surface roughness effects are carried out in this section. The study can help improve the design of future passive control devices on the wing surface for separation control and drag reduction.

By using the high-order SD method on unstructured hexahedral mesh, geometry of the roughness bumps are modeled as shown in Figure 9. The bump geometry is defined using the following parameters: the width W_{AC}, the length L_{BD} and the height H_{EF} of the bump. The surface edges of the bump are tangentially patched with the wing surface by high-order (P_3) polynomial curves and the curved surface on the top (at point F) of the bump is also tangential to the original wing surface at point E, as shown in Figure 9. In all cases, the discrete roughness bumps are equally spaced near the leading edge before the flow separates. Cases with different geometries, numbers of roughness bumps and AoAs are considered and numerically investigated, and the parameters are listed in Tables 2, 4 and 7, in which all the geometric parameters are normalized by the chord length c.

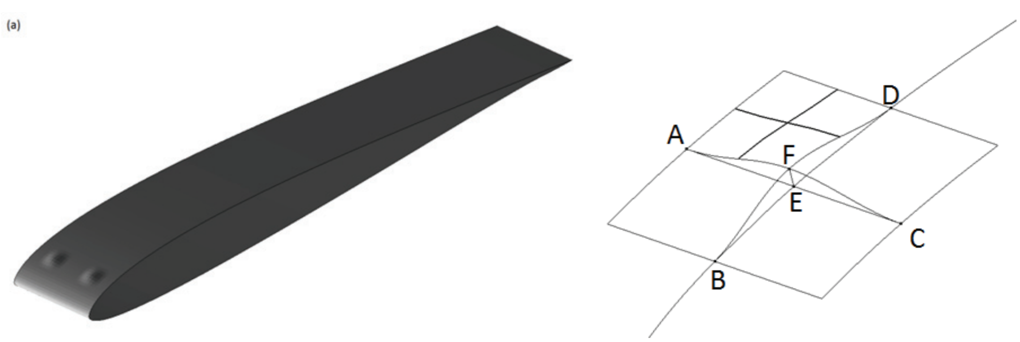

(a) (b)

Figure 9. (a) Roughness bump on the wing surface and (b) bump geometries

a. Effects of roughness bump size

Table 2 Parameters of the roughness bumps

Case	X_E	W_{AC}	L_{BD}	H_{EF}	N_{bump}	δ_E
AoA_4	N/A	N/A	N/A	N/A	N/A	0.0049
AoA_4c	0.05	0.045	0.045	0.0035	2	N/A
AoA_4c.w	0.05	0.090	0.045	0.0035	2	N/A
AoA_4c.h	0.05	0.045	0.045	0.005	2	N/A

Table 3 Mean lift coefficient, drag coefficient (per unit span) and lift-to-drag ratio

Case	C_L	C_D	C_{Dp}	C_{Df}	L/D
AoA_4	0.600	2.34e-2	1.38e-2	0.97e-2	25.6
AoA_4c	0.593	2.05e-2	1.00e-2	1.05e-2	28.9
AoA_4c.w	0.579	2.10e-2	0.94e-2	1.16e-2	27.6
AoA_4c.h	0.579	2.07e-2	0.95e-2	1.12e-2	28.0

Three cases with different roughness geometry are simulated and presented to test the effects of the bump size. The geometric parameters of the roughness bumps in all three cases are shown in Table 2. In order to affect the attached boundary layer profile before separation and also not induce too much viscous drag force, the location and dimension of the bumps in case AoA_4c are chosen after several tests. Through trial and error, the bump size and height were found to affect the flow more than the bump location. Here in all cases, the bumps are placed at a fixed location $\mathrm{x} = 0.05$, where the boundary layer thickness for the baseline model AoA_4 is $\delta_E = 0.0049$. The cases AoA_4c.w and AoA_4c.h are variations based on case AoA_4c. The bumps in AoA_4c.w are twice as wide (W_{AC}) as in AoA_4c. In cases AoA_4c and AoA_4c.w, the height of the bumps is about 70% of the boundary layer thickness δ_E, while in case AoA_4c.h the height is set to close to 100% δ_E.

The instantaneous iso-surfaces and side-views of the Q-invariant are shown in Figure 10 for the baseline model and the cases with roughness bumps. The effectiveness of the bumps in changing the flow field of the baseline model can be clearly seen. In case AoA_4c, vortex shedding in the separation bubble region is observed as in the baseline model AoA_4. However the shedding vortices are distorted as streamwise vorticities are generated behind the bumps. The shedding vortices are closer to the airfoil surface and the frequency of vortex shedding is higher than those in the baseline model, as shown in Figure 10b. It is found in both AoA_4c.w and AoA_4c.h that small scale vortex packets are generated behind the bumps and the pattern is periodic (Figure 10c&d). This implies that changing the width and height of the bumps can dramatically change the flow features, and the wider and taller bumps introduce stronger disturbances and significantly affect the laminar boundary layer flow. The perturbed region (periodic vortical packets) after the bumps grows in the flow direction, takes over the laminar region. Eventually the boundary layer becomes fully turbulent as shown in Figure 10c&d. Vortex shedding is also found in the laminar region of the flow, and the shedding vortical rolls interact with adjacent turbulent region. In cases of AoA_4c.w and AoA_4c.h, the roughness bump act like the turbulators, and the breakdown process is triggered by the vertical packets generated right behind the bumps, as shown in Figure 10c & d.

The mean pressure coefficient and friction coefficient distributions on the suction surface of the controlled cases are shown in Figure 11, compared with the results of the baseline model. As shown in the friction coefficient plots, the separation region is smaller in case AoA_4c than in the baseline model. Disturbed by the upstream bumps, flow separation is delayed, while the breakdown and reattachment occur at an earlier location. In case AoA_4c, the features associated with the LSB, which include a pressure plateau and steep pressure recovery at the strong separation region, are also observed in $x = [0.5, 0.6]$. This indicates the characteristics of the breakdown process in AoA_4c are quite similar to those in the baseline model AoA_4 even though the flow field is disturbed by the streamwise vorticity generated by the bumps. And the feedback mechanism of the circulation flow serves the same important role in the breakdown process of case AoA_4c as in the baseline model. With the increase of the width or height of roughness bumps, the LSBs are completely avoided in cases AoA_4c.w and AoA_4c.h as shown in the friction coefficient plot of Figure 11. A similar trend can be found in the cases of separation active control by increasing the magnitude of suction/blowing [42] and also in the cases by increasing the free-stream turbulence level [43]. In cases AoA_4c.w and AoA_4c.h, the pressure recovers smoothly (Figure 11) without separation and the breakdown process occurs convectively (Figure 10 c&d). The pressure recovery and the associated strong separation region ($x = [0.6, 0.7]$ for case AoA_4 and $x = [0.5, 0.6]$ for case AoA_4c) seem to be closely related to the LSBs. Figure 12 shows the contours of the pressure gradient magnitude for cases AoA_4c and AoA_4c.h. With a reduced LSB in case AoA_4c, the severe APG region (Figure 12.a) can also be observed in $x = [0.5, 0.6]$ but is weaker than that in case AoA_4. In case AoA_4c.h, the severe APG region $x = [0.5, 0.6]$ disappears when the LSB is avoided (Figure 12.b). And in case AoA-4.w the situation is similar to case AoA_4.h.

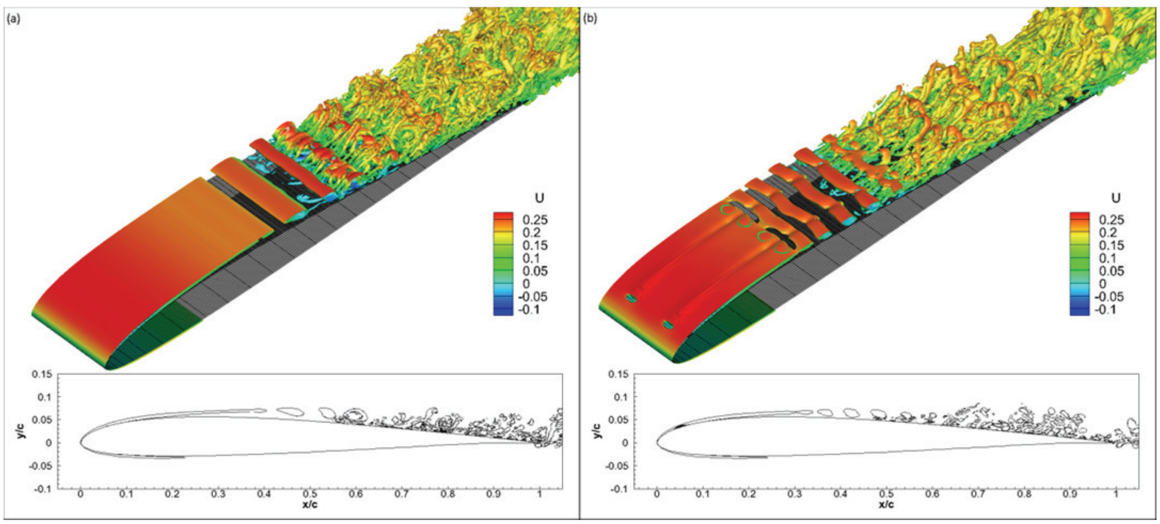

(a) (b)

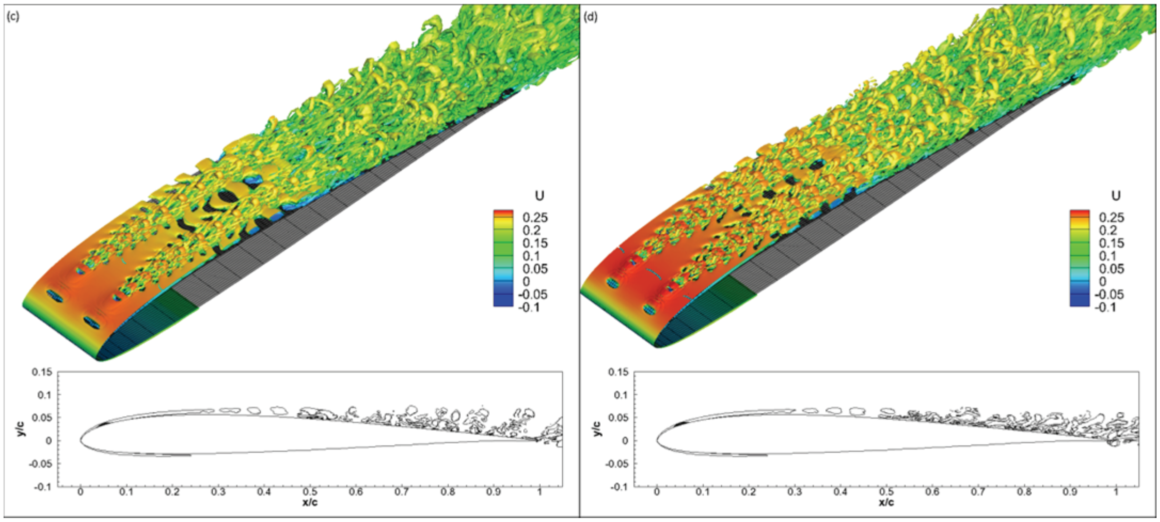

(c) (d)

Figure 10. Iso-surface of Q-invariant colored by streamwise velocity and side-view: (a) AoA_4, (b) AoA_4c, (c) AoA_4c.w, (d) AoA_4c.h

Table 3 presents the mean lift and drag coefficients per unit span and the lift-to-drag ratio of all the cases. The drag coefficients decrease for all the controlled cases, and the lift coefficients also decrease slightly. It can be seen in Figs. 10 and 11 that roughness bumps generate a larger turbulent flow region and thus the friction drag increases. The contribution to the drag C_D from both pressure drag C_{Dp} and friction drag C_{Df} are also listed in Table 3 for all the cases. It is shown that with the reduction of the LSB, the pressure drag C_{Dp} decreases and the friction drag C_{Df} increases. However, the pressure drag decreases by a larger amount than the increase of friction drag resulting in an overall drag reduction of over 10%. In addition, the lift-to-drag ratio is increased by at least 10% for all the controlled cases, as shown in Table 3.

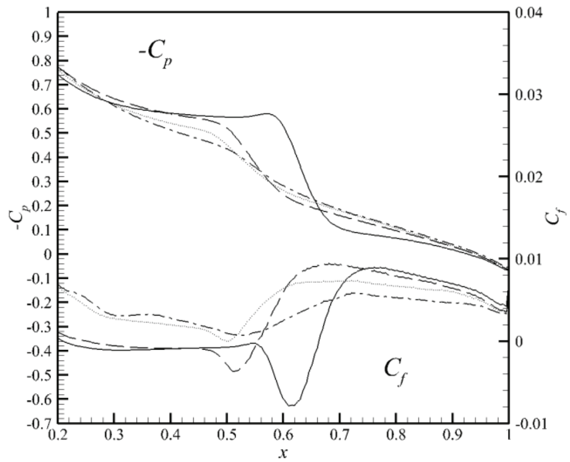

Figure 11. Mean pressure coefficient and mean skin friction coefficient on the wing surface; AoA_4 (solid line, -), AoA_4c (dash line, - - -), AoA_4c.w (dash-dot line, -.-.-) and AoA_4c.h (dot line, ….)

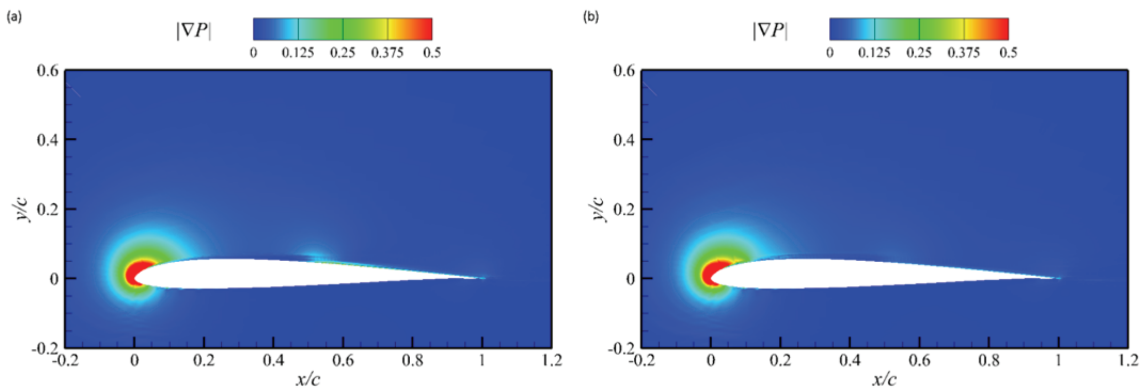

(a) (b)

Figure 12. Contours of pressure gradient magnitude. (a) AoA_4c; (b)AoA_4c.h

b. Effects of the number of bump

Case AoA_4c has two roughness bumps on the span width of 20% chord length and it is again used as the starting point for variations. Cases AoA_4c.1 and AoA_4c.4 have just 1 and 4 bumps on the same span width with everything else remaining the same. Case AoA_4c.4n reduces the bump width W_{AC} by 50% and double the number of bumps from 2 to 4, which is for further comparison with the cases AoA_4c and AoA_4c.4. Figure 13 shows the instantaneous iso-surface and side-view of Q-invariant of all the cases. Similar to case AoA_4c (Figure 13.b), the attached boundary layer and the following shedding vortices are perturbed but still remain laminar for all the cases. Vortex shedding due to the

K-H instability occurs in all the cases and the turbulent vortical packet formed in cases AoA_4c.w and AoA_4c.h is not observed here. The number of bumps N_{bump} affects the spanwise wavelength of the disturbance. After separation, the K-H instability takes the dominant role of disturbance growth and the most unstable mode of K-H instability which is also called inviscid instability is two dimensional and the spatial growth rate of the disturbance decreases with the increase of the spanwise wave number [44]. Thus the physics and mechanisms are associated with the three dimensional instability in the detached shear layer and also possibly the elliptical instability [45, 41] of the shedding vortices.

Table 4. Parameters of the roughness bumps

Case	X_E	W_{AC}	L_{BD}	H_{EF}	N_{bump}	δ_E
AoA_4	N/A	N/A	N/A	N/A	N/A	0.0049
AoA_4c.1	0.05	0.045	0.045	0.0035	1	N/A
AoA_4c	0.05	0.045	0.045	0.0035	2	N/A
AoA_4c.4	0.05	0.045	0.045	0.0035	4	N/A
AoA_4c.4n	0.05	0.0225	0.045	0.0035	4	N/A

Table 5 Mean lift coefficient, drag coefficient (per unit span) and lift-to-drag ratio

Case	C_L	C_D	C_{Dp}	C_{Df}	L/D
AoA_4	0.600	2.34e-2	1.38e-2	0.97e-2	25.6
AoA_4c.1	0.581	2.25e-2	1.20e-2	1.04e-2	25.8
AoA_4c	0.593	2.05e-2	1.00e-2	1.05e-2	28.9
AoA_4c.4	0.572	2.20e-2	1.15e-2	1.05e-2	26.0
AoA_4c.4n	0.593	2.09e-2	1.07e-2	1.02e-2	28.4

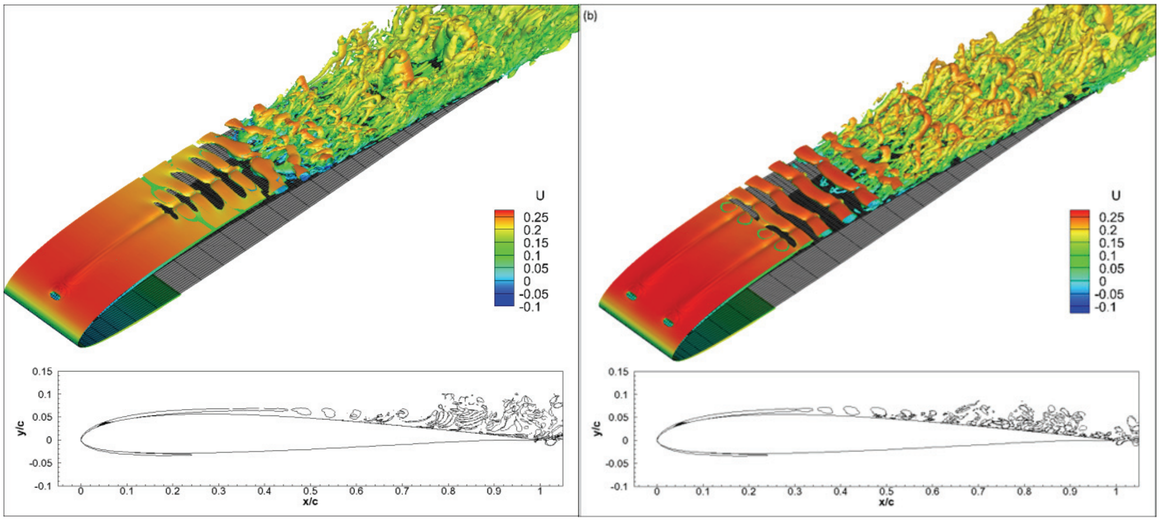

(a) (b)

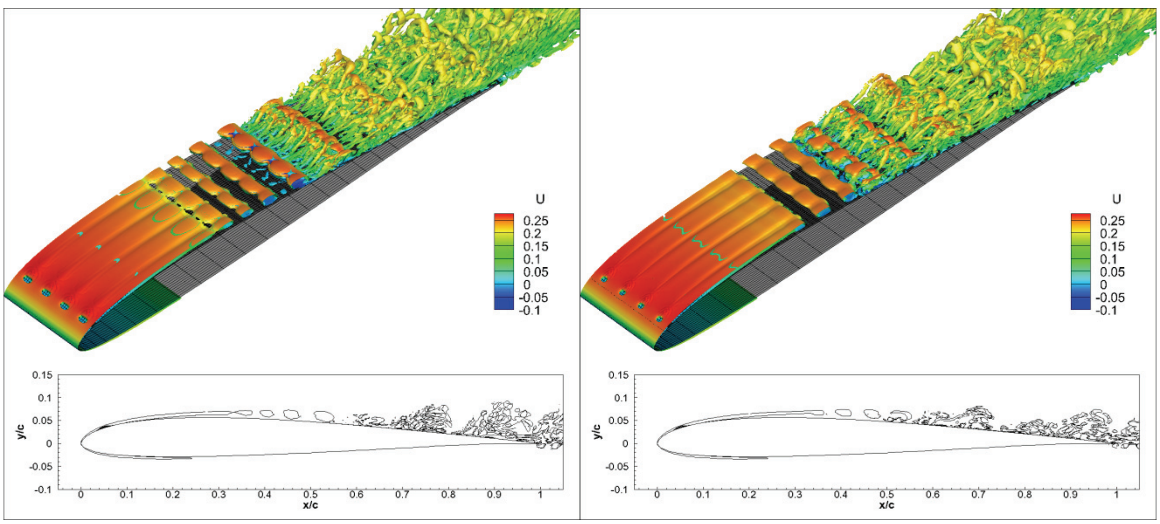

(c) (d)

Figure 13 Iso-surface of Q-invariant colored by streamwise velocity and side-view: (a) AoA_4c.1, (b) AoA_4c, (c) AoA_4c.4, (d) AoA_4c.4n

Figure 14 shows the instantaneous contours of u-velocity and streamwise vorticity on the cutting plane at $y = 0.065$ for all the cases. It can be seen that high speed flow is induced behind the bumps. With narrower roughness bumps in case AoA_4c.4n, the influence region of the high speed flow is smaller than that in case AoA_4c.4 (Figure 14). The spanwise influences of the bumps on the laminar flow field and the development of the streamwise vorticity in the separation region can be clearly seen in Figure 14. The spanwise expansion of streamwise vorticities of case AoA_4c.1 is clearly shown in Figure 14.(1).

With multiple roughness bumps over the span of the wings, the interaction between the streamwise vorticities generated by the adjacent bumps are shown in Figure 14.(2-4).

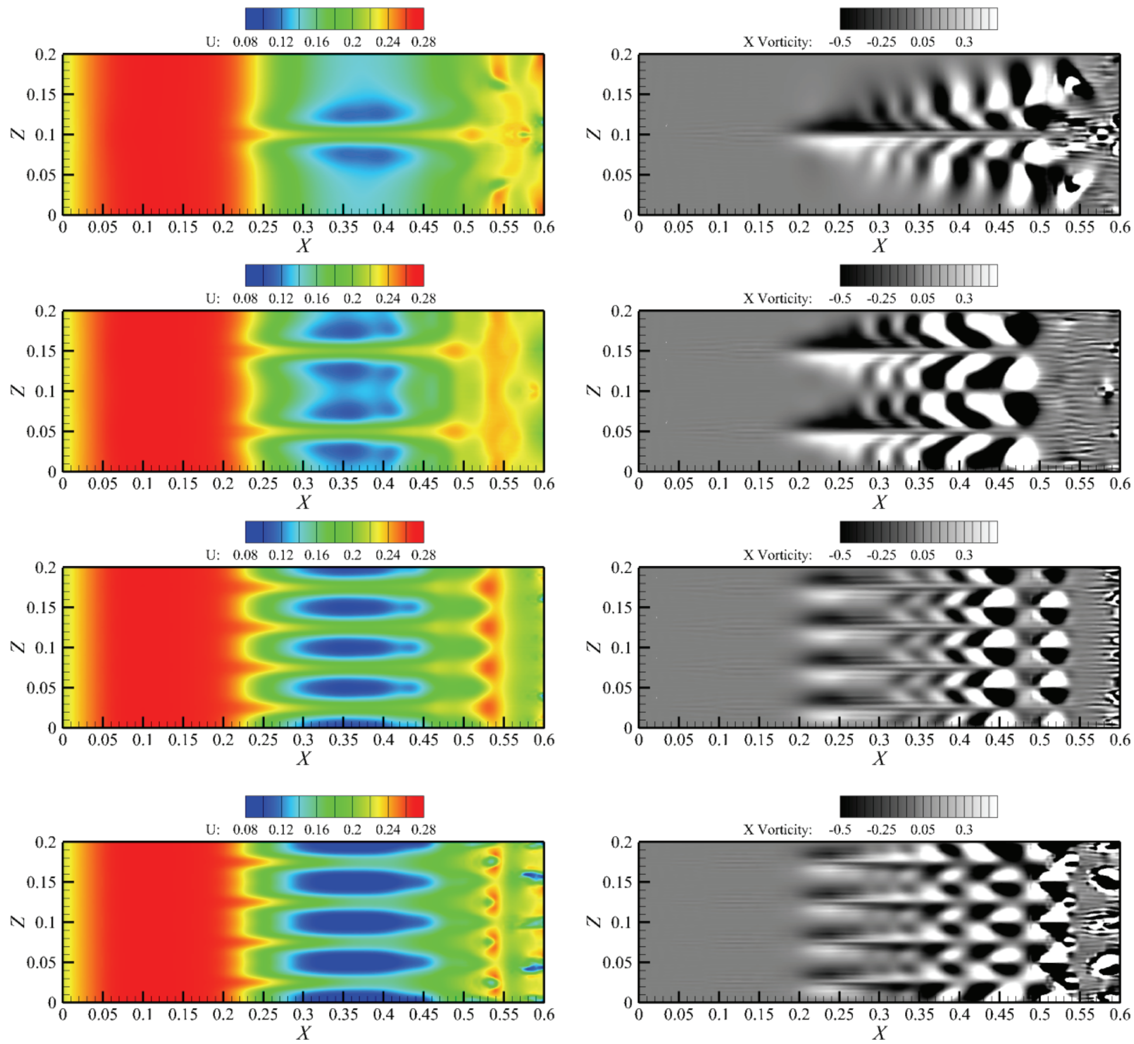

(a) (b)

Figure 14 The instantaneous contours of u-velocity (a) and streamwise vorticity (b) on the sliced plane at $y = 0.065$: from top to bottom (1) AoA_4c.1, (2) AoA_4c, (3) AoA_4c.4, (4) AoA_4c.4n

The mean pressure coefficient and friction coefficient distributions are shown in Figure 15, in comparison with those of the baseline model AoA_4. The LSBs are reduced in all the cases with roughness bumps. The length of the LSB is shorter for case AoA_4c.1 than that in case AoA_4c. However, further increasing the number of bumps N_{bump} does not further reduce the length of the LSBs. The mean pressure coefficient and friction coefficient distributions of cases AoA_4c.4 and AoA_4c.4n are found very close to those of AoA_4c (Figure 15), and the separation region is even larger in case AoA_4c.4.

Table 5 presents the mean lift and drag coefficients per unit span and the lift-to-drag ratio of all the cases. With one roughness bump in case AoA_4c.1, both the drag coefficient and the pressure drag coefficient decrease. But the lift coefficient also decreases, such that only a little improvement of L/D ratio is achieved. The similar behavior of the mean pressure and friction on the wall in both controlled cases results in similar aerodynamic performances for cases AoA_4c and AoA_4c.4n, as listed in Table 5. With 4 bumps in case AoA_4c.4, the lift coefficient is degraded (5%) compared to the baseline model. Although the drag coefficient is reduced due to the decrease of the pressure drag, the L/D ratio improvement is less than those in cases AoA_4c and AoA_4c.4n.

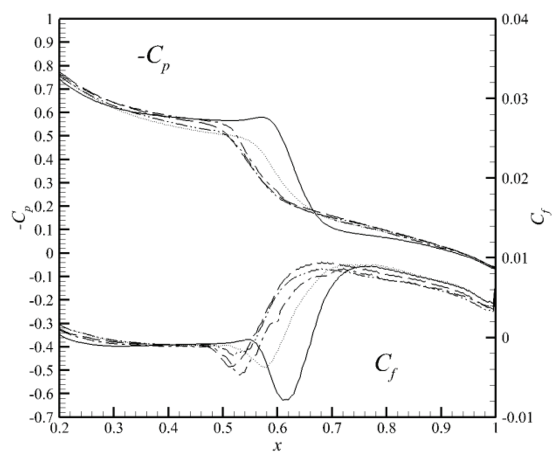

Figure 15 Mean pressure coefficient and mean skin friction coefficient on the wing surface; AoA_4 (solid line, -), AoA_4c (dash line, - - -) and AoA_4c.4n (dash-dot line, -.-.-)

c. Effects of the Angle of Attack (AoA)

The effects of AoA are tested and investigated here by adjusting the incidence of the flow. $AoA = 2\ deg$ and 6 deg are considered and the same roughness configuration in case AoA_4c are used here. At a different AoA, the boundary thickness δ_E is different, and the effects will be different. With the baseline model at different $AoAs$, the thickness δ_E of the boundary layer and the ratio of the bump height H_{EF} to δ_E are listed in Table 6. Figure 16 shows the instantaneous iso-surfaces and side-views of Q-invariant of cases AoA_2 and AoA_2c, and Figure 17 shows those of cases AoA_6 and AoA_6c. The mean pressure coefficient and friction coefficient distributions on the suction surface are shown in Figure 18 for both $AoAs$. The same results of cases AoA_4 and AoA_4c can be found Figure 10 and Figure 11. The LSBs are diminished in cases AoA_2c and avoided in case AoA_6c as shown by the friction coefficient plots in Figure 18. With the roughness bumps, the recovery of the pressure on the wall for all the controlled cases is much smoother than in the baseline model.

Table 6 Parameters of the roughness bumps

Case	X_E	W_{AC}	L_{BD}	H_{EF}	N_{bump}	δ_E	H_{EF}/δ_E
AoA_2c	0.05	0.045	0.045	0.0035	2	0.0046	76.1%
AoA_4c	0.05	0.045	0.045	0.0035	2	0.0049	71.4%
AoA_6c	0.05	0.045	0.045	0.0035	2	0.0056	62.5%

Table 7 Mean lift coefficient, drag coefficient (per unit span) and lift-to-drag ratio

Case	C_L	C_D	C_{Dp}	C_{Df}	L/D	Benefit
AoA-2	0.401	1.68e-2	0.78-2	0.90e-2	23.8	N/A
AoA-4	0.600	2.34e-2	1.38e-2	0.97e-2	25.6	N/A
AoA-6	0.786	3.14e-2	2.15e-2	0.99e-2	25.1	N/A
AoA-2c	0.400	1.63e-2	0.68e-2	0.95e-2	24.5	3%
AoA-4c	0.593	2.05e-2	1.00e-2	1.05e-2	28.9	13%
AoA-6c	0.766	2.56e-2	1.37e-2	1.19e-2	29.9	19%

In case AoA_2c, the shedding vortices are found to be disturbed in a similar pattern as in case AoA_4c. In case AoA_6c, the periodic vortical packets are generated behind the bumps in the same pattern as in cases AoA_4c.h and AoA_4c.w. With the increase of AoA, the boundary layer thickness δ_E at the bump location $X_E = 0.05$ increases (Table 6), thus the ratio H_{EF}/δ_E decreases. It has been shown previously that at AoA $= 4$ deg and the same location, taller bumps with higher H_{EF}/δ_E ratio in case AoA_4c.h may generate larger disturbances and the vortical packets. However, here the situation is opposite and the vortical packets are generated behind the bumps in case AoA_6c with lower H_{EF}/δ_E ratio. This shows that the effects of the roughness bumps on the flow field are not uniquely determined by the H_{EF}/δ_E ratio, but also by the instability features of the flow field near the location of bumps. Figure 19.a shows the mean tangential velocity profiles at location

$x = 0.1$, which is right behind the location of the bumps $X_E = 0.05$, for the baseline model at three AoAs. Figure 19.b shows the wave speed s and growth rate α_i of the convective instability obtained by Linear Stability Theory (LST) [44, 46] based on the mean tangential velocity profiles as shown in Figure 19.a. In LST, the fluctuations of the primitive variables $\phi = \{u, v, w, p, T, \rho\}$ are assumed to take the harmonic wave form: $\phi = \hat{\phi}(y)e^{i(\alpha x+\beta z-\omega t)}$. For convective instability (spatial instability), β, ω are assumed to be real and $\alpha = \alpha_r + i\alpha_i$ is complex. Thus the flow is convective unstable if $\alpha_i < 0$, and vice versa. In case AoA_6c the location $x = 0.1$ is close to the mean separation point (Figure 18) and the mean tangential velocity profile (Figure 19.a) generates the inflection point and separation. After separation, the K-H (inviscid) instability is usually more unstable, and has a higher growth rate than the Tollmien-Schlitchting (T-S) instability in the attached boundary layer. Both the unstable frequency range and the growth rate of the convective instability of AoA_6 are much larger than those in the other two cases (Figure 19.b). In cases AoA_2c and AoA_4c, the bumps locate further upstream from the mean separation points. The unstable frequency range and the growth rate of the convective instability of case AoA_4 are very small as shown in Figure 19.b, and it is even convectively stable in case AoA_2 at location $x = 0.1$ as predicted by LST. Thus the flow at $x = 0.1$ in case AoA_6c is more unstable to be perturbed by the bump and causes the generation of the vortical packets, although the H_{EF}/δ_E ratio is lower than these in cases AoA_2c and AoA_4c.

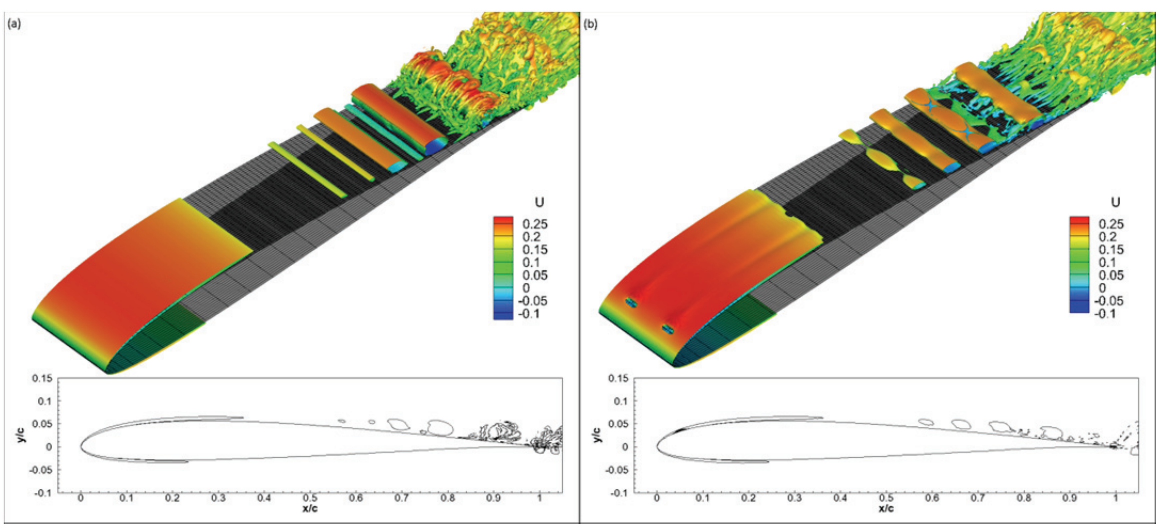

(a) (b)

Figure 16 Iso-surface of Q-invariant colored by streamwise velocity at AoA $= 2$deg; (a) AoA-2; (b) AoA-2c.

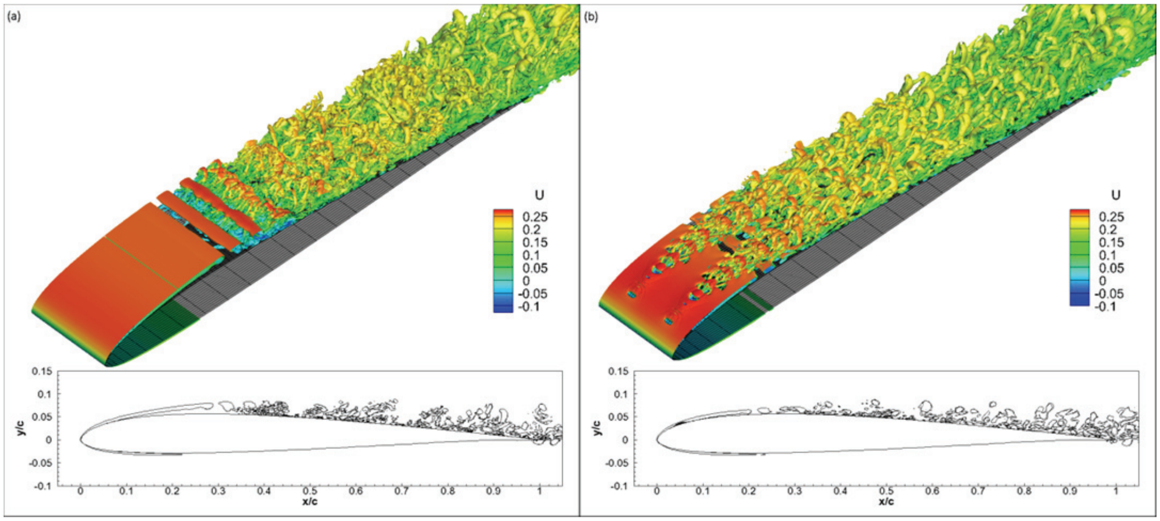

(a) (b)

Figure 17 Iso-surface of Q-invariant colored by streamwise velocity at AoA $= 6$deg; (a) AoA_6; (b) AoA_6c.

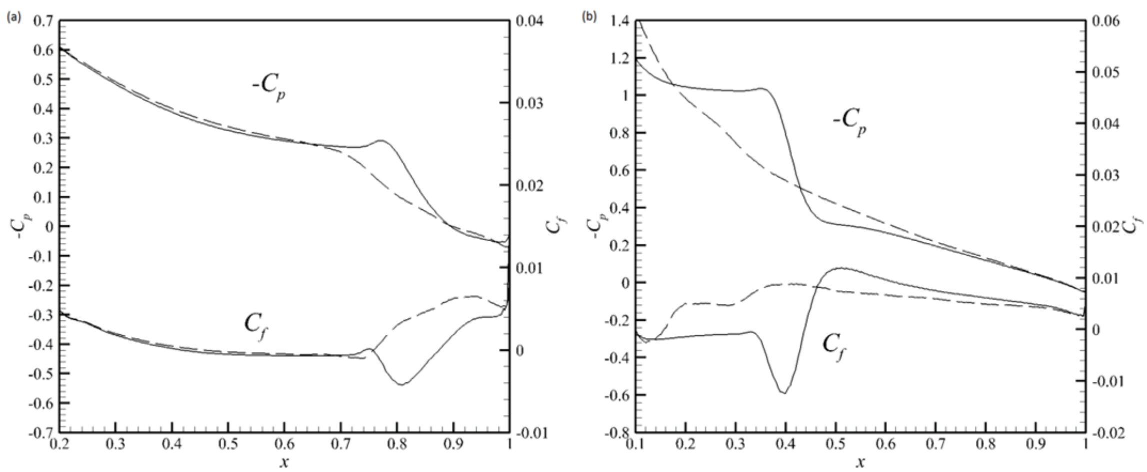

(a) (b)

Figure 18 Mean pressure coefficient and mean skin friction coefficient on the wing surface; baseline model (solid line, -) and controlled case (dash line, - - -); (a) AoA $= 2$deg, (b) AoA $= 6$deg

Table 7 lists the mean lift coefficient, drag coefficient and lift-to-drag ratio for both the baseline and controlled cases at different AoAs. In current cases, the roughness bumps are more effective on performance improvement at higher AoAs. Figure 20 plots the pressure drag coefficient distributions and the lift-to-drag ratio for all the baseline and controlled cases at three AoAs. In the baseline cases, the lift and drag both increase with the increase of the AoA (Table 7). However, the pressure drag force increases dramatically as the LSB moves upstream with the increase of AoA (Table 7 and Figure 20.b), which causes the deficit of the lift-to-drag ratio at AoA $= 6$ deg (Table 7 and Figure 20.a). In the controlled cases, the lift, the drag and the pressure drag decreases at all the AoAs, though the friction drag increases slightly because of the larger turbulent boundary layer flow region. The $\mathrm{L/D}$ ratio is improved in the controlled cases at each of the AoAs as listed in Table 7 and shown in Figure 20. Especially for case AoA_6c, the $\mathrm{L/D}$ ratio increases significantly comparing with baseline case AoA_6 (Figure 20.a).

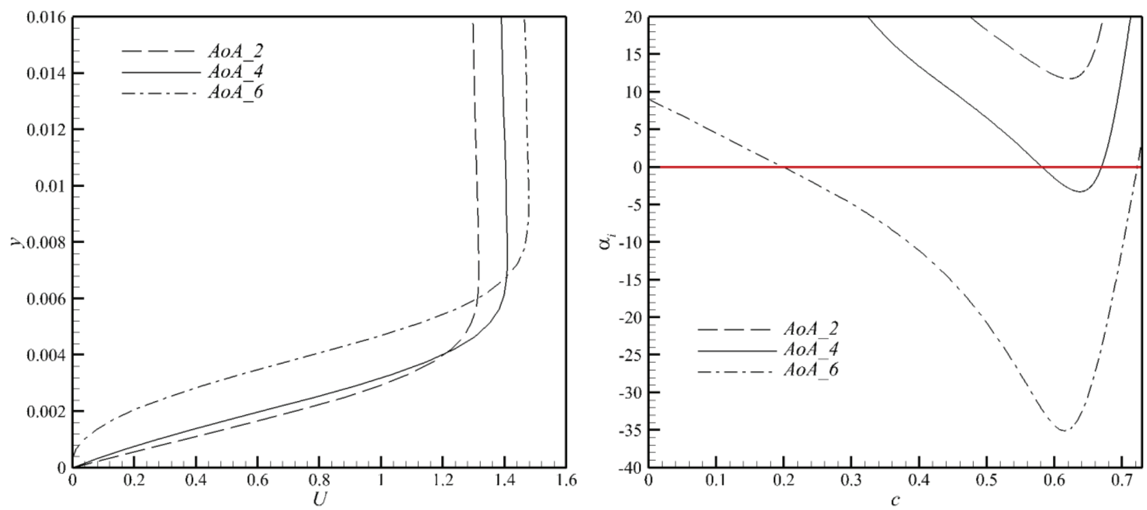

(a) (b)

Figure 19 (a) Tangential velocity profiles at $x = 0.1$; (b) unstable frequency range and growth rate of the convective instability obtained by LST at $x = 0.1$

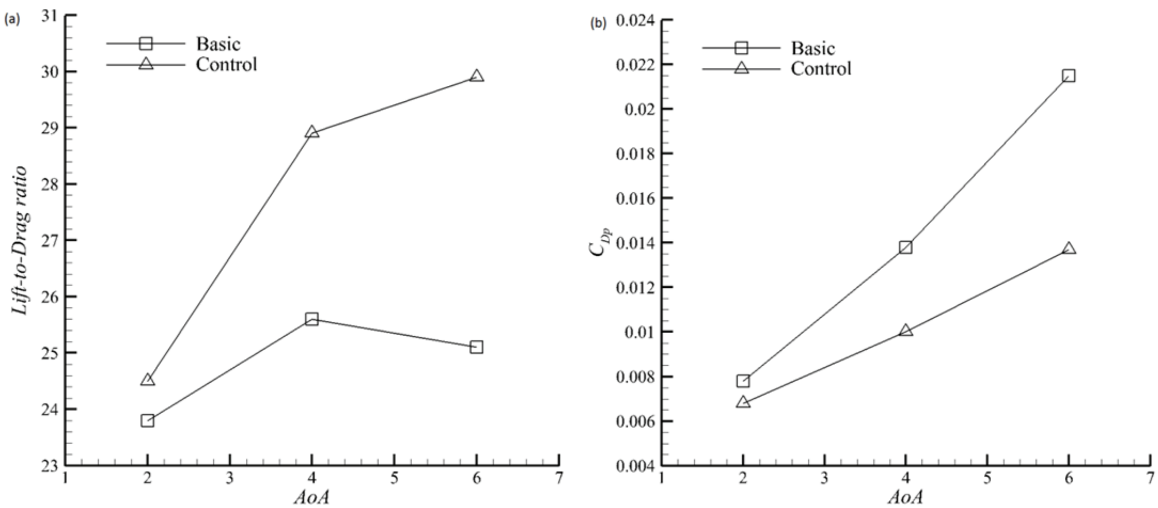

(a) (b)

Figure 20 (a) Lift-to-drag ratio and (b) pressure drag coefficient distributions at different AoAs

5. Conclusion

The numerical simulations of a passive flow control technique using roughness bumps on a low-Reynolds number wing are presented in this paper. A high-order spectral difference Navier-Stokes solver is used in the simulations. The SD method with unstructured hexahedral mesh is capable of capturing the LSB and the transition process well over the suction side of the airfoil. The numerical results of the baseline cases and controlled cases are extensively investigated and discussed.

By introducing the roughness bumps near the leading edge, the LSBs are reduced or avoided depending on the bump geometric parameters. It is found that larger and taller bumps generate larger disturbances, which trigger the vortex breakdown, and delay or avoid flow separation. In addition, the flow also transitions into turbulent flow sooner. Although the friction drag increases slightly, the pressure drag is significantly reduced resulting in an overall drag reduction. The reduction of LSBs by roughness bumps also slightly reduces the lift. However, the lift-to-drag ratio is increased in the cases with carefully chosen surface roughness bumps.

The effects of the surface roughness are also dependent on the number of roughness bumps. The aerodynamic performance is improved by increasing the number of bumps from one to two. However, the performance is degraded by further doubling the number of bumps. Reducing the width of the bumps by 50% regains the aerodynamic performance. The detailed physics is related with the three-dimensional K-H instability of the detached shear layer and possible the elliptical instability of the shedding vortices which worth future investigation.

With a fixed configuration of bumps, the effects of bumps are tested over three AoAs. It is found that the effects of roughness depend on multiple factors including the size of the bumps and the instability of the local flow behind the roughness bumps. In the baseline cases, the LSB causes a dramatic increase of the pressure drag which decrease the lift-to-drag ratio with the increase of AoA. In the cases with surface roughness, the aerodynamic performance has been largely improved with the diminishing of the LSB especially at higher AoAs.

Acknowledge

The authors would like to acknowledge the support from the Air Force Office of Scientific Research and the Department of Aerospace Engineering, Iowa State University.

References

[1] Saric WS, Carrillo Jr. RB, Reibert MS, 1998. Leading-edge Roughness as a Transition Control Mechanism, AIAA Paper Number 98-0781

[2] Saric WS, Reed HL 2002. Supersonic Laminar Flow Control on Swept Wings Using Distributed Roughness, AIAA Paper Number 2002-0147

[3] White, E.B., & Saric, W.S., Application of variable leading-edge roughness for transition control on swept wings, AIAA paper 2000-0283.

[4] Carpenter, A. L., Saric, W. S., and Reed, H. L., "In-Flight Receptivity Experiments on a 30-Degree Swept-Wing Using Micron-Sized Discrete Roughness Elements," AIAA Paper 2009-590, Jan. 2009.

[5] Carpenter, A. L., Saric,W. S., and Reed, H. L., "Roughness Receptivity in Swept-Wing Boundary Layers—Experiments," International Journal of Engineering Systems Modelling and Simulation, Vol. 2, No. 1/2, Mar. 2010, pp. 128–138.

[6] Ergin, F. G., and White, E. B., "Unsteady and Transitional Flows Behind Roughness Elements," AIAA Journal, Vol. 44, No. 11, 2006, pp. 2504–2514.

[7] Berg, D., "Surface Roughness Effect on a Mach 6 Turbulent Boundary Layer," AIAA Journal, Vol. 17, No. 9, 1979, pp. 929, 930.

[8] Latin, R., and Bowersox, R., "Temporal Turbulent Flow Structure for Supersonic Rough-Wall Boundary Layers," AIAA Journal, Vol. 40, No. 5, 2002, pp. 832–841.

[9] Fransson, J. H. M., Talamelli, A., Brandt L. & Cossu, C. 2006 Delaying transition to turbulence by a passive mechanism. Phys. Rev. Lett., 96, 064501.

[10] Fransson, J. H. M., Brandt L., Talamelli, A. & Cossu, C. 2005 Experimental and theoretical study of the stabilization of Tollmien-Schlichting waves by finite amplitude streaks. Phys. Fluids, 17, 054110.

[11] Y. Zhang, T. Igarashi and H. Hu , "Experimental Investigations on the Performance Degradation of a Low-Reynolds-Number Airfoil with Distributed Leading Edge Roughness", AIAA-2011-1102

[12] R. Honsaker and W.W. Huebsch, 2005, Parametric Study of Dynamic Surface Roughness as a Mechanism for Flow Control, AIAA 2005-4732

[13] Rizzetta, D. P., and Visbal, M. R., "Direct Numerical Simulation of FlowPast an Array of Distributed Roughness Elements," AIAA Journal, Vol. 45, No. 8, Aug. 2007, pp. 1967–1976.

[14] D. Rizzetta, Miguel Visbal, H. Reed and W. Saric, "Direct Numerical Simulation of Discrete Roughness on a Swept-Wing Leading Edge", AIAA Journal 2010 0001-1452 vol.48 no.11 (2660-2673)

[15] J. Redford, N. Sandham and G. Roberts, "Compressibility Effects on Boundary-Layer Transition Induced by an Isolated Roughness Element" , AIAA Journal 2010 0001-1452 vol.48 no.12 (2818-2830)

[16] A. Santhanakrishnan and J. D. Jacob, "Effect of Regular Surface Perturbations on Flow Over an Airfoil", AIAA-2005-5145

[17] A.V. Boiko, A.V. Dovgal and S. Hein, "Control of a laminar separating boundary layer by induced stationary perturbations", European Journal of Mechanics - B/Fluids Volume 27, Issue 4, July-August 2008, Pages 466-476

[18] Patera, A.T., A Spectral element method for fluid dynamics: Laminar flow in a channel expansion, J. Comput. Phys. 54, 468(1984).

[19] Kopriva, D.A. and Kolias, J.H., A conservative staggered –grid Chebyshev multidomain method for compressible flows, J. Comput. Phys. 125, 244(1996).

[20] D.A. Kopriva, J.H. Kolias, A Staggered-Grid Multidomain Spectral Mthod for the Compressible Navier-Stokes Equations,J. Comput. Phys. 143 (1998) 125-158.

[21] Barth, T.J. and Frederickson, P.O., High-Order Solution of the Euler Equations on Unstructured Grids using Quadratic Reconstruction, AIAA Paper No. 90-0013(1990).

[22] Hu, C. and Shu, C.-W., Weighted essentially non-oscillatory schemes on triangular meshes, J. Comput. Phys. 150, 97 (1999).

[23] Cockburn, B. and Shu, C.-W., TVB Runge-Kutta local projection discontinuous Galerkin finite element method for conservation laws II: General framework, Math. Comput. 52,411(1989).

[24] Abgrall, R. and Roe, P.L., High Order Fluctuation Schemes on Triangular Meshes, Journal of Scientific Computing, Volume 19, pp. 3 – 36, 2003.

[25] Wang, Z.J. and Liu, Y., Spectral (Finite) Volume Method for Conservation Laws on Unstructured Grids III: Extension to One-Dimensional Systems, J. Scientific Computing, Vol. 20 No. 1, pp.137-157 (2004).

[26] Liu, Y., Vinokur, M., and Wang, Z.J., Discontinuous Spectral Difference Method for Conservation Laws on Unstructured Grids, the 3rd International Conference in CFD, Toronto, Canada July 2004.

[27] Liu, Y, Vinokur, M., and Wang, Z.J., Multi-Dimensional Spectral Difference Method for Unstructured Grids, AIAA-2005-0320.

[28] Wang, Z. J., and Liu, Y., The Spectral Difference Method for the 2D Euler Equations on Unstructured Grids, AIAA-2005-5112.

[29] Huang, P.G., Wang, Z.J., and Liu, Y., An Implicit Space-Time Spectral Difference Method for Discontinuity Capturing Using Adaptive Polynomials, AIAA-2005-5255.

[30] Y. Sun, Z.J. Wang, Y. Liu, High-Order Multidomain Spectral Difference Method for the Navier-Stokes Equations on Unstructured Hexahedral Grids, Communications in Computational Physics, Vol. 2, No. 2(2007) 310-333.

[31] Y. Zhou and Z.J. Wang, "Implicit Large Eddy Simulation of Transitional Flow over a SD7003 Wing Using High-order Spectral Difference Method", AIAA-2010-4442

[32] P. L. Roe, Approximate Riemann solvers, parameter vectors, and difference schemes, J. Comput. Phys. 43 (1981) 357-372.

[33] Galbraith, M. and Visbal, M., "Implicit Large Eddy Simulation of low Reynolds number flow past the SD7003 airfoil," Proc. of the 46th AIAA Aerospace Sciences Meeting and Exhibit, Reno, Nevada, AIAA-2008-225, 2008.

[34] Zhou, Y. and Wang, Z. J. 2010 Absorbing Boundary Conditions for the Euler and Navier-Stokes Equations with the Spectral Difference Method, Journal of Computational Physics 229, 8733-8749

[35] Volino, R. J., and Hultgren, L. S., 2001, Measurements in Separated and Transitional Boundary Layers Under Low-Pressure Turbine Airfoil Conditions, ASME J. Turbomach., 123, pp. 189–197.

[36] Ol, M. V., Hanff, E., McAuliffe, B., Scholz, U., and Kaehler, C., 2005, "Comparison of Laminar Separation Bubble Measurements on a Low Reynolds Number Airfoil in Three Facilities," 35th AIAA Fluid Dynamics Conference and Exhibit, Toronto, Ontario, June 6–9, AIAA Paper 2005-5149.

[37] Burgmann, S., Brucker, S., Schroder, W., 2006, Scanning PIV Measurements of a Laminar Separation Bubble, Exp. Fluids, 41, pp. 319–326.

[38] Hu, H., Yang, Z.F., An Experimental Study of the Laminar Flow Separation on a Low-Reynolds-Number Airfoil, Journal of Fluids Engineering, May 2008, Vol. 130 / 051101-1

[39] Dubeif, Y. and Delcayre, F., "On Coherent-vortex Identification in Turbulence," Journal of Turbulence, Vol. 1, No. 11, 2000, pp. 1-22.

[40] Spalart, P. R. & Strelets, M. K. H. 2000 Mechanisms of transition and heat transfer in a separation bubble. J. Fluid Mech. 403, 329–349.

[41] Jones, L. E., Sandberg, R. S. & Sandham, N. D 2008 Direct numerical simulations of forced and unforced separation bubbles on an airfoil at incidence. J. Fluid Mech. 602, 175–207.

[42] H. F. Fasel, W. Balzer and A. Gross. 2008 "Investigation of separation control for low-pressure turbines using cfd". 26th international congress of the aeronautical sciences.

[43] Zaki T.A., Wissink J.G., Rodi W. and Durbin P. A. 2010 Direct numerical simulations of transition in a compressor cascade: the influence of free-stream turbulence, J FLUID MECH, Vol:665, Pages:57-98

[44] Drazin, P. G. 2002 Introduction to hydrodynamic stability. Cambridge University Press, ISBN 0 521 00965 0.

[45] Williamson, C. H. K. 1996 Three-dimensional wake transition. J. Fluid Mech. 328, 345–407.

[46] Malik, M. R. 1990 Numerical methods for hypersonic boundary layer stability, Journal of Computational Physics 86, 376-413.

CHAPTER 6. General Conclusion

Two popular absorbing boundary conditions, the absorbing sponge zone and perfectly matched layer, are implemented with the spectral difference method on hexahedral meshes for non-linear Euler and Navier-Stokes equations. Both the ASZ and PML perform very effectively in the vortex and acoustic propagation problems. The reflected errors with the two zonal techniques are much smaller than those with the CBC based on linearized one-dimensional Euler equations. The absorbing processes with the two techniques are different owing to the different design concepts. The formula of the ASZ is much simpler than the PML technique and therefore easier to implement. However, it is still somewhat reflective and generates visible reflections at the interface with the ASZ between the physical domain and the absorbing domain. PML is more efficient in absorbing the disturbances.

In the numerical simulations of separated and transitional flow over a SD7003 airfoil at low-Reynolds numbers and moderate incidences, a low-frequency oscillation in the attached boundary layer is observed. The low-frequency instability is found to be apparently two dimensional and convective unstable. The primary growth of the disturbances before the turbulent breakdown over the suction side of the airfoil consists of two stages. The first stage is dominated by the low-frequency instability and the second growth stage is caused by the K-H instability.

The breakdown processes associated with the laminar separation bubbles are numerically investigated. It is shown in all three cases that the breakdown process mainly occurs in the Recovery-Separation region and the feedback mechanism due to the flow circulation inside the LSB plays a critical role in passing the three dimensional disturbances from downstream to the upstream which causes the breakdown of the next shedding vortex. The secondary mechanism in the breakdown process appears differently at different AoAs. With the increase of AoA in current cases, the sequence of states is analogous to the sequence of breakdown states observed in bluff-body wakes with the increase of the Reynolds number, which follows the scenario: elliptic instability → hyperbolic instability → contact instability.

By introducing the roughness bumps near the leading edge, the LSBs are reduced or avoided depending on the bump geometric parameters. It is found that larger and taller bumps generate larger disturbances, which trigger the vortex breakdown, and delay or avoid flow separation. In addition, the flow also transitions into turbulent flow sooner. Although the friction drag increases slightly, the pressure drag is significantly reduced resulting in an overall drag reduction. The reduction of LSBs by roughness bumps also slightly reduces the lift. However, the lift-to-drag ratio is increased in the cases with carefully chosen surface roughness bumps.

ACKNOWLEDGEMENTS

It is a pleasure to thank the many people who made this thesis possible. First and foremost, Dr. Z.J. Wang his guidance and support throughout this research. I would also like to thank my committee members for their efforts and suggestions to this work. Thanks are also given to my fellow group members for their support and insight provided throughout the years. Special thanks to my families for their support all these years.